MONASH University

Graft-Host Interactions in Full-Thickness Wounds Using Mouse Models

Dr. Nicole Ann Garcia

Doctor of Medicine, Bachelor of Science, Graduate Diploma of Surgical Anatomy

Student ID 21468826

A thesis submitted for the degree of Master of Surgery at
Monash University in 2020

With amendments submitted in 2021

Department of Surgery and the Victorian Adult Burns Service, The Alfred Hospital, Melbourne

Copyright notice

Abstract

Background and aims: Little is known about the biomolecular changes of the wound bed and the mechanism by which skin grafting accelerates wound healing. Our aims were to identify biomolecules related to successful graft take following establishment of a full-thickness wound mouse model. **Methods:** An autologous full-thickness skin graft (FTSG) or Biodegradable Temporising Matrix (BTM) was grafted on a full-thickness wound bed on SKH-1 hairless mice. RNA and protein were extracted from the wound bed following a cull at inflammation, proliferation and remodelling stages of healing wounds and analysed for inflammatory (TNF-α, IL-1β, IL-6, CXCL-1), anti-inflammatory (IL-10), proliferation (TGF-β1, VEGF) and remodelling markers (MMP-2, collagen I and III) using Q-PCR and antibody arrays respectively. Results from the full-thickness wounds were compared to FTSG and BTM wounds. **Results:** The majority of the inflammatory markers peaked during inflammation in the full-thickness wound mouse model. Collagen deposition was significantly higher at Day 11, 14 and 21 compared to D1, 2, 5 and 8. Mice with grafts were considered successfully brought to endpoint with taken grafts. Haematoxylin and eosin staining demonstrated the appearance of less inflammatory cells in grafted wounds compared to ungrafted wounds. Wound contraction was significantly greater in wounds grafted with BTM than with FTSG. Collagen deposition was significantly greater in wounds grafted with FTSG than with BTM. RNA expression of key inflammatory mediators was less in grafted wound beds compared to ungrafted wounds. Expression of IL-6, CXCL-1 and MMP-2 were significantly higher in wounds with FTSG compared to BTM at D5. VEGF-A, IL-10 and TGF-β1 were similar with both graft groups. **Conclusion:** There are clear differences in the biomolecular activity in an ungrafted full-thickness, and grafted wounds. Grafting modulates the inflammatory response of spontaneous wound healing. The modulation of the normal wound healing trajectory is yet to be determined. Identification of wound bed biomarkers that can predict healing is essential for design of novel treatment options and/or the development of a more efficacious synthetic or bioengineered dermal substitutes.

Declaration

This thesis is an original work of my research and contains no material which has been accepted for the award of any other degree or diploma at any university or equivalent institution and that, to the best of my knowledge and belief, this thesis contains no material previously published or written by another person, except where due reference is made in the text of the thesis.

Print Name: NICOLE A. GARCIA

Date: 14th December 2020

Acknowledgements

Thank you to the staff of the Skin Bioengineering Laboratory for their never-ending support – to Dr. Shiva Akbarzadeh, who believed in my potential despite my inexperience; to Dr. Mostafiz Rahman for the conversations about life; and to Dr. Ilia Banakh for his sound expertise and parsley.

Thank you to Ms. Heather Cleland and Mr. Cheng Hean Lo.

Thank you to the staff of the Precinct Animal Centre and Monash Histology Platform, Clayton.

Finally, to my family – thank you for everything.

This thesis is dedicated to PGG, Walter, and Olive.

Project Contributions

Project conception and methodology: Dr. Shiva Akbarzadeh (SA) and Ms. Heather Cleland (HC) 100%.

Lysis buffer optimisation experiments: Mostafiz Rahman (MR) (100%). IL-6 ELISA: MR (50%) and Nicole Garcia (NG) (50%). All other laboratory experiments performed by NG (100%).

Masson's Trichrome Staining performed by Monash Histology Platform Services, Clayton, Victoria.

Preamble

The final results of this Master of Surgery are a collation of animal studies and experiments that were significantly affected by the unprecedented events of 2020 and the ongoing CoVid-19 pandemic.

Although great care was taken to ensure that laboratory work continued when possible, the Skin Bioengineering Laboratory was closed for approximately a month and a half in early- to mid-2020 due to the lack of physical space within the premises that meant social distancing could not be adhered to, as well as the first wave of the pandemic that occurred during the first half of the year. Furthermore, animal lines including the SKH-1 mouse line utilised in this body of work were minimised within the Precinct Animal Centre, thus affecting the availability of mice for animal experiments.

In addition, Animal Ethics modifications submitted at the beginning of 2020 were effectively not approved until mid-year due to the requests of the Animal Ethics Committee, which could not be fulfilled until the second half of the year as these required animal experiments.

Table of Contents

Table of Figures

Chapter 1:

Page

Chapter 2:

Chapter 3:

Chapter 4:

Chapter 5:

List of abbreviations

(b)FGF	(Basic) Fibroblast Growth Factor
(m)-RNA	(Messenger)-Ribonucleic Acid
(Q/RT)-PCR	(Quantitative/Real-time)-Polymerase Chain Reaction
AEC	Animal Ethics Committee
BMZ	Basement Membrane Zone
BPAG	Bullous-pemphigoid Antigens
BTM	Biodegradable Temporizing Matrix
cDNA	Complementary Deoxyribonucleic Acid
DEJ	Dermal-epidermal Junction
ECM	Extracellular matrix
EGF	Epidermal Growth Factor
EGTA	Ethylene glycol-bis(β-aminoethyl ether)-N,N,N',N'-tetraacetic acid
ELISA	Enzyme-linked immunosorbent Assay
EMT	Epithelial-Mesenchymal Transition
FAP	Fibroblast Activator Protein
FTSG	Full-thickness Skin Graft
GAG	Glycos-aminoglycans
G-CSF	Granulocyte Colony Stimulating Factor
HEPES	4-(2-hydroxyethyl)-1-piperazineethanesulfonic acid
HIF-1	Hypoxia Inducible Factor-1
IGF-	Insulin-like Growth Factor
IL-	Interleukin
KC	Keratinocyte derived chemokine
KGF	Keratinocyte Growth Factor
KO	Knockout
LWE	Left wound edge
MCP-1	Monocyte Chemoattractant Protein-1

MIP-1β	Macrophage Inflammatory Protein-1beta
MMP-	Matrix Metallopeptidase
NaCl	Sodium chloride
NaOv	Sodium orthovanadate
OCT	Optimum Cutting Temperature Cmpound
PAC	Precinct Animal Centre
PBS	Phosphate-buffered Saline
PDGF	Platelet Derived Growth Factor
PFA	Paraformaldehyde
RAGE	Receptor for Advanced Glycation Endproducts
RIPA	Radioimmunoprecipitation Assay
SA	Surface area
SDF-	Stromal cell-derived factor
SDS	Sodium dodecyl sulphate
TBSA	Total Body Surface Area
TGF-α/β	Transforming Growth Factor-alpha/beta
TIMP	Tissue Inhibitors of Metallo-Proteinase
TNF-α	Tumour Necrosis Factor-alpha
VEGF	Vascular Endothelial Growth Factor
WB	Wound bed
α-SMA	alpha-Smooth Muscle Actin

CHAPTER 1: INTRODUCTION

The Biomolecular Profile of Wound Healing and the Healing Dynamics of Skin Grafts

1. Introduction

1.1. Background

A graft is a section of tissue without its own blood supply, which is transplanted from one area (the donor site) to another – the recipient site[1]. Various tissues can be grafted such as bone, tendon, fat and skin. Of interest to this review are skin grafts, and how these types of grafts survive and modulate the wound bed environment to produce healing.

The predecessor of the skin graft was thought to have come from India circa 600 BCE[2], and was a flap of skin upon a vascular pedicle, fashioned to reconstruct a nose. Although this was a flap and not a graft, it is thought to have initiated the idea that skin could be moved from one area to another. Celsus and Galen attempted skin grafts to repair facial defects in the first two centuries of the common era, and Tagliacozzi attempted grafts taken from the inner arm to repair a mutilated nose in the 1500s. Interest in the field of skin grafting in humans grew in the 1800s, and in 1875, John Reissberg Wolfe compared the pedicle flap to the skin graft, stating that the 'pedicle was not essential … to the vitality of the flap.'[2]

In the mid-to-late 19th Century, the skin graft underwent a series of developments by pioneers such as Jacques-Louis Reverdin, Louis Léopold Ollier and Karl Thiersch (the pioneers of the split-thickness skin graft), and John Reissberg Wolfe and Fedor Krause (to whom the description of full-thickness skin graft is traditionally ascribed)[3]. Skin grafts as a treatment for burns was first published in 1940s[4, 5]. Prior to this wounds could only be left to heal by secondary intention[6].

Despite its long history and widespread use in reconstructive and burns surgery, little is known about how skin grafts repair wounds, and the minimum requirements for graft "take" (healing). Different types of wounds such as chronic non-healing wounds and burns wounds can pose different issues to the process of skin grafting. These include donor availability and wound bed issues. Although the process of graft take has been described in the literature and investigated with animal models[7-9], associated molecular processes for a successful graft have yet to be scrutinised. This is of importance, as improved understanding of how a graft modulates the wound bed to produce healing will help to establish the requirements for successful graft take.

Identification of wound bed biomarkers and changes associated with successful grafting is a prerequisite for the productions of proteins as treatment options to improve graft take and for the development of a more efficacious synthetics or bioengineered culture grafts.

Here I will describe the stages of wound healing in mouse and human models, and explore how autologous and synthetic skin grafting modulates the wound healing and repair process.

1.2. Introduction to the skin

1.2.1. The structure and function of skin

The human skin is the largest organ in the human body, and comprises approximately 16% of the total body weight of an adult[10], weighing 3-5kg on average[11]. Human skin consists of three layers: the epidermis, the dermis, and the underlying subcutaneous fat (also known as the subcutis or hypodermis)[12, 13]. Although anatomically thought of as independent layers, clinically they are interdependent, dynamic functional units that regulate normal structure and function of the organ at molecular, cellular, and tissue levels.[12] They perform vital functions which include: mechanical protection, thermoregulation, immunological surveillance, and the provision of sensation[10, 12] .

Mouse models are widely used as a model for wound healing studies. Its skin structure is similar to humans in terms of its layers except for the excess of hair follicles, the lack of epidermal ridges, and the presence of the panniculus carnosus below the dermis in murine skin.

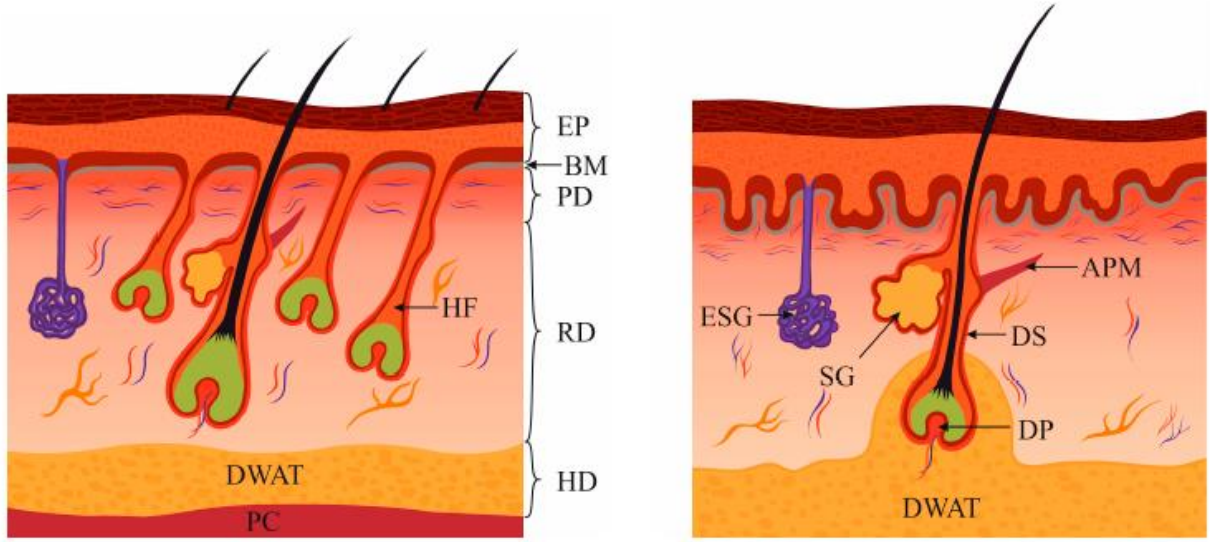

(A) **(B)**

Figure 1.1: (A) Murine and (B) Human skin structure. Rippa et. al. 2019[14]. APM – arrector pilli muscle; BM – basement membrane; DP – dermal papillae; DS – dermal sheath; DWAT – dermal white adipose tissue; EP – epidermis; ESG – eccrine sweat glands; HD – hypodermis; HF – hair follicle; PC – panniculus carnosus; PD – papillary dermis; RD – reticular dermis; SG – sebaceous gland.

The Epidermis

The epidermis is the upper layer of the skin. It is derived from the embryonic ectoderm[15]. The thickness differs greatly according to the regions of the body. It is the thinnest on the scrotum and on the eyelids (thickness ~<0.1mm)[16] and thickest on the back and on peripheral body sites (~ 1.0mm thick)[16]. It is an avascular structure, receiving its nutrients from the papillary dermis directly below its basal layer[13]. The principle cell of the epidermis is the keratinocyte[13]. The stratification of the epidermis is organised into five layers, from deepest to most superficial: the stratum basale, stratum spinosum, stratum granulosum, stratum lucidum, and the stratum corneum[11] (see Figure 1.2). The epidermis, particularly the stratum corneum, constitutes a large part of the physical barrier provided by the skin[12]. This barrier function formed by the stratum is bidirectional as a physical barrier, as it prevents loss of fluid, electrolytes, and proteins; but also shields from noxious chemicals, infections, and ultraviolet radiation[17].

Interfollicular epidermis (IFE) stem cells that reside in the stratum basale maintain epidermal renewal. They undergo a series of programmed biochemical and morphological changes, flattening and hardening as they move upwards to terminate as the stratum corneum[12, 18].

In mice and guinea pigs, studies involving radioactively labelled basal cells demonstrated that the basal to surface transit time of cells ranged from 8-9.5 days in mice to 13.5 days in guinea pigs[19]. To maintain homeostasis, cells lost during turnover must be replaced. Two distinct models have been proposed as to how this homeostasis occurs. The first is based on

a series of experiments performed by Leblond in the 1960s[20] on rat oesophagus (comprised of stratified squamous epithelium that behaves similarly to the epidermis), where he proposed that all basal cells were the same, and that they differentiate and proliferate stochastically. This stochastic model has been also been investigated in *in vivo* mouse models, demonstrating that the epidermal homeostasis is maintained by a population of single, equipotent, committed progenitor cells that differentiate and proliferate stochastically[21].

An alternative explanation was introduced by Potten in the 1980s[19, 22], where he proposed that tissues such as the epidermis are maintained by long-lived, slow-cycling, self-renewing stem cells. These cells generate a population of short-lived 'transit-amplifying' cells that undergo terminal differentiation after a set number of cell-divisions. This is demonstrated in Figure 1.3.

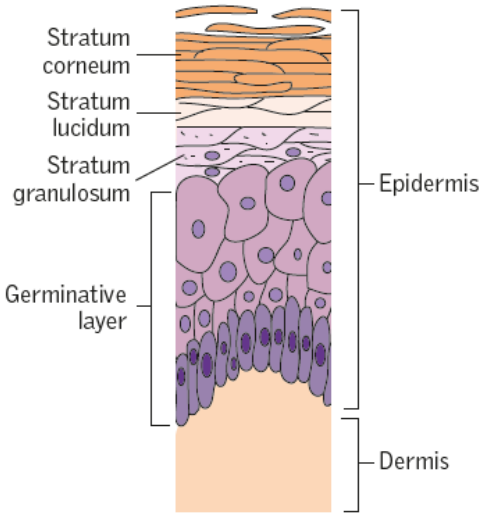

(A)

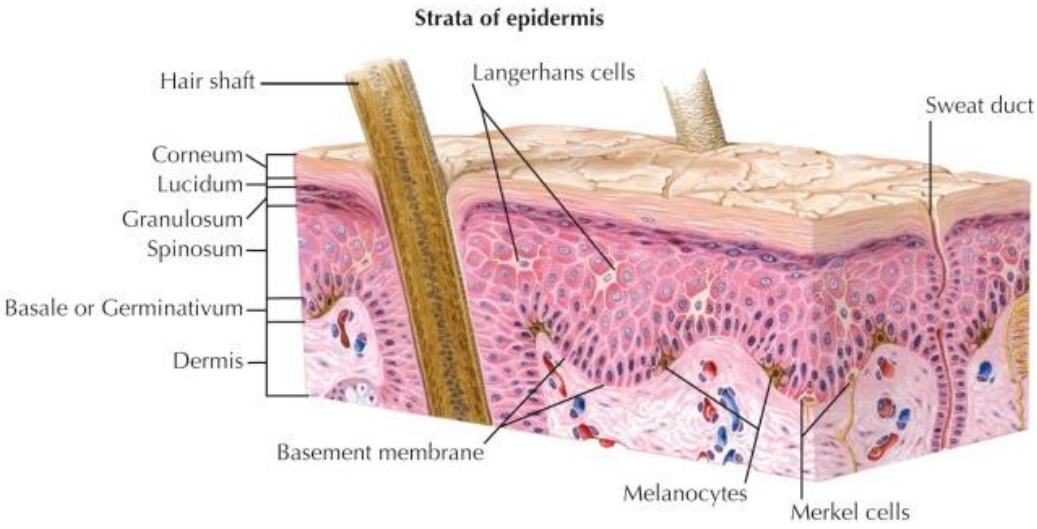

(B)

Figure 1.2: (a) Layers of epithelium of the epidermis. Modified from McLafferty et. al. 2012[11]; **(b) Cutaneous basement membrane or Dermal-Epidermal Junction, as seen at the junction between the stratum basale of the epidermis and the dermis.** Modified from Anderson et. al. 2011[13].

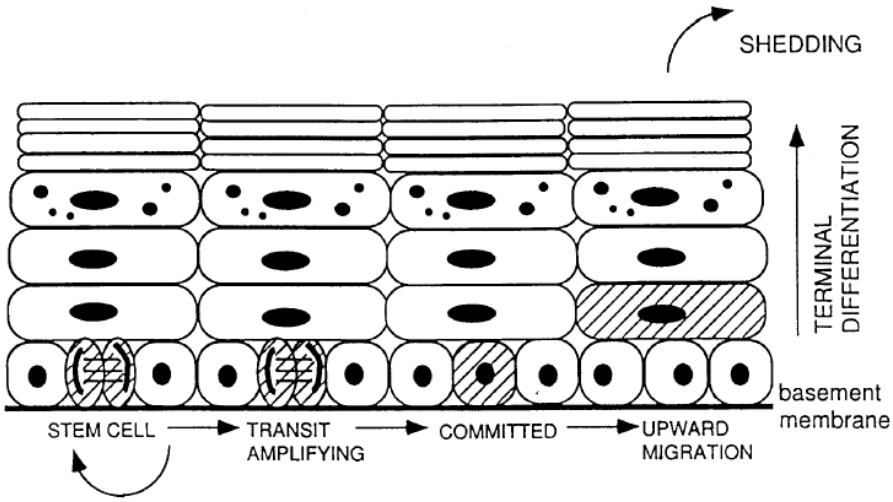

Figure 1.3: Diagram illustrating the organisation of keratinocytes within human IFE. Watt, F. 1998[23]. The daughters of transit-amplifying cells exit the cell cycle and terminally differentiate as they move upwards to the stratum corneum.

The kinetics of IFE stem cell renewal were further investigated with lineage tracing and analysing the clonal fate. Mascré *et. al.* (2012)[24] utilised K14-Cre-ER mice, whose fluorescence targeted mostly cells in the basal layer of IFE, and Inv-Cre-ER mice, which target mainly suprabasal IFE cells. Their findings suggest that IFE maintenance is undertaken by two populations of stem cells: slow-cycling stem cells (whose fluorescent label was attached to the Keratin-14 protein in mice) and more rapidly cycling committed progenitor cells (linked to the involucrin protein). In normal epithelia, keratin-14 is an intermediate filament protein mainly expressed in the basal layer, and involucrin is synthesised after keratinocytes have left the basal layer[25]; both are useful markers for the terminal differentiation of keratinocytes in the epidermis. This study also supports the idea that the committed progenitor cells are responsible for epidermal homeostasis; whereas during wound healing, the slow cycling stem cells contribute most.

Also residing within the stratum basale are melanocytes and Merkel cells. Melanocytes are dendritic cells derived from the neural crest[26]. which migrate to their location early in embryonic development[12]. They produce the pigment melanin, which is packaged into subcellular organelles called melanosomes, and transported to neighbouring keratinocytes in the basal layer. These melanosomes form a 'melanin cap'[26] which performs a critical role in absorbing ultraviolet radiation and minimising damage to the skin[12].

Merkel cells, part of the sensory nervous system, are mechanoreceptors.[16] They transmit sensory information from the skin to sensory nerves[26]. These mechanoreceptors are located in peripheral areas that require high tactile sensitivity, such as the skin of digits, lips, regions of the oral cavity, hair follicles[12]. They sit on the basement membrane, and have desmosomal contacts with keratinocytes[16].

Langerhan's cells are another resident cell of the epidermis. Although not unique to the epidermis, they constitute 3-4% of all epidermal cells, and reside in the mid-epidermis[16]. They are bone marrow derived, and are involved in the skin's immune defence[13]. They are dendritic antigen-presenting and antigen-processing cells. Once the epidermis has been injured, Langerhan's cells undergo changes to allow them to leave the epidermis, and enter the dermal lymphatics which drain into lymph node basins[10]. They are functionally impaired by ultraviolet (UV) radiation, particularly UV-B[12].

The Dermal-Epidermal Junction

In general, basement membrane zones are located at the interfaces between layers of cells[27]. The cutaneous basement membrane zone (BMZ) separates the epidermis and dermis, and is known as the dermal-epidermal junction (DEJ)[28]. Both keratinocytes and fibroblasts contribute protein components to the DEJ during development.

Ultrastructurally, the DEJ can be divided into four major subregions under light microscopy: (i) the basal cell plasma membranes of basal keratinocytes and the hemidesmosomal plaques, (ii) lamina lucida), (iii) lamina densa and (iv) the sublamina densa[29]. The basal keratinocytes are attached to the DEJ via specialised multi-protein complexes called hemidesmosomes. Hemidesmosomes contain plectin, collagen XVII, integrin α6β4, and the bullous pemphigoid antigens (BPAG)1 and BPAG2.

As a unit, this region has functions integral for skin homeostasis. The zone links the keratin filaments of the basal keratinocytes and the collagen components of the superficial dermis[26]. It is also a regulator of epithelial-mesenchymal interactions, acts as a permeability barrier, participates in signal transduction[28] and provides structural integrity for resistance against external shearing forces[12]. The absence or aberrant expression of hemidesmosomal proteins, as seen in inherited cutaneous disorders such as epidermolysis bullosa, have demonstrated skin fragility and blister formation in humans[30]. The DEJ also allows transmission of cells under

homeostatic (e.g. melanocytes and Langerhan's cells) or pathological conditions (e.g. lymphocytes and tumour cells)[27] between the cutaneous layers, which may be important in the context of wound repair, the healing of skin grafts, and the recapitulation of skin with respect to laboratory-based skin equivalents.

The Dermis

The bulk of the skin and its structural integrity as a whole is largely attributable to the dermis[12]. Along with the subcutaneous layer, it is derived from the embryonic mesoderm[13]. It supports and provides nutrients to the epidermis. The thickness of the dermis varies by sex and body region – it is thicker on palms and soles compared to the eyelids, and is thicker in men than women[17].

Fibroblasts are the most abundant cells within the dermis, and are able to synthesize and remodel the extracellular matrix (ECM)[12]. The dermis is composed mostly of collagen produced by the fibroblasts[13]. In addition to ECM, it contains lymph vessels, nerve endings, hair follicles, and glands.[11] It comprises two structurally different layers: the more superficial papillary dermis and the thicker reticular dermis[31]. The papillary dermis contains nerve endings[26], collagen (mostly Type III) and loose elastic fibres. The reticular layer is mostly dense connective tissue with collagen, mostly Type I[17]. It contains two vascular plexuses. The superficial vascular plexus separates the papillary from the reticular dermis, and is responsible for thermoregulation[13]. The deep vascular plexus is present at the junction of the reticular dermis and the underlying subcutaneous fat[16].

The dermis is thus critical during the proliferative phase of wound healing, when the production of ECM is important. The proteins of the ECM act as a scaffold for inflammatory cell migration, along with granulation tissue generation. It provides a temporary substrate which the re-epithelialisation takes place via the epidermal keratinocytes[32]. Fibroblasts promote interactions between the epidermis and dermis through paracrine, autocrine and other forms of communication[33]. and their proliferative and the synthetic activity increases during wound healing[12]. Other cells residing in the dermis include macrophages and mast cells[12]. Fibroblasts have the ability to differentiate into myofibroblasts, which are responsible for wound contraction[32].

Fibroblasts are not homogenous[34, 35]. The two types, papillary and reticular, originate from differing cell lineages and have varying functions in wound repair and skin homeostasis. This has been investigated by using transplantation assays, lineage tracing, and flow cytometry in mouse models[34]. The papillary dermis and the dermal papillae (at the base of the hair follicles) fibroblasts are from a similar lineage. These regulate the growth of hair follicles and the arrector pilli muscles. The reticular fibroblasts, myofibroblasts and hypodermal cells arise from a similar cell line, and are incapable of inducing hair follicles. These are largely responsible for the synthesis of ECM in the primary wave of dermal regeneration during wound healing.

A recent work by Korosec *et. al.* (2019)[36] associated Fibroblast Activation Protein (FAP) and CD90 expression as markers of papillary and reticular fibroblasts respectively. Cell surface markers in human fibroblasts were identified in *in vitro* models using flow cytometry. Papillary fibroblasts (FAP+/CD90-) exhibited greater proliferative potential and could not be differentiated into adipocytes. In contrast, FAP-/CD90+ cells expressed high levels of CD36 (associated with cells of the lower dermis), and easily undergo adipogenic differentiation; this is pathognomonic of reticular fibroblasts (the relationship of adipocytes of the hypodermis with the fibroblasts is discussed later sections).

Fibroblast heterogeneity has also been investigated in adult humans by Tabib *et. al.* (2018)[37]. Two major and distinct fibroblast sub-populations were defined based on SFPR2 and FMO1 markers. SFPR2 expression defined a distinct subpopulation of fibroblasts that are small, elongated, and distributed in high frequencies amongst collagen bundles compared to the cells with FMO1+ lineage. These cells were seen throughout both layers of the dermis. SFPR2+ cells also expressed higher levels of common matrix genes such as Type I collagen and fibronectin, implying their role in ECM production. In contrast, FMO1+ cells were larger with larger nuclei. Their function was less relevant to matrix production, demonstrating lower expression of the collagen-related genes COL1A1 and COL1A2. It confirmed that these two distinct populations were present throughout the dermis and not specifically aligned with the papillary or reticular layer of the dermis. This suggests that although papillary and reticular subpopulations are established during development, there is fluidity in fibroblast subpopulation maintenance in adults.

The FMO1+ cells identified in Tabib's work would fit best with the characteristics of papillary fibroblasts (and SFPR2+ cells with reticular) if we were to consider the behaviour as outlined by Driskell and colleagues. However, studies using single-cell RNA sequencing techniques show that although the function of fibroblasts is separated by layers, much like the epidermis is with keratinocytes, the organisation of these cells is more complicated than initially thought. Both populations of SFPR2+ and FMO1+ cells were divided further into subpopulations, further adding to the idea that 'fibroblasts' may be a simplistic, collective term for a diverse group of cells involved in wound healing. However, it is important to note the divergence in human and murine models.

Nevertheless, the differences between papillary and reticular fibroblasts are numerous, both structurally and functionally, and are summarised in the review by Rippa and colleagues (2019)[14]. A modified table is below.

Characteristics	Papillary Fibroblasts	Reticular Fibroblasts
Morphology	Spindle-shaped	Stellate-shaped
ECM	Weaker alignment of collagen fibres, higher proteoglycans content.	Ordered network of collagen fibres and elastin strands.
Positivity for α-Smooth Muscle Antibody (SMA)	Small part of fibroblast is α-SMA positive.	Most part of fibroblast is α-SMA positive.
Contribution to skin equivalents	Support the formation of a multilayered, more stratified and differentiated epidermis with ridges. ECM components promote the growth of keratinocytes.	Do not support the formation of a fully-stratified epidermis. Altered basement membrane composition.
Scarring	May improve scar condition.	Generates a matrix typical for fibrosis.

Table 1: Characteristics of papillary versus reticular fibroblasts. Rippa *et. al.* 2019[14].

Hair Follicles

As epidermal renewal is thought to be controlled by stem cells located in the stratum basale or a portion of the hair follicles called the bulge[38] to induce hair follicles could lead to epidermisation, and thus the potential closure of a wound. The hair follicle has been identified as a reservoir of cells with a wide range of therapeutic possibilities not limited to the development of hair[39].

Regeneration of the epidermis after wounding involves the activation, migration and proliferation of keratinocytes from stem cell niches of the surrounding unwounded epidermis and other appendages such as hair follicles. The presence of active hair follicles has been shown to accelerate wound healing in murine *in vivo* models[40]. Hair follicles consist of both follicular (epithelial) stem cells and mesenchymal stem cells. The follicular stem cells reside in the bulge area of the follicle (located below the sebaceous gland), and the dermal papilla at the base of the follicle lower down[14]. Structurally, murine hair follicles are similar to human follicles and they contain the same principal cell types. Although they also undergo repetitive cycling, significant interspecies differences do exist, thus limiting the translational capacity to humans from murine models[41].

In contrast to epidermal basal cells, which are unipotent and differentiate to form the mature epidermis in adult skin[42], hair follicle stem cells from the bulge region have been shown to have regenerative capacity of hair follicles as well as epidermal regeneration following wounding[43]. Defects in the hair follicle bulge in wounded transgenic mice established an acute delay of wound re-epithelialisation[43]. Lineage analysis in transgenic mouse wounds have found that stem cells in the hair follicle bulge contribute to wound repair but not to homeostasis of the epidermis[44].

The dermal papilla also contains mesenchymal stem cells[45]. *In vitro* studies of murine fibroblasts and dermal papilla cells demonstrate they reorganise the ECM in a similar fashion in culture, as well as forming the cytoskeletal protein vimentin in similar timelines[46]. Hair follicle cells were even found to be superior to fibroblasts in influencing DEJ formation in murine *in vitro* and *in vivo* models[47], demonstrating their multi-functional role in wound healing.

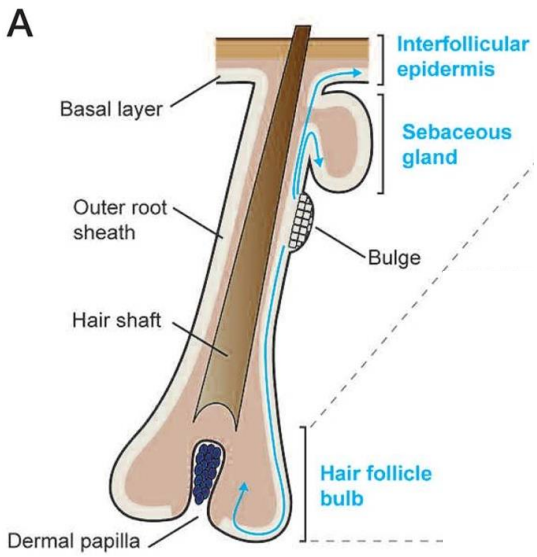

Figure 1.4: Schematic representation of the human hair follicle. Modified from Fuchs, E and Nowak, J. A. 2009[48].

The Hypodermis

The hypodermis, or the subcutis, lies beneath the reticular dermis. It is made up of looser connective tissue[17]. This layer of subcutaneous fat insulates the body, serves as a reserve energy supply, cushions and protects the overlying skin, and allows for its mobility over the underlying structures[12, 17].

The dermis and the hypodermis are structurally and functionally integrated through networks of nerves and vessels, as well as in the continuity of epidermal appendages[12]. Both the dermis and the hypodermis are derived from the embryonic mesoderm[13].

The hypodermis is composed mainly of adipocytes, organised into lobules[17]. They have roles in the storage of triglycerides as an energy source. They also function as endocrine cells that secrete growth factors (for example, fibroblast growth factor and its receptor are expressed in both white and brown human adipose tissue[49]) and cytokines associated with physiological processes such as glucose and lipid metabolism[50].

The ability of adipose tissue and adipose-derived cells to influence wound healing has been demonstrated *in vivo*. When seeded onto a polymer scaffold, cultured for 14 days, and grafted onto athymic mice, fibroblasts derived from human adipose significantly stimulated angiogenesis and re-epithelialisation when compared with fibroblasts derived from the papillary dermis[51]. Complete wound re-epithelialisation was only observed in mice treated with adipose cultured constructs in the same study.

In a full-thickness burn wound mouse model, where there is by nature a lack of dermis, fat grafting of the wound bed has positively influenced angiogenesis[52]. Mice treated with fat grafts also demonstrated a decrease in wound fibrosis, as measured by immunostaining and biochemical markers. This highlights the ability of adipocytes, even in transplanted form, to affect change in the wound bed milieu.

Dermal defects that occur in the absence of adipocytes demonstrated a loss of wound closure integrity and a resulting recurrence of the wound, as investigated in lipoatrophic "fatless" mice[53]. The same study also demonstrated that not only do alterations in adipocyte formation hinder the production of fibroblasts, they may also promote fibroblast production from an unknown fibroblast precursor cell to mediate fibroblast recruitment during skin wound healing.

1.3. Wound Repair

Wound repair has been extensively investigated[54, 55]. It is a process that seems aimed solely at wound closure and survival rather than functional and aesthetic outcomes. Our increased understanding has led to the advancement of the way we treat injuries such as burns and chronic wounds. Nevertheless, wound healing is still appreciated as a complex process that may be derailed by a host of factors. Better understanding of the processes involved may assist in the development of new methods of wound management and treatments to improve outcomes.

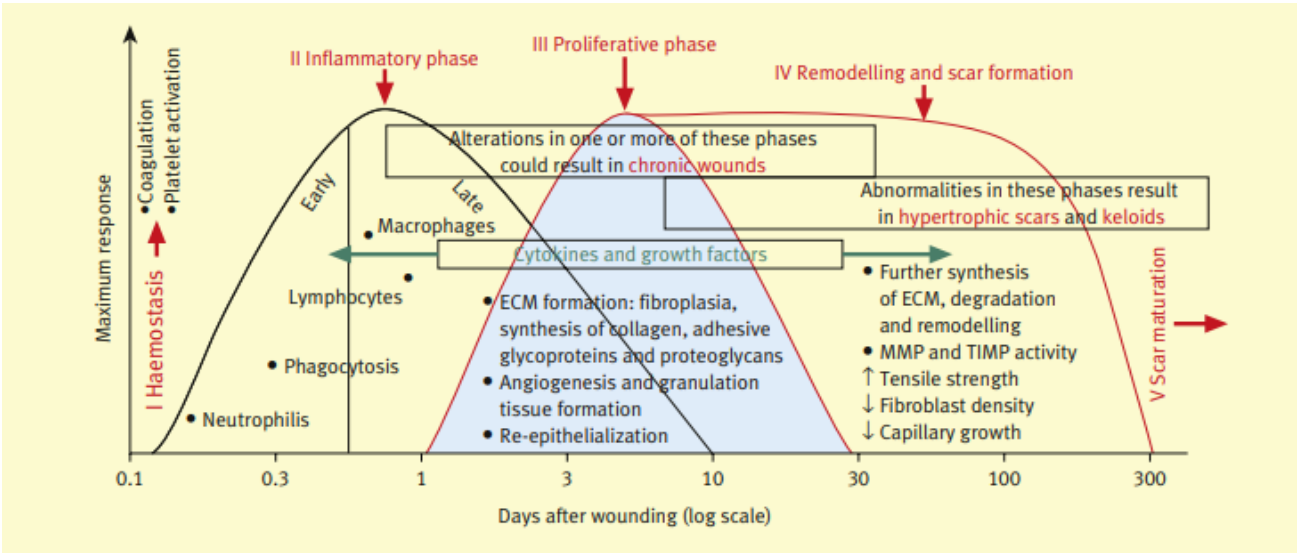

Figure 1.5: Phases of wound healing in humans. Enoch, S. & Leaper, D. J. 2008[56].

1.3.1. The Classic Model of Spontaneous Wound Repair

Haemostasis and Inflammation

Although thought of discrete phases, the stages of wound healing overlap in cellular and molecular levels. The first stage of acute wound healing is dedicated to haemostasis and the formation of a provisional wound matrix by way of a clot. This phase is immediate upon injury, and also initiates the inflammatory process. When a cutaneous wound occurs, blood and lymphatic vessels are traumatized, and blood thus enters the wound, flushing it to remove antigens and micro-organisms[57]. The clotting cascades are initiated, vasoconstriction triggered by the platelets, and the blood clots. This provides a provisional matrix that acts as a scaffold for the migration of the cells of wound healing[58].

Both platelets and leukocytes release cytokines and growth factors to activate the inflammatory process (IL-1α, IL-1β, IL-6 and TNF-α), stimulate collagen synthesis (FGF-2, IGF-1, TGF-β), activate the transformation of fibroblasts to myofibroblasts (TGF-β), commence angiogenesis (FGF-2, VEGF-A, HIF-1α, TGF-β) and support the re-epithelialisation process (EGF, FGF-2, IGF-1, TGF-α)[59]. Cytokines and growth factors relevant to this will be discussed in further detail below.

Concurrent with haemostasis, early inflammation occurs from days 0-2 post injury and is marked by neutrophil recruitment. 'Late' inflammation occurs from days 2-3 post injury. This phase is marked by the appearance and transformation of monocytes[56, 59].

In early inflammation, neutrophils are recruited to the site of skin injury by the products released by degranulated platelets and the by-products of bacterial degradation. The neutrophils kill the local bacteria and help to breakdown necrotic tissue[60].

Neutrophils release inflammatory mediators such as IL-1β, TNF-α, and IL-6. In turn, these stimulate other cytokines and growth factors such as VEGF and IL-8 to allow for the next stages of wound healing such as angiogenesis and epithelialisation. Following this, during the late inflammatory phase, neutrophils are replaced by macrophages, and enter the wound to continue the wound healing process by phagocytosing pathogens and cell debris present. They also secrete growth factors, chemokines, and cytokines, some of which are able to activate the next phase of wound healing (the proliferative phase)[55].

Interleukin-6

The interleukin-6 (IL-6) family belongs to a family of cytokines including IL-6 and IL-11[61] and is commonly used as a marker of inflammation. IL-6 is involved in the growth and differentiation of numerous cell types of dermal and epidermal origin[62]. IL-6 is not spontaneously produced by intact normal cells; in wound healing, it is primarily produced by epidermal keratinocytes with smaller amounts being produced by macrophages, Langerhan's cells, and dermal fibroblasts[63]. Increased IL-6 levels have been seen in papulosquamous skin pathologies such as psoriasis, with IL-6 also stimulating the proliferation of human keratinocytes *in vitro*[64]. *In vivo* rat and mouse models have also demonstrated that an overexpression of IL-6 in normal, unwounded rats causes epidermal proliferation and inflammation[65]; while overexpression in transgenic mice causes a thickened stratum corneum[66]. In murine skin lesion models, IL-6 has been observed to consistently peak early in the inflammation phase as a pro-inflammatory cytokine, with a concurrent increase in TNF-α and IL-1β[67, 68]. In a murine excisional wound model, the peak of IL-6 was observed at 18 hours post wounding in comparison to a non-wounded control[69].

Fibroblasts, through the expression of IL-6 and keratinocyte growth factor (KGF)-2, cause the proliferation and migration of keratinocytes[54]. The importance of IL-6 in wound healing is evident from delays wound healing observed in IL-6 deficient mice. IL-6-deficient mice (IL-6 knockout, KO) require up to three-fold longer to heal in comparison to wild-type controls, with decreased inflammation, granulation tissue formation and neovascularisation. This delay was reversed with a single dose of recombinant murine IL-6 or intradermal injection of an expression plasmid containing murine IL-6 cDNA[70]. IL-6 has also been demonstrated to indirectly induce keratinocyte migration only in the presence of fibroblasts in IL-6-KO mouse *in vitro* models. Keratinocytes and fibroblasts were isolated from neonatal IL-6-KO mice and treated with recombinant mouse IL-6 (rmIL-6). rmIL-6 alone did not significantly modulate the activity of cultured IL-6-KO keratinocytes, whereas there was a significant 5-fold increase in the migration of IL-6 KO keratinocytes when co-cultured with fibroblasts following the rmIL-6 treatment[71].

The wound healing delays in steroid-induced immunosuppressed mice was also reversed by administration of recombinant murine IL-6. Conversely, in control mice, administered murine IL-6 delayed the wound healing process. Furthermore, the increase in MMP-10 expression

seen in steroid-treated mice was attenuated with recombinant IL-6 administration, suggesting that IL-6 may also influence dermal matrix formation and collagen synthesis[72]. Its activity on fibroblast differentiation has been investigated further, with data indicating that α-SMA expression (a marker of myofibroblasts, the primary mediators of wound contraction) is dysregulated in IL-6 KO mice[73]. This behaviour of IL-6 – expressed in two distinct phases: upregulated quickly after skin injury peaking 12 hours post-injury, and again at >72 hours[73] – may be an indicator of the pleiotropic nature of this interleukin.

Interleukin-1β

The interleukin-1 (IL-1) family has 11 members including IL-1α and IL-1β. IL-1β is a potent pro-inflammatory cytokine that was originally identified as a pyrogen[61]. Both the α and β subtypes are synthesised by multiple cell types including monocytes, macrophages, and neutrophils; however, it is thought that the expression of IL-1β is induced primarily as a response to microbial molecules[74]. Macrophages secrete paracrine IL-1 and KGF that stimulate fibroblasts in both *in vivo* rat and *in vitro* human studies[75-77]. In *silico* and *in vitro* studies have demonstrated that IL-1β stimulates murine keratinocyte and fibroblast cell lines to produce keratinocyte-derived chemokine (KC, homologous to human IL-8) to recruit more inflammatory cells in an autocrine fashion[78].

IL-1β has been shown to be upregulated in a murine model of excisional wounds, along with a number of other cytokines. Its peak was observed at 24 hours post wounding compared to a non-wounded model[69]. A murine partial-thickness (heated rod) burns model was observed to have a peak of IL-1β protein, at the 3 day mark post injury[79]. Chemically-induced skin lesions (using lewisite, an organoarsenic compound) were examined in hairless, immunocompetent SKH-1 mice, and both IL-1 proteins (α and β) were downregulated[67]. SKH-1 mice and their role in wound healing studies will be discussed later in this review.

Diabetes is associated with impaired wound healing, and there is evidence of elevated levels of IL-1β in the wounds of both diabetic humans and mice[80, 81]. Expression of IL-1β from macrophages isolated from wounds of human diabetic patients was negatively correlated with Peroxisome Proliferator-Activated Receptor (PPAR)-γ in a 2015 study by Mirza *et. al.*[82] In a healing wound, macrophages undergo a transition from pro-inflammatory to healing phenotypes, and this switch is dependent on the activation of PPAR-γ. Thus, IL-1β may negatively regulate PPAR-γ activity in diabetic, non-healing wounds.

The activity of IL-1β has also been implicated in abnormal scarring: oxidative and heat stress proteins (important mediators in abnormal scar formation) are stimulated through IL-1β pathways, and are shown to develop in scars after severe burns. This has been demonstrated in human *in vitro* studies comparing fibroblasts from normal skin and hypertrophic scars[83].

Tumour Necrosis Factor-α

Tumour necrosis factor (TNF)-α is a potent inflammatory mediator of the innate immune system[61]. It is secreted by macrophages and mast cells, and has been shown to exhibit properties cytotoxic to tumour cells. Like IL-1, TNF-α is thought to promote re-epithelialisation through the production of KGF and its effect on fibroblast activation. It is a pro-inflammatory cytokine implicated in sepsis[84] and chronic inflammatory conditions such as rheumatoid arthritis[85].

Its role in the modulation of the inflammatory response has also been observed. A study by Yimin *et. al.* investigated the granulomatous and inflammatory response of mice inoculated with *Rhodococcus aurantiacus*, a Gram-positive bacteria related to the *Mycobacterium* species responsible for tuberculosis[86]. It was found that the TNF-α knockout mice had a high bacterial burden after inoculation, but if pre-treated with exogenous recombinant TNF-α the day prior to infection, there was an increased rate of bacterial elimination post-infection. Administration of anti-murine IL-6 mouse antibodies (to deplete the endogenous IL-6 *in vivo*) the day prior to infection had no effect on bacterial clearance, but improved the overall mortality of TNF-α knockout mice. It thus appears that TNF-α plays an essential role in bacterial clearance.

TNF- α levels peaked at 72 hours post wounding both in a murine excisional wound healing model as confirmed by ELISA assay and Q-PCR[69], and in a murine partial thickness burns model confirmed by PCR.[79] Much like IL-1β levels in chemically-induced skin lesions[67], TNF-α did not demonstrate an increase in response to sulfur-mustard exposure[68]; in fact, there was no observable change in levels in this chemical-wound model. This would suggest that chemically-induced skin lesions may not be an on optimal vehicle to examine the inflammatory consequences of wounds given the difference in profile, and that excisional or thermal wound models would be more effective.

Valvis *et. al.* (2015)[87] demonstrated that at day 1 post the administration of a full-thickness burn to mice, TNF-α was significantly elevated compared to an equivalently sized full-thickness excisional wound. The same study also demonstrated the delayed onset of IL-6 production in the excisional model compared to the burn model, and an earlier neutrophil chemoattractant response with no significant increase in macrophage inducing cytokines. The expression of IL-6 was increased in the burns model compared to the excisional wound model. The cytokine profile of burns injuries, in particular partial-thickness burns injuries, will be discussed later.

Interleukin-8

Compared to the other inflammatory cytokines, interleukin-8 (IL-8) is relatively new following discovery of its properties as a neutrophil-activating peptide in the early 1990s[88, 89]. It is a chemoattractant, pro-inflammatory cytokine produced by a variety of cells including keratinocytes and macrophages[54] and has been demonstrated to play a causative role in inflammation by recruiting and activating neutrophils[90]. It also enhances neutrophil adherence, chemotaxis and granule release as well as enhancing epithelialisation[54], with a role in angiogenesis[91] particularly in tumours. A recent review by Fousek, *et. al.* [92] highlights the multifaceted role of IL-8 in tumour progression and disease prognostication due to its potency in affecting immune cells.

In addition to its effects on inflammatory cells, an *in-vitro* study observed that IL-8 also stimulates endothelial cell proliferation and capillary tube organisation through direct interaction with the endothelial cells[93]. Endothelial cell survival and programmed apoptosis are critical for the maintenance of the vascular structure and cell turnover in angiogenesis; and as such, endothelial cells treated with culture medium containing IL-8 in the same study showed higher levels of active Matrix Metalloproteinase (MMP-2 and MMP-3) production. This indicates that IL-8 plays an important angiogenic role in wounds and tumours; however, the exact mechanism through which this occurs remains unclear. Its roles in murine full-thickness wound repair and behaviour at the grafted wound bed is also yet to be determined.

Proliferation

Proliferation occurs 2-10 days after injury[55], and consists of epithelialisation, angiogenesis, and provisional matrix formation[54].

The first event is the migration of keratinocytes over the wound bed (epithelialisation). They migrate from the edges of the wound until a sheet of cells completely covers the wound. A highly conserved cellular program between metazoan organ systems termed *epithelial-mesenchymal transition* (EMT) allows stagnant epithelial cells to gain motility, much like mesenchymal cells, and travel across the wound[94]. Epithelialisation begins shortly after wounding and is initially stimulated by IL-1 and TNF-α.

Platelets and macrophages from the haemostatic clot continue to stimulate fibroblast proliferation and migration into the wound bed by producing platelet-derived growth factor (PDGF) and transforming growth factor (TGF)-β1. By the third or fourth day, the wound becomes rich in fibroblasts which lay down the extracellular matrix with proteins such as hyaluronan, fibronectins and proteoglycans. Nearby damaged endothelial cells secrete basic fibroblast growth factor (bFGF) to signal endothelial cell migration.

This new stroma of extracellular matrix, or 'granulation tissue', is pink, vascular, and fibrous. Fibroblasts also subsequently produce collagens and fibronectins[95]. Fibroblasts then synthesize and secrete KGF-1, KGF-2 and IL-6 – these stimulate adjacent keratinocytes to migrate to the wound area, proliferate, and differentiate in the epidermis[54].

The concurrent formation of new blood vessels (angiogenesis) is necessary to sustain the newly formed granulation tissue. It relies on extracellular matrix in the wound bed, as well as the stimulation of endothelial cells by vascular endothelial growth factor (VEGF)[58]. VEGF is secreted predominantly by keratinocytes on the wound edge, but also by macrophages, platelets, fibroblasts and other endothelial cells)[54] in response to injury and hypoxia. Keratinocytes can be stimulated to produce VEGF by IL-1, TNF-α, TGF-β1, and KGF.

Fibroblasts, which can come from the wound edge as stated above or from the bone marrow[96], may begin transforming into myofibroblasts under the influence of macrophage-secreted TGF-β1 whilst also synthesizing collagen. The appearance of contractile myofibroblasts corresponds to the commencement of wound contraction.

Transforming Growth Factor-β1

The TGF-β superfamily includes types 1, 2 and 3. It was originally isolated in the 1970s, when attempts to define an individual peptide growth factor that could 'transform' or promote cell growth[97]. There are also three TGF-β receptors (TGFBR1, 2 and 3)[98]. It is the β1

subtype that predominates in cutaneous wound healing. It is primarily synthesised and produced by macrophages, fibroblasts, keratinocytes and platelets[99]. Wounds of transgenic mice lacking a TGF-β receptor, TGF-β receptor II (TGF-βRII), have been shown to have delays in re-epithelialisation compared to wild-type mice 3 days post-wounding. There was also an almost complete absence of dermal regeneration and impaired fibroblast migration and myofibroblast differentiation as shown through immunohistochemical staining. However, the same study also demonstrated that TGF-βRII-null mice contained more proliferating keratinocytes compared with the wild-type control at 7 days, reflecting the complexity of TGF-β functionality[100].

The TGF-α subtype has been shown to directly stimulate keratinocyte migration and proliferation[101]. However, the effect of the β1 subtype on keratinocyte activity remains unclear whether TGF-β1 promotes keratinocyte proliferation directly or by secondary effect via the promotion of ECM production and deposition. *In vitro* studies have shown that TGF-β1 has the capacity to induce keratinocyte motility through its interaction with integrins[102] and its ability to induce epithelial-to-mesenchymal transition in cell culture[103]. An overexpression of TGF-β1 in transgenic mice resulted in aberrant keratin expression, and growth arrest of the epidermis and hair follicles[104]. Phenotypically, the mice were born with taut skin, which ultimately proved lethal due to their inability to move and breathe.

Deletion, rather than overexpression, of the TGF-β1 gene in mice has also demonstrated lethality. In half of embryos born, multi-organ failure followed with death by 3 weeks in those successfully born alive[105]. There was a decrease in granulation tissue formation, vascularity, collagen deposition and epithelialisation in the wounds of these mice, along with a marked increase in the inflammatory infiltrate of the wound bed compared to wild-type mice[106]. Koch *et. al.* in 2000[107] also demonstrated that, although wounds of both TGF-β1-KO mice and wild type mice were both healed by 10 days, the KO mice showed an overall reduction in the amount of granulation tissue and an increased rate of epithelialisation compared to wild-type controls. Together, this suggests a negative effect of TGF-β1 on epithelialisation.

Scar formation is heavily influenced by TGF-β1, as it is a potent stimulator of collagen production by fibroblasts[108]. It also suppresses the expression of matrix metalloproteinases (MMPs), the enzymes that modulate the synthesis and degrade the ECM[109]. As a result, TGF-β1 has been implicated in aberrant scar formation pathologies such as keloids.[110] It has been

shown to accelerate wound healing in partial-thickness murine wounds through its stimulatory effect on fibroblasts and ECM deposition rather than the inhibition of keratinocyte migration. In full-thickness wounds, however, it has demonstrated wound closure delays by the inhibitory effect on keratinocyte migration[111], by prolonging the inflammatory phase of wound healing through its intrinsic pro-inflammatory effect[112] and by leaving the wound open.

Platelet Derived Growth Factor

PDGF is a disulphide-linked dimeric protein composed of varying combinations of four polypeptide chains (A, B, C and D). It acts through tyrosine kinase receptors and the downstream extra-cellular regulated kinase (ERK) cascade[113], and directly increases fibroblast proliferation, along with indirectly increasing fibroblast proliferation through its effects on IL-1, TNF-α, and TGF-β[54]. It was the first growth factor shown to be chemotactic for cells migrating into the wound bed such as neutrophils and fibroblasts, and stimulates fibroblasts to contract collagen matrices along with inducing the myofibroblast phenotype[59].

The BB isoform, known as PDGF-BB, was shown to be the major stimulating factor for human dermal fibroblast motility in an *in vitro* study performed by Li, *et. al.* in 2004[114]. Human dermal fibroblasts were cultured on polylysine control matrix or a type I collagen matrix, with or without PDGF-BB. Kinetic analysis of the cells' behaviour *in vitro* revealed that PDGF-BB does indeed enhance the migration of cells. This enhancement is more evident in the later phase of migration (i.e. more evident 16 hours post seeding compared to 2 hours post). Furthermore, PDGF-BB would not induce fibroblast migration without the collagen matrix, indicating again the PDGF-BB alone cannot initiate cellular migration in the absence of a physiological ECM. Conversely, in the absence of PDGF-BB, collagen was able to initiate cellular migration, until a plateau was reached around the 4 hours post seeding mark. The addition of the PDGF-BB allowed cells to continue to migrate over the plateau reach by the collagen alone. This highlights two important points: that fibroblasts require groundwork by way of an ECM to migrate, and that PDGF-BB demonstrates promotility effects for fibroblasts[114].

The topical application of recombinant PDGF-BB (rPDGF-BB) to an avascular wound model in rabbits to facilitate skin grafting demonstrated an increased amount of granulation tissue at equivocal timepoints, as assessed macroscopically, compared with an avascular wound

treated with control buffer. Although the addition of hyaluronic acid with the rPDGF-BB generated more granulation tissue macroscopically, it was not until a vascular wound bed in the *in vivo* model was added that the most granulation tissue was produced.

All skin grafts subsequently applied to the granulation tissue with vascularised wound beds and those treated with rPDGF-BB survived completely. All skin grafts in the control buffer group, and the rPDGF-BB alone treated groups failed to take, with the exception of those that were grafted with onto a vascular wound bed[115]. This once again serves to highlight that PDGF seems to only work effectively in concert with other factors such as other cytokines and wound bed qualities. Following several clinical trials, it was approved in 1997 by the Food and Drug Administration in the United States of America for the treatment of diabetic foot ulcers[116]. It remains the only growth-factor based adjunct to wound therapy to be so.

The efficacy of PDGF-BB as a topical adjunct to improve full-thickness acute wound healing in non-diabetic humans, has also been demonstrated. Seven healthy volunteers were given either an antibiotic or PDGF-BB gel to treat full-thickness punch biopsy wounds. More PDGF-BB treated wounds were healed in comparison to antibiotic gel treated wounds at all study time points. These differences were statistically significant[117].

Vascular Endothelial Growth Factor-A

The vascular endothelial growth factor (VEGF) family contains multiple members (VEGF-A to VEGF-E).[99] VEGF-A is one of the most important positive regulators of angiogenesis along with fibroblast growth factor (FGF)-2, also known as basic-FGF (bFGF)[59]. They bind to three different transmembrane tyrosine kinase receptors, named VEGF receptors (VEGFR) 1-3 (i.e. VEGFR-1, VEGFR-2, VEGFR-3) localised to the endothelial surface of blood vessels. VEGF-A binds to VEGFR-1 and -2.[118] It is produced by endothelial cells, keratinocytes, fibroblast smooth muscle cells, platelets, neutrophils and macrophages[99, 119].

VEGF-A expression was strongly induced following cutaneous injury in rat and guinea pig models confirmed by in-situ hybridisation, with keratinocytes and macrophages being the major producers[120]. Macrophages stimulate keratinocytes to express VEGF with IL-1 and TNF-α, and fibroblasts stimulate keratinocytes to express VEGF with TGF-β and KGF-2[54]. KGF-knockout mice have shown decreased angiogenesis and VEGF mRNA levels *in vivo*, highlighting a regulatory positive feedback within the growth factor families[121].

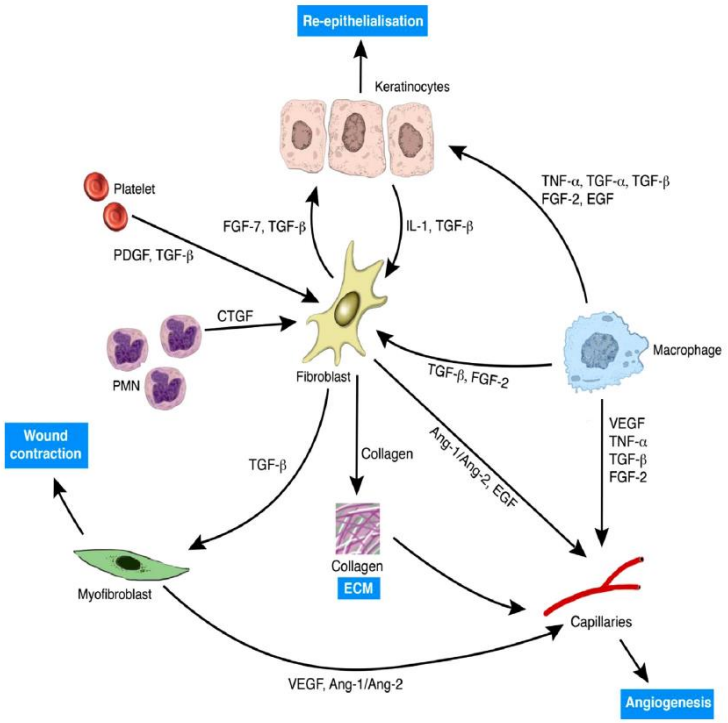

Figure 1.6: Cell-cell and cell-matrix interactions. VEGF pertinent interactions can be seen at the bottom right leading to angiogenesis. Greaves, N. 2013.[122]

Interleukin-10

IL-10 is an anti-inflammatory cytokine, regulating the synthesis of pro-inflammatory cytokines such as IL-1β, IL-6 and TNF-α in activated macrophages[123]. Both IL-10 mRNA and protein levels were detectable in a murine incisional wound model for 10 days after injury, with biphasic peaks at 3 and 72 hours post incision[124]. IL-10 expression also had biphasic peaks in a murine full-thickness burns wound model, however peaking at days 1 and 7 post-burn[125]. These peaks were similar to the temporal profile of TGF-β1 in the same study. Its role in the proliferative phase of wound healing is demonstrated in IL-10 deficient foetal mice, whose wounds heal by scar formation rather than by scarless regeneration as is commonly seen in foetal wounds[126].

Injections of a purified IL-10 in mice given full-thickness wounds produced wounds that had accelerated re-epithelialisation, increased granulation tissue coverage and improved wound revascularisation when compared to mice injected with placebo control. In addition, mice treated with IL-10 induced a reduction of TGF-β1 expression and limited myofibroblast differentiation, further highlighting the suppressive role of IL-10 on fibrosis and scarring.

Remodelling

The final stage of wound repair commences 7-10 days following injury, and lasts for a year or longer. The main feature of this phase is the deposition of collagen into an organised network for wound integrity and strength[54, 55]. If there are matrix deposition problems, then wound strength is compromised. If there is an excess of collagen production, then a hypertrophic scar or a keloid scar may result. During this stage, fibroblasts also differentiate into myofibroblasts under the influence of TGF-β[127] and PDGF to facilitate wound contractility for closure, and cicatrisation of the resultant scar.

Initially, this matrix is composed mainly of fibrin and fibronectin laid down previously in the haemostasis stage of inflammation by macrophages. Following this, fibroblasts synthesise glycosaminoglycans and proteoglycans, providing a haphazard framework for the new matrix. It is this temporary matrix that is replaced by an organised collagen matrix[54]. Types I and III collagens make up about 95% of the collagen of a scar. The collagen in uninjured skin is 80-90% Type I collagen, and 10-20% Type III; granulation tissue has 30% Type III collagen, and a mature scar only has 10%[128]. This continual decrease in Type III collagen as the scar matures is mediated by the matrix remodelling proteinases (MMPs) and is influenced by changing concentrations of TGF-β, PDGF, IL-1, and EGF. The suppression of MMPs is, in turn, suppressed by tissue inhibitors of metalloproteinase (TIMPs), whose production by fibroblasts is upregulated by TGF-β and IL-6.

Collagen: Types I and III

The major component of connective tissue in a developing scar is collagen. It is organised as fibres composed of individual polymerised collagen molecules. These molecules are made up of three polypeptide chains arranged in a characteristic triple helix[128]. Their main function is to provide mechanical stability to animals, with up to 28 collagen types evident in humans and mice[129]. Type I collagen is the main protein in human bone, skin and tendon, type II is specific to cartilage; and type III along with type I are the main structural components of blood vessels[129].

During the remodelling phase of wound healing, Type I collagen replaces the fibronectin and Type III collagen present in the provisional matrix laid down during proliferation, becoming the predominant constituent in the extracellular matrix[128, 130]. This change in protein levels is reflected in the burn wounds of a mouse model. Partial thickness burns were applied to

C57Bl/6 mice and the inflammatory markers in the wounds measured. Fourteen to 21 days post burn, Type III collagen (Col3α1) mRNA levels were higher compared to Type I Collagen (Col1α2) levels. By 70 days post burn, the inverse was found. Both types peaked at day 28 post burn, likely reflecting the transitioning state of the extracellular matrix[79].

Similar to inflammation and proliferation phases, the remodelling phase in a full-thickness burn model in mice demonstrated significant differences between the excisional wound and burn wound repair models. The expression of collagen type I peaked much earlier, between days 3 to 14 post-burn compared to a simple excisional wound model further reflecting fundamental differences in repair process of two different types of wounds[125, 131]. In the mature burn scars of humans, histological specimens demonstrated an increase in the type I collagen density and thickness and a decrease in the amount of type III collagen, compared to normal skin controls, with a lack of the "basket-weave" pattern of normal skin[132].

Collagen has been demonstrated to be a requirement for cellular motility of human dermal fibroblasts *in vivo,* independent of any topical growth factor agents such as PDGF-BB[114]. The interplay between other extracellular matrix proteins and collagens has also been demonstrated in excisional wounded rat models. The topical application of a low-molecular weight hyaluronic acid (the principal glycosaminoglycans found in extracellular matrix) accelerated excisional wound healing by modulating inflammatory cytokines (such as IL-1β, IL-6 and TNF-α), promoting epithelialisation and neovascularisation, and remodelling collagen from a Type III to a more mature Type I[133].

There also seems to be a difference in expression of Type I collagen between fibroblasts in non-ulcerated skin of patients with diabetes and skin from diabetic foot ulcers. Immunofluorescent staining suggested that Type I collagen was intracellularly localised in fibroblasts from diabetic foot ulcers and non-ulcerated skin of diabetic patients. In contrast, non-ulcerated, non-diabetic fibroblasts had their Type I collagen located extracellularly. This may indicate the lack of ready availability of Type I collagen in a population prone to poor wound healing, and perhaps the fibroblast phenotype inherent on a patient population may contribute to impaired wound healing through aberrant ECM production[130].

Matrix Metalloproteinases and Tissue Inhibitors of Metalloproteinases

The collagen remodelling in a wound is mediated by specific collagenases, MMPs, and their inhibitors, Tissue Inhibitors of Metallo-Proteinase (TIMPs), which are expressed in fibroblasts under tight regulation. MMP-2 deficient mice have been shown to have reduced neovascularisation after epithelial corneal injury [134]. MMP-9 deficient mice have shown poor arterial remodelling following aortic injury [135], poor angiogenesis at a fracture site[136], and delays in full-thickness excisional wound closure[137]. As discussed earlier some pro-inflammatory growth factors show a second expression peak days after injury, indicating their role during proliferation and remodelling phases. IL-1 contributes to remodelling phase by stimulating MMPs expression, while IL-6 stimulates TIMPs expression. It has been shown that TGF-β stimulates both MMPs and TIMPs expression during remodelling phase, indicating the complex role that growth factors play during wound healing. It is often the balance of growth factors, rather than individual ones that drives biological outcomes[54].

High levels of MMP-8 and MMP-9 have been detected in plasma of burns patients regardless of their degree of burns with peaks within hours from injury. TIMP-1 was also elevated with a peak around 24 hours post injury and its level corelated with 90-day survival[138].

1.3.2. Cellular Interactions

The overlapping phases of wound healing lead to an array of cellular interactions. The collective, coordinated activity of the layers and their various cell types are necessary for wound repair. The dermis and its cells have been shown to coordinate relationships between the cells of the other layers.

Epithelial cells have been shown in *in vitro* assays of human skin equivalents to modify their behaviour following injuries to the basement membrane. Laminin 332, previously known as Laminin 5[28], has been shown to accelerate the assembly of the DEJ and encourage the conversion of epithelial cells to a migratory phenotype to assist in re-epithelialisation. Lineage tracing in mice has also shown that hair follicles are mobilised to the wound area, and contribute to the repair of the damaged epidermis[44]. Incisional wounds in genetic mouse mutants that completely lack hair follicles have a delay in re-epithelialisation compared to their wild-type counterparts[139].

Keratinocyte-fibroblast interactions were investigated with human wound-healing myofibroblasts[140]. The presence of wound healing myofibroblasts in the dermis induced a delay of epithelialisation and a disorganised dermis as seen through immunostaining. Furthermore, basement membrane protein deposition was also delayed when the dermis contained wound healing myofibroblasts.

The relationship between the ECM and dermal fibroblasts has recently been demonstrated in *in vivo* mouse models and *in silico* techniques. The idea that fibroblasts undergo fate restriction (i.e. terminal differentiation) has previously been discussed[34]. However, Rognoni and colleagues demonstrated that fibroblasts have the capacity to come out of quiescence. Their models indicated that the presence of an ECM was sufficient to prevent further fibroblast proliferation, *and* that the presence of an ECM could also encourage fibroblasts out of their quiescent state[141]. This duality of function demonstrates that this inhibition is reversible, may be a source of fibroblast recruitment when skin is injured, and that skin homeostasis is dependent on this complex interplay. Despite this contrast of cellular fate, these two studies emphasize that cellular interactions can occur between cutaneous layer, and cells within a single layer itself.

1.3.3. Deviations from normal wound healing – non-healing wounds

In humans, problems with wound healing can manifest as either delayed wound healing (e.g. from diabetes or radiation exposure) or excessive healing (hypertrophic, keloid scars)[55] Local factors (e.g. infection, ischaemia and mechanical trauma) as well as systemic factors (e.g. chronic diseases such as diabetes, and nutritional deficiencies) are involved in the cycle of non-healing wounds[142].

Full-thickness wounds in rabbit models have demonstrated that exacerbated and prolonged inflammation (as measured through RNA and protein expression via Q-PCR and ELISA) impairs wound healing and increases scar formation seen histologically[143].

Punch biopsies from chronic diabetic wounds and chronic venous ulcers in humans demonstrated a prolonged presence of ECM proteins compared to an acute wound model[144]. Proteolysis of the ECM is an important step during normal wound healing, allowing for the removal of debris and encouraging cell migration and angiogenesis[54]. However, overactivity of this proteolysis could result in excess tissue degradation, and prolongation of healing.

Proliferation assays of human fibroblasts from chronic wounds have demonstrated that they produce similar amounts of ECM compared with normal fibroblasts, indicating that it is through matrix processing and ECM remodelling that a chronic wound may persist[145].

Chronic wound fluid contains high concentrations of active neutrophil elastase, which is responsible for the degradation of proliferative cytokines such as PDGF-BB and TGF-β1[146]. It also contains a significant higher concentration of MMPs, which remove ECM[80]. TGF-β also upregulates the expression of tissue inhibitor of metalloproteinases (TIMPs) and decreases MMP production. In humans, other cytokines such as IL-1β, IL-6 and TNF-α induce the expression of some MMPs[147], and upregulates TIMP[54]. It appears that the milieu of the chronic wound provides an array of aberrant cellular interactions.

Extensive deep burn wounds will not heal in a timely fashion according to the classic models of acute wound healing. This is largely because epithelial elements at the edge of such wounds will only be able to proliferate to cover extensive areas over a prolonged period of time, during which the wound will become chronic. In the context of available surgical resources, such wounds will be skin grafted in order to achieve healing. Severe burns induce a raft of systemic physiologic changes, including insulin resistance, hypermetabolism and an hyperinflammatory state[148]. Severe trauma in general causes an increase in endotoxins, systemic IL-1β, IL-6 and TNF-α, and reactive oxygen species, resulting in sustained inflammation[149].

Early burn wound excision has been shown to significantly reduce inflammation as well as the risks of infection, wound sepsis, and multi-organ failure[5, 150] with benefits in reducing patient mortality and length of hospital stay[150-152]. As a result, burns wound excision and subsequent autologous grafting remains the gold standard of care for deeper burns.

Skin grafts as a treatment for burns was first noted post-second world war[4], and provides the epidermis that contributes to wound healing. The destruction of the cutaneous barrier and the altered immune status leads to an increased susceptibility to infection and consequent sepsis, hence the need for expeditious wound coverage. The acute wound model that has been extensively investigated provides a dilemma when the size of the wound to heal overwhelms the healing mechanisms available. This is none more evident than in extensive,

large total body surface area (TBSA)% burns when the percentage area of injury surpasses the area available as a donor site.

The severity of burn wounds can be estimated by TBSA% as calculated in multiples of nines ("The Rule of Nines"), and by the depth of the burn. The larger the percentage of TBSA injured, and the deeper the injury, the more severe the burn. It is more difficult to facilitate wound spontaneous wound repair with a higher TBSA of burn, and it is also more difficult to find appropriate donors for skin grafts. The following figures outline this grading scheme.

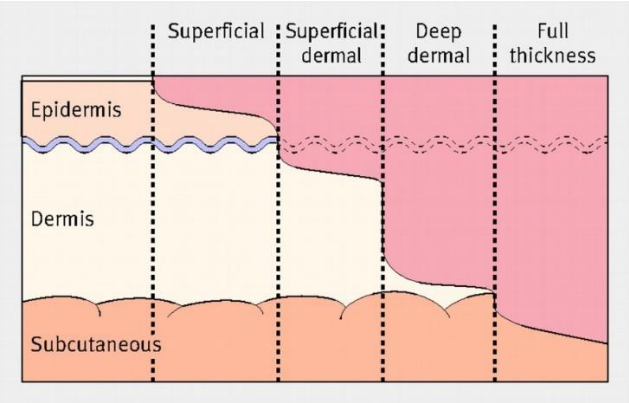

Figure 1.7: Burn Depth and injured layers. Enoch et. al. 2009[153].

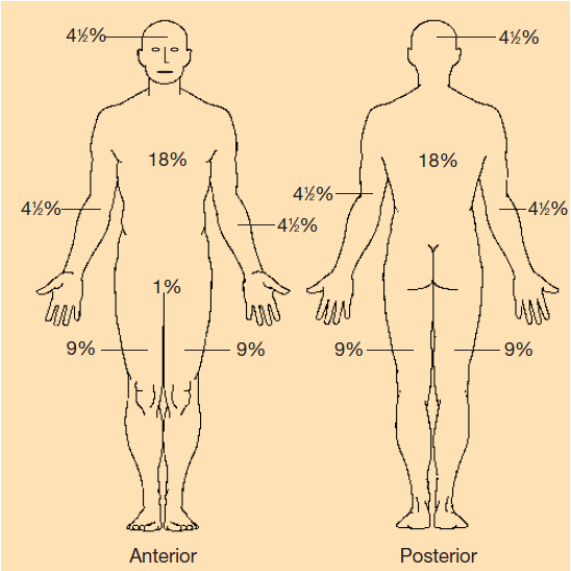

Figure 1.8: The Rule of Nines. Johnson et. al. 2003[154].

Growth factors and Cytokines in Burn Wounds

In addition to mitigating infection and sepsis risks, early excision and grafting of burns is undertaken to avoid the presence of granulation tissue and subsequent future scarring issues[155].

Several studies in humans have investigated the temporal relationship of several pro- and anti-inflammatory cytokines during the first few days to weeks post a burn injury. In this hyperinflammatory state, plasma levels of IL-6, IL-8, IL-10 and TNF-α and granulocyte colony stimulating factor (G-CSF) were elevated in burns patients compared to non-burns patients at all observed time points in one study[156]. IL-6, -8 and -10, although fluctuant in their levels, all peaked at Day 1 post burn, whereas TNF-α peaked at Day 7. In addition, a general trend observed was that the higher the burn TBSA%, the higher the levels of the aforementioned cytokines. Fatal burns also saw significantly higher levels of IL-6, IL-8 and GCSF compared to non-fatal burns patients[157].

This elevation of cytokine plasma levels post burn was also seen in the paediatric burns population[158]. The prognostic ability of cytokines has also been investigated, and of those mentioned in this review, IL-6 may be used as a prognostic indicator of mortality in burns patients[159]. It is interesting to note that these cytokines are generally considered to be inflammatory cytokines, and to the best of our knowledge, a study that investigates the continuous temporal profiles of proliferation and remodelling cytokines in burns patients is yet to be undertaken.

The fluctuating levels of inflammatory cytokines post injury is also evident in mouse models[67, 79]. A mouse model for partial-thickness burn wounds demonstrated peaks of IL-1 and TNF- α at day 3, and a peak of IL-6 at day 1, which sharp declines of all cytokines at Day 7 and minimal amounts between Days 10-14. This model establishes that a thermal burn induces a strong pro-inflammatory response that subsides prior to burn closure; however, this response leads to sustained effects on downstream scar remodelling.

1.3.4. Skin Grafts

There is paucity of information available as to how a skin graft takes on a biomolecular level, and how it modulates wound healing.

There exist general principles as to how a skin graft heals. To have graft take, skin grafts require that the recipient wound has a graftable bed, i.e. one with a functioning vascular supply[160]. Therefore, skin grafts will not take on exposed bone, tendon or cartilage, but will take on periosteum, paratenon, and perichondrium. Like wound healing, graft healing has been proposed to consist of phases: (i) adherence, (ii) plasmatic imbibition, (iii) revascularisation, and (iv) remodelling.

Burleson first described an elastin-fibrin bond in 1972[8] using rat models xenografted with partial-thickness porcine skin grafts. This acute stage of adherence was seen to occur within the first 24 hours of grafting. Concurrent to this, the first 48 hours sees the extrusion of plasma from graft recipient site capillaries as seen in rat[9] and guinea pig models[161]. This plasma is thought to either nourish the graft or merely keep the graft moist and to keep the graft vessels open whilst circulation is being established. After 48 hours, blood vessels can be seen within the fibrin layer of the graft. The formation of these blood vessels was thought to either be by inosculation (the kissing of a graft and a wound bed vessel)[9] or by neovascularisation first from the recipient bed growing into the graft[7]. Hypoxia inducible factor (HIF-1α, which stimulates the expression of VEGF) increased the macroscopic take rate of autologous skin grafts in mouse models. HIF-1α knockout mice had significantly impaired graft take. The mechanisms through which this occurs was not elucidated, and histological staining showed no difference in epithelialisation between the knockout and wild-type mice[162].

The graft then undergoes a remodelling phase, where the graft itself regains the architecture of normal skin. By day 6, lymphatic channels have been established, and by day 7, collagen replacement has begun, increasing to normal levels by 42 days. Further vascularisation and remodelling continues for months following, and sensation may begin to appear at 3 weeks[163].

These insights have been achieved largely through macroscopic observations of grafted wound beds, and more recent studies have only sought to highlight wound factors that may increase or contribute to visual graft take. Such external wound factors include the use of negative pressure wound therapy to encourage plasmatic imbibition or to create a well-vascularised wound bed prior to grafting[164-166]. A review by Schneider *et. al.* (2007)[167] ultimately concluded that an intrinsic wound bed factor to encourage increased graft take is an alkaline wound bed milieu.

In research where cellular interaction was investigated, no protein confirmation of biomarkers was undertaken. Allografting human keratinocytes onto partial thickness burn wounds post-debridement demonstrated immediate shifts in integrin expression. It allowed the epidermal integrin expression to normalise rapidly, shifting the epidermis from an inflammatory to a regenerative state as investigated through the histology of human wound biopsies post graft[168]. This has also been demonstrated when cultured epithelial autografts were transplanted onto a homograft dermis, along with regeneration of the wounded DEJ[169]. Accelerated assembly of the DEJ has been shown to accelerate wound healing (see Section 1.2.1).

Rudolph in 1975[170] investigated full-thickness skin grafts in rats (using light and electron microscopy) and concluded that the application of a skin graft rapidly decreases the number of wound bed myofibroblasts. This is not through the inhibition of myofibroblast formation, but rather by speeding up the completion of their life-cycle. Desmouliere *et. al.* (1995)[171] found that, in rats, the senescence of granulation tissue is mediated by apoptosis; this also mediates the decrease in cellularity, particularly of myofibroblasts, during the transition between granulation tissue and scar (observed to begin at around day 12 post wounding). This finding was mimicked when a similar full-thickness wound was applied to a similar rat model, and the wound bed covered with a local rotation flap[172]. However, this apoptosis, as seen via *in situ* labelling of fragmented DNA and electron microscopy, was seen to commence at day 3 post wounding. This opens the door for the idea that skin grafts modulate the wound bed by altering the wound healing trajectory as seen in the classical model of wound healing; but this is yet to be investigated and confirmed on the protein and RNA levels.

In addition to the role of MMP in ECM remodelling during spontaneous wound repair, these proteases are also involved in remodelling vasculature in grafts. Immunofluorescence analysis illustrated MT1-MMP was present at the emerging wound vessel sprout-tips, indicating that a possible role for MT1-MMP in endothelial growth during inosculation in an autologous FTSG mouse model[173]. Whereas, MMP-2 initially rose within the wound bed followed by predominating within the skin graft at 96 hours suggesting a role in remodelling as opposed to the role of angiogenesis. At 24 to 48 hours, MMP-9 had upregulated expression concentrated in the upper dermis of the graft at the level of non-perfused vessels, and was

associated with disorganised cell morphology, implying a role in the ordered regression of the pre-existing graft vasculature[174].

A recent study by Jalili *et. al.*[175] used split-thickness skin grafting in porcine models to investigate the possible sources of the cells that fill the wound bed below the graft. Their immunohistochemical findings suggest that the new skin under the graft regenerates in a "bottom-up" approach, undergoing proliferation and demonstrating α-SMA-positive expressing cells. In addition, the immune cells infiltrating the wound bed were thought to acquire the capacity to become skin cells, as early as day 10 post-wounding.

1.4. Dermal Matrices

The limited availability of donor skin grafts in large burns becomes a significant challenge. Split-thickness skin grafts are often meshed to maximise the harvested skin, but can cause contractures. The thickness of the skin graft and the depth of the underlying wound bed affects the extent of scar tissue formation[176].

Since the 1980s, bioengineered skin substitutes have been developed as an adjunct or alternative to the use of the patient's own skin in the context of the aforementioned limitations often found with burn wounds. More specifically, dermal substitutes are biomatrices that fulfil the functions of the cutaneous dermal layer when the dermal layer has been destroyed[177]. They act as matrices or scaffolds, and promote new tissue growth and enhance wound healing[178, 179], and may improve the resultant scar quality[180].

There exist various bioengineered skin substitutes and dermal templates in the market[177, 179], as the type of scaffold can influence the delivery of wound healing cytokines to the wound bed[181]. The scaffold being investigated in this research project is NovoSorb Biodegradable Temporising Matrix (BTM). BTM is a fully synthetic dermal template in the form of biodegradable polyurethane foam with a temporary non-biodegradable polyurethane seal.

The mechanism through which matrices heal wound beds is also another question yet to be answered. Greenwood *et. al.* in 2009[182] revealed that neovascularisation with Integra results in large vessel, high volume, rapid flow circulation contrasting markedly from normal inosculation process in skin grafts and the capillary circulation in normal skin. Our laboratory in 2016[183] revealed earlier neovascularisation of BTM compared to Integra, a dermal matrix

comprised of human collagen I and GAG. The biomolecular profile of both synthetic and autologous graft take is yet to be investigated.

1.5. The Mouse Model

1.5.1. Animal Models in Research

There is currently no ideal model of cutaneous wound healing[184]. *In vitro* models of wound healing serve to isolate specific elements of the wound healing process, so they can be studied in a simpler system.

Results therefore need to be extrapolated *in vivo*. There are various *in vivo* models; and although different mammals can have differing wound healing characteristics, wound healing is conserved across evolution, so observing lower species can inform us of this basic biology[185].

Approached from structural perspective – hair density, blood supply, relative epidermal-dermal thickness and skin laxity – pig dermis is structurally the most similar to that of humans[184, 186, 187]. However, porcine models are cumbersome, expensive, and genetically heterogenous[143]. Other models include rat and rabbit models; but the most commonly used animal model is the mouse, as they are easy to handle and maintain, produce rapidly, and are economically more acceptable.

As human and murine skin have the same layers of cells in the epidermis and dermis, there are similarities in skin healing between the two species despite the great different in thickness of layers[187]. However, mice have a panniculus carnosus – similar to the human muscle of the plastysma – a thin layer of muscle resting directly under their hypodermis. As a result, mice wounds heal via contraction as opposed to re-epithelialisation seen in humans[185, 188]. In general, mice have greater hair follicle density which facilitates a faster wound repair compared to wound repair in humans. One way to avoid cutaneous contraction of open wounds in mice is to splint the wound open with silicon or metal[184, 189, 190]; and one way to avoid the greater hair follicle density is to use a hairless mouse model.

1.5.2. The SKH-1 Hairless Mouse Models

The immunocompetent, outbred albino hairless SKH-1 mouse is the most widely used in dermatological research as it allows for the ready manipulation of the skin and easy visualisation of the cutaneous response.[191] Its lack of hair is similar to human skin, and has an

epidermis and dermis similar to that of humans. Its outbred status means, however, that the mouse will reject anything not autologous, and for a mouse widely used in research, its genetic status remains relatively uncharacterised.

1.6. Hypotheses, Aims and Methodology

1.6.1. Hypotheses

We hypothesise that:

i. Skin grafting facilitates wound repair by altering the wound micro-environment such as modulating the inflammatory response.
ii. A synthetic matrix graft allows for the wound to repair by similar changes in the wound micro-environment as autologous skin graft.

1.6.2. Aims

i. To establish a mouse model for studying changes in wound microenvironment in skin grafting over time.
ii. To identify key molecular markers to aid in the investigation of wound healing progression.
iii. To identify biomolecules associated with successful graft take.

1.6.3. Study Design

Our study will use male SKH-1 mice, aged approximately 8-10 weeks and weighing ≥21g at the time of surgery. Male mice have more subcutaneous fat particularly at the flanks, which can thus facilitate a greater ease in the surgical portion of the experiments.

Arm 1: Full-thickness wound model

The aim of the first arm is to establish and confirm the stages of full-thickness wound healing in this mouse model. The results of this study will guide the experimental arm.

Two full-thickness wounds will be made on the dorsum of the mice under general anaesthesia and splinted open with a pre-made silicon ring, and sutured on to prevent contraction following a similar protocol from Dunn *et. al.*[190]

The mice will be monitored for the duration of the experiment, and will be euthanised at their endpoints by CO_2 inhalation. The wounds, and a small margin of surrounding tissue will be collected as well as tissue near the tail (unwounded host tissue) from the mouse after euthanasia for histological, protein and RNA analysis.

Arm 2: Autologous full-thickness skin graft and synthetic dermal graft models

The second arm is similar to the first, where mice will be given two wounds and culled at varying timepoints. Differing in this arm, however, is that we will be giving mice a graft alongside the full-thickness wound. This graft will either be an autologous full-thickness skin graft or a synthetic graft, one of NovoSorb BTM. The mouse's endpoint will be one of three: a day that coincides with the inflammatory phase of wound healing, a day that coincides with proliferation, and a day that coincides with an early remodelling timepoint. These days will be dictated by the results of the first arm of the study. Again, the mice will be monitored for the duration of the experiment, and will be euthanised at their endpoints by CO_2 inhalation. The wounds, and a small margin of surrounding tissue will be collected as well as tissue near the tail (unwounded host tissue) from the mouse after euthanasia for histological, protein and RNA analysis.

1.7. Transition into the Clinical Setting

Ehrlich's perspective article in 1996[128] stated that "graft take replaced the healing process for the closure of the defect"; but perhaps, a skin graft is merely another method of healing process that modulates not only the wound bed, but the temporal trajectory of the classic model of wound healing. Investigating the microenvironment in full-thickness autografted and synthetically grafted wounds may relay significant information as to the method of wound healing attributable to skin grafts and synthetic grafts. Identifying the minimal requirements for a graft to take could feed back into the composition of comparable skin substitutes.

Furthermore, to outline why a particular dermal substitute is successful in the context of burns injuries would convey a better knowledge as to why dermal cells behave the way they do when injured. A better understanding of the way dermal cells behave in differing cell-matrix environments could pave the way for a wider usage of these dermal substitutes not previously approached in the context of not only Burns injuries, but in the realm of Reconstructive surgery.

CHAPTER 2: MATERIALS AND METHODS

2. Methods

2.1. The Mouse Model

All experiments were performed using male SKH-1 mice. SKH-1 mice were acquired through a pre-existing collaboration with researchers from Baker IDI Institute (Melbourne, Australia). Mice were between 8-10 weeks old at time of surgery and weighed ≥21g. All mice arrived at the Precinct Animal Centre (PAC) seven days prior to their surgery date to acclimatise to the environment of the holding room. On this day, mice undergo a health check and their weight recorded. At least two days prior to their surgery date, mice were housed in divided cages using sterile caging equipment, given Neomycin drinking water in dark water bottles, and given wet mash to acclimatise to the texture of food.

2.1.1. Ethics

All experiments were performed on animals in accordance with the guidelines set by the Animal Ethics Committee (AEC) of Monash University and Baker Institute, Melbourne (AEC E/1920/2019/A).

2.1.2. Neomycin drinking water

The stock solution of Neomycin (100x, 180mM) was prepared by adding Neomycin powder (Neomycin Trisulfate, Sigma-Aldrich) to sterile filtered water (MilliQ) in an autoclaved bottle and left to stir and dissolve using a magnetic flea. As Neomycin is light sensitive, all bottles were wrapped in aluminium foil. The drinking water solution of Neomycin (1x, 1.8mM) was prepared by acidifying 1L of MilliQ using hydrochloric acid (HCl) to a pH of 2.5, adding 10mLs of the 100x stock solution of Neomycin, and filter sterilised using a vacuum filter (Nalgene, Merck).

2.1.3. Mouse surgeries and dressing changes

Fresh paracetamol (in 300µl of phosphate-buffered saline (PBS), 150mg/kg) and buprenorphine (100µl in PBS, 0.01mg/kg) injections were prepared. Extra paracetamol at 50mg/kg was made to be added to the mash on the day of surgery. Two buprenorphine syringes were prepared for each mouse, as they required a second, post-operative dose of analgesia 8-12 hours post-surgery.

Mice were then transported from their holding room to PAC theatre. The theatre set-up included a recovery area (a sterile recovery cage on a heat rack) and a sterile theatre table on

a heat rack with an anaesthetic machine and an instrument bench. Prior to the operation, mice underwent a final pre-surgery health check and their weight recorded.

Mice were anaesthetised using an inhaled anaesthetic (isoflurane, (2-chloro-2-(difluoromethoxy)-1, 1, 1-trifluoro-ethane)) at 3L/min in an induction chamber. A mouse was considered anaesthetised when the animal was breathing steadily, does not right itself when the induction chamber was tilted, and when gentle pressure on the foot pad and tail does not elicit a response. Following confirmation of anaesthetisation, the mouse was moved from the induction chamber onto a nose cone, with the isoflurane maintained at 1.5L/min. Eye gel was then applied.

A sterile field was set up around the mouse. The area of excision (on the dorsal side of the rib cage, 1cm on either side of the midline at around the flanks of the mouse) was cleaned with 80% alcohol (EtOH, v/v) and PBS. Two 1.5cm circles were marked on the mouse's skin using a round template such as a biopsy punch and an inkpad. The tissue was excised using a pair of surgical scissors.

Mouse surgery for both arms of the study were similar, however in the second arm, only one wound was treated, either with an autologous full-thickness skin graft (FTSG) or the synthetic Biodegradable Temporising Matrix (BTM).

In FTSG group, the skin excised with surgical scissors was turned 180 degrees and sutured onto one of the two wounds with monofilament nylon sutures (size 6/0 Dafilon nylon monofilament sutures, Warner & Webster) with 4 to 6 simple interrupted sutures. The adjacent wound was left as an ungrafted full-thickness wound. The remaining tissue from the untreated wound ("unwounded") was collected and immediately immersed in TRI Reagent (Sigma-Aldrich) for processing later that day (see section 2.3.1).

In the BTM group, BTM was sutured onto one of the two wounds instead of the excised skin in the same fashion as above. The BTM was pre-cut to wound size prior to surgery and soaked in 0.9% Normal Saline 30 minutes prior to use.

Two custom-made silicon rings (Press-to-stick silicon, Life Technologies/ThermoFisher, P-18178) were adhered to the outer edges of each wound using skin glue (Histoacryl glue, BRA1050044) and sutured in place along the outer circumference of the ring with the

monofilament nylon suture with 6 to 8 simple interrupted stitches. Prior to dressing, photographs of the mice were taken using a camera, measuring the size of the wound using digital electronic surgical calipers (Sterihealth Labs).

The two wounds were dressed following the final suture with one layer of a paraffin impregnated gauze (Jelonet, Smith & Nephew), two layers of a non-absorbent but porous wound dressing (Surfasoft, Otago Healthcare) and dry gauze. These were fixed to place with an adhesive, waterproof dressing (Tegaderm, 3M Company), and a self-adherent bandage (Coban, 3M Company) was applied to hold the bandage in place.

Mice were given an 300µL intraperitoneal injection of non-opioid analgesia (paracetamol, 3mg/ml in saline) and a 100µL subcutaneous injection of opioid analgesia (buprenorphine, 0.01mg/kg). A flush of oxygen was delivered to the mice, and placed in the recovery cage and closely observed while they regained consciousness. Once the mice started to move around, they were placed in their home cages. Animals were returned to their holding room at the end of the surgery day and were monitored on a daily basis post-operatively (see Appendix 2: Post-surgery Animal Monitoring Sheet). Another dose of buprenorphine in as a 100µL subcutaneous injection was given to the mice 8-12 hours post their first injection as an adjunct pain relief. Carprofen (5mg/kg) was available as a 100µL subcutaneous injection if the mouse monitoring indicated that the mice needed extra analgesia due to their pain.

Dressing changes were performed on the mice on days 5, 10 and 15 post-op. The anaesthetic, intra-operative monitoring and dressing regime was as the primary operation. Photographs were also taken at these time points. An intraperitoneal injection of paracetamol was administered to these mice following their dressing changes.

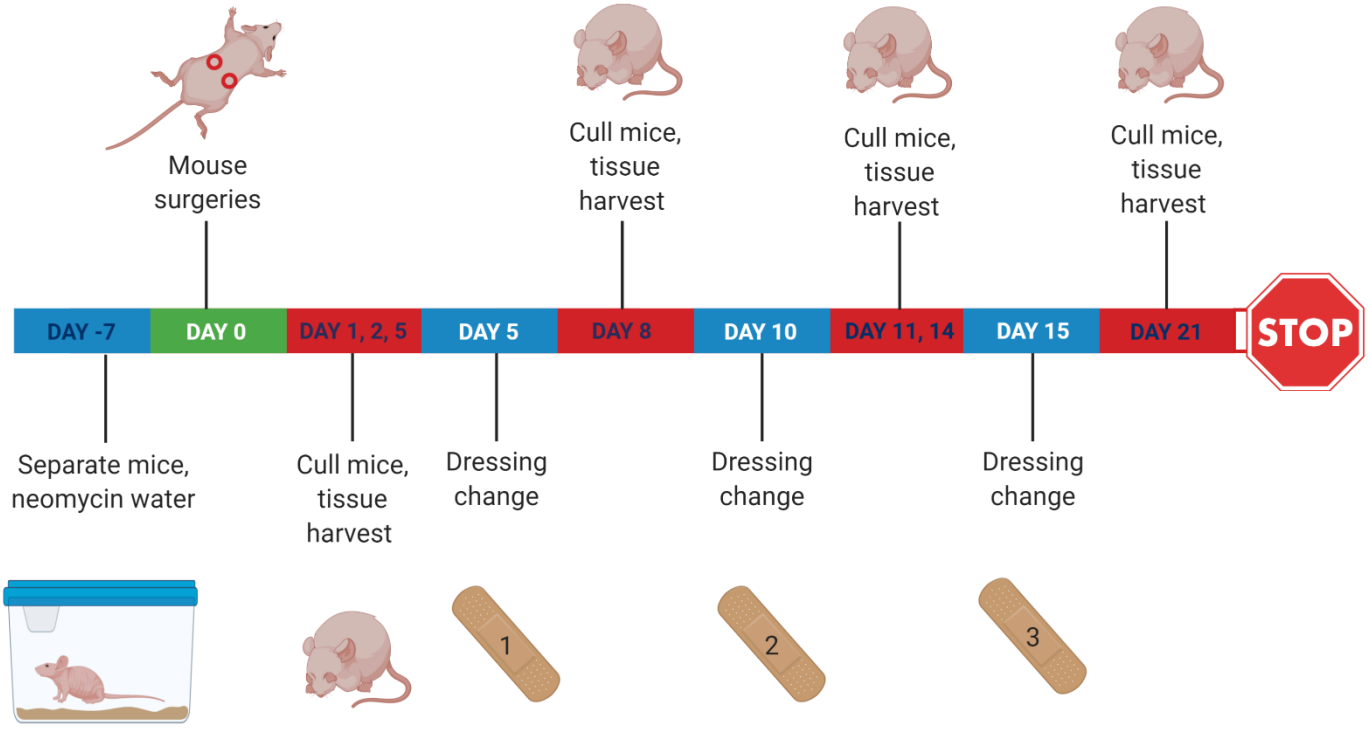

Figure 2.1: (a) Experimental timeline for the full-thickness wound model. Mice were culled at endpoints that coincided with inflammatory, proliferative, and remodelling timepoints.

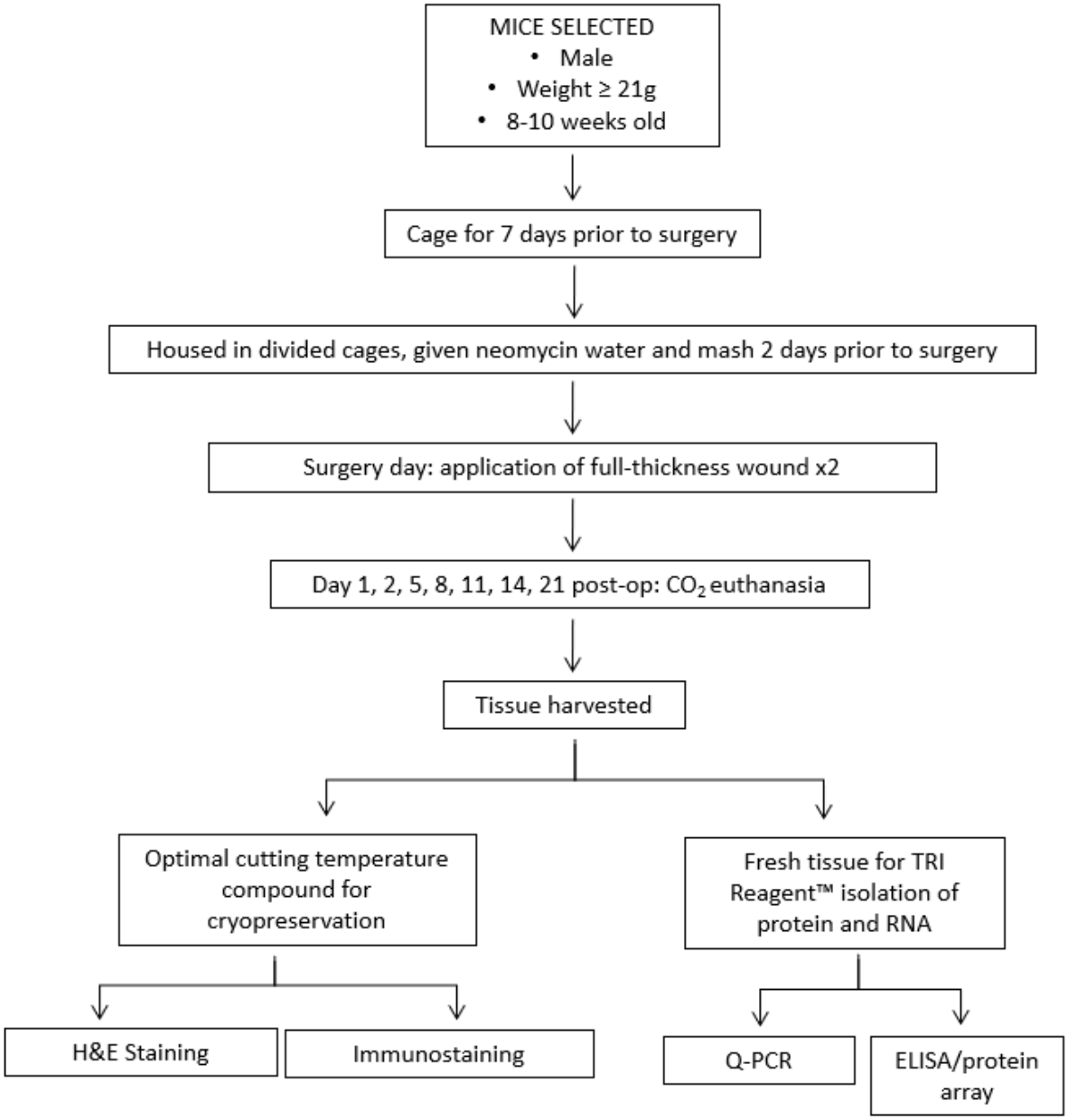

Figure 2.1: (b) Methodology flowchart for the full-thickness wound model.

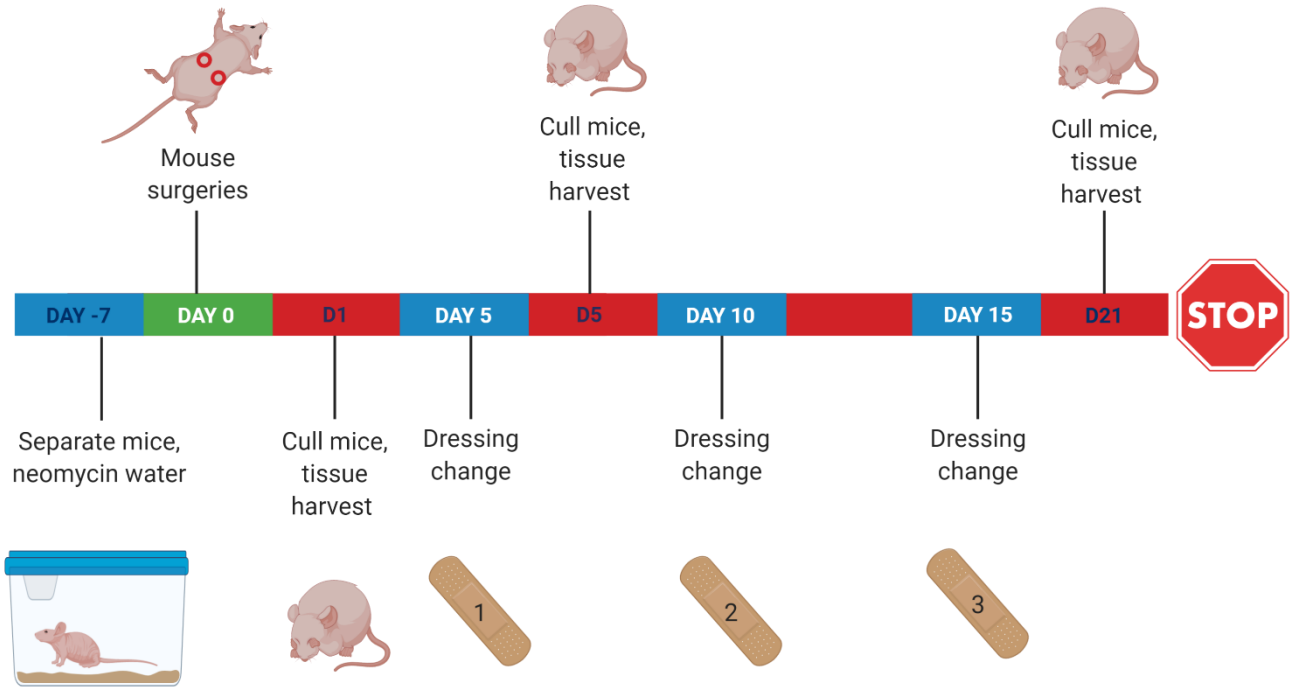

Figure 2.2: (a) Experimental timeline for the autologous- and synthetic-grafted wound models. Mice were culled at three distinct timepoints as guided by the results of the full-thickness wound model.

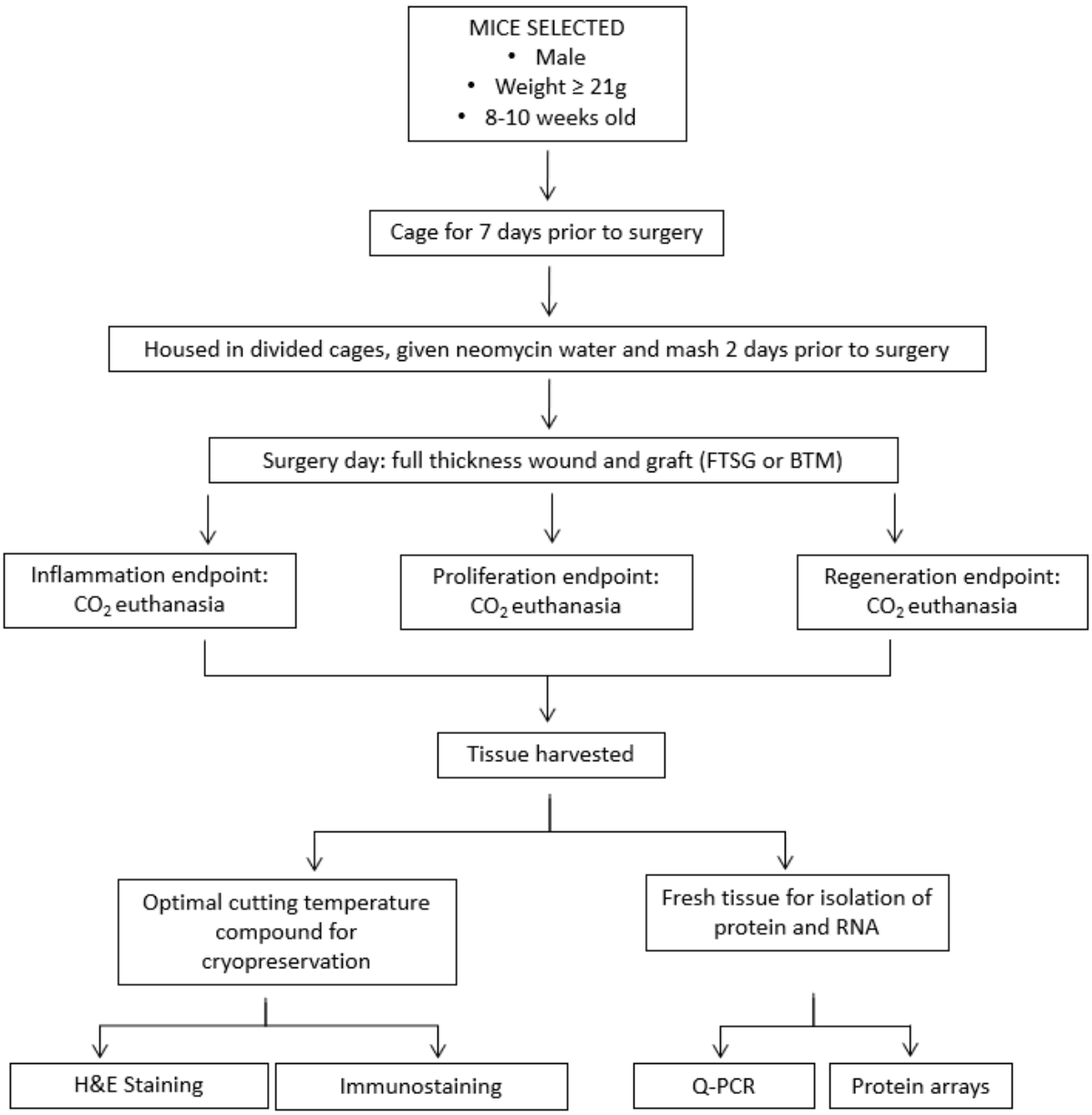

Figure 2.1: (b) Methodology flowchart for autologous- and synthetic-grafted wound models.

2.1.4. Euthanasia

Mice were euthanised at their assigned end-points using a CO_2/CO_2 gas mix. Mice were placed in the chamber and the CO_2 turned on at a low flow rate (25-30% of the volume of the chamber per minute). The mouse was monitored until the animal had stopped breathing. After its final breath, the CO_2 was left on for a further 1-2 minutes and then turned off. Heartbeat, respiration and pain reflexes were checked to verify death. The mouse was given a pneumothorax by piercing its diaphragm below the heart as a secondary measure of euthanasia to ensure death.

2.2. Excision of Tissues

Following euthanasia (See Section 2.1.4), dressings were removed from the mouse and photographs taken of the wounds with caliper measurements prior to removal of the silicon rings. The two wounds (left – "L" and right – "R") and its surrounding host tissue were excised along with skin from the tail end of the mouse. These were laid flat onto filter paper placed into the wells of a six-well plate and carefully soaked in PBS. The wound bed ("wound") tissue and the tissue from the tail ("tail") were halved for processing with TRI Reagent and for tissue embedding in OCT for histological cryopreservation, as outlined below.

Tail, FTSG and tissues excised from the wounds at day 21 for both conditions (FTSG or BTM) were separated into epidermis and dermis as follows. Tissues were soaked in 1M of sodium chloride (NaCl) following halving and gently rocked for 1.25 hours, prior to processing the specimens with TRI Reagent, snap freezing or saving in RNA-later. To separate the layers, once the specimen had soaked in NaCl, it was turned dermis side up and the dermis scraped off from the epidermis until the shiny underside of the epidermis was seen.

Tissue specimens (L, R and T) were prepared in TRI Reagent ("TR") prior to RNA and protein purification on the day of tissue excision following animal euthanasia.

2.2.1. Tissue Processing: using TRiReagent

Specimens were homogenised in TR (1000µL per 50-100mg of tissue) using a tissue homogeniser. The homogenate was then centrifuged at 12,000 *x* g for 10 minutes at 2-8°C to remove the extracellular material such as hair. These cell suspensions were either used immediately to purify RNA and proteins, or stored in -80°C for up to 1 month.

Following tissue homogenisation, the samples were left to stand for 5 minutes at room temperature prior to adding 100µL of 1-bromo-3-chloropropane (Sigma-Aldrich) per 1000µL of TR to the Eppendorf tube, shaken vigorously for 15 seconds, and allowed to stand for 5 minutes at room temperature. These were then centrifuged at 12,000 *x* g for 15 minutes at 2-8°C to separate the sample into its three phases: a bottom pink organic phase containing protein, a middle white interphase containing DNA, and a top clear aqueous phase containing RNA.

Purification of RNA and proteins will be discussed in later sections (see Section 2.4.1: RNA extraction and purification, and: Section 2.5 Protein extraction and purification of tissue lysates).

2.2.2. Tissue Processing: snap freezing

Another method was used to process the tissues to maximise the protein and RNA yield of specimens. Once the tissues were halved, and the half soaked in 1M NaCl for epidermal and dermal separation, the half was bisected again (into quarters) for RNA and protein. The quarter for RNA was stored in RNA later and soaked overnight prior to storing at -80°C prior to extraction. The quarter for protein was immediately snap-frozen in dry-ice and stored in -80°C.

2.3. Histology Methods

2.3.1. Cryopreservation of specimens

Tissues for cryopreservation were lightly fixed in 4% Paraformaldehyde (PFA), 20min, washed in PBS and placed in a cryomold with OCT overnight. The skin grafts were frozen on dry ice while keeping them in profile the next day. Specimens were stored at -80°C until use for cryotomy.

2.3.2. Haematoxylin and Eosin Staining

Cryopreserved specimens were cut using a cryotome and left in room temperature overnight prior to staining. Slides were then washed in tap water for 2 minutes prior to staining with Harris's Haematoxylin for 30 seconds, then washed again in running tap water for 30 seconds. The slides were dipped in Acid Alcohol for 1 second, washed in running tap water for 30 seconds, then dipped in Scott's tap water for 10 seconds. The slides were washed in running tap water again for 30 seconds, and stained with Eosin for 1 minute. Following this, the slides were washed in absolute alcohol three times for 2 minutes each and then

dehydrated in xylene three times for 2 minutes each. Slides were then mounted with DPX (Dibutylphthalate Polystyrene Xylene, Merck), and left to dry overnight prior to imaging.

2.3.3. Masson's Trichrome Staining

Masson's Trichrome staining was performed with thanks by the Monash Histology Platform Services (Clayton, Melbourne, Victoria). Briefly, cryopreserved specimens were cut using a cryotome at 7µm thickness per section. Sections were then brought to water, and placed in Bouin's fixative either overnight at room temperature or 1 hour at 60°C. Slides were then washed in running water prior to staining with Celestin blue for 5 minutes, and then washed again. Slides were placed in Weigert's haematoxylin for 30 minutes, washed in tap water following, and differentiated in acid alcohol briefly. Slides were washed again in running tap water for 10 minutes before staining with Biebrich scarlet-acid fuchsin for 5 minutes. Five percent tungstophosphoric acid was applied to the slides with brief washed in distilled water before and after. These were then stained with Aniline blue staining solution for 5 minutes, washed in 1% aqueous acetic acid for 3 minutes, and then dehydrated through 3 changes of 100% ethanol. Specimens were cleared in 3 changes of xylene period to mounting with DPX, and left to dry overnight.

2.4. RNA Methods

2.4.1. RNA extraction and purification

RNA purification was firstly undertaken using the TriReagent instructions. Extraction was then undertaken using the Qiagen RNeasy kit (Qiagen, 74136) following streamlining methods. Following TR separation of the specimens into three phases, the aqueous phase was aspirated into a new RNase-free tube, with care to avoid the contaminants of the middle and bottom phases. The middle interphase was discarded, and the protein phase was placed in the fridge for later precipitation.

For specimens directly kept in RNA-later, these were taken out of the -80°C freezer, thawed on ice, and homogenised in 800µl of the RLT buffer provided in the Qiagen RNeasy kit before proceeding with the following steps.

An equal volume of 100% EtOH was added to the RNA (extracted either by TR or by RLT buffer homogenisation), mixed, and 700µl loaded into an RNeasy column seated in a collection tube. Samples were spun at 8,000 *x g* for 30 seconds at room temperature, and the flow-through

discarded. Next, 700µl of the RW1 buffer from the kit was added into the columns, spun 8,000 *x* g for 30 seconds at room temperature, and the flow-through discarded.

The column was transferred into a new tube, 500µl of the RPE buffer (with added ethanol as per manufacturer's instructions) from the kit added to the tube, and spun at the above parameters with the flow-through discarded. 500µl of the RPE buffer was added again to the columns, spun at 8,000 *x* g for 2 minutes at room temperature, and the flow-through discarded. The column was again spun for 1 minute at 8,000 *x* g to remove the remaining buffer from the column.

The collection columns were transferred to a new 1.5mL tube, and 50µl of RNase-free water pipetted directly onto the column membrane. The samples were allowed to sit at room temperature for 2 minutes, and then spun at 8,000 *x* g for 1 minute to elute RNA. This addition of 50µl of RNase-free water was repeated to elute a total of 100µl of RNA. Samples were stored at -80°C.

A Nanodrop Spectrophotometer (Thermofisher) was use to evaluate the quantity of RNA eluted (ng/µL), as well was the $A_{260/280}$ ratios to assess the purity of the final RNA product. Later quantitation involved use of the Quantus™ Fluorometer machine and kit (Promega), which required use of the QuantiFlor® RNA System kit (Promega, Product no. 287813).

2.4.2. Complementary DNA synthesis

Complementary DNA (cDNA) was synthesised using the GoScript™ Reverse Transcriptase Master Mix and Oligod(T) kit (Promega, A2791). cDNA for the wound sample (e.g. SG001L) as well as the no RNA (i.e. SG001L no RNA) and no reverse transcriptase (i.e. SG001L no RTC) negative controls were synthesised.

Volumes of the GoScript™ Buffer, GoScript™ Enzyme mix, and nuclease free water to add to the microtubes (0.2mL, Axygen Corning) were as per below. The template RNA for a 500ng concentration was also added to the microtubes for wound sample and the no RTC negative controls. The enzyme mix was omitted from the no RTC negative controls.

Component	**Volume (µL)**		
	sample	No RTC	No RNA
Nuclease-free water	4	6	4

GoScript™ buffer	4	4	4
GoScript™ Enzyme	2	0	2
+	+		
Template RNA (=500ng)	*x*	*x*	0
Nuclease-free water to a final volume of	10 - *x*	10 - *x*	10
Final microtube volume	***20***		

All labelled tubes were vortexed and briefly centrifuged. A BioRad ThermalCycler was used to synthesise cDNA according to the following program:

1. 25°C for 10 min (annealing)
2. 42°C for 60 min (reverse transcription)
3. 99°C for 5 min (denature RTase)
4. 4°C for 5 min (cooling)

cDNA was either used immediately for PCR or stored at -80°C until required.

2.4.3. Primer Selection

Primer pairs for all target genes of interest were selected by literature search through the PubMed online database. Criteria for primer selection were as follows:

- The primer should span an exon-exon junction to include an intron, in order to avoid the risk of genomic DNA (gDNA) amplification.
- Melting temperatures (T_m) to be between 60-64°C with an ideal temperature of 62°C. The two primers should not differ by more than 2°C.
- A guanidine/cytosine content between 30-65% with an ideal of 50%.

For a full list of primer pairs (Sigma-Aldrich) including reference housekeeping genes, please see Table 2.1. Lyophilised Primers were spun down prior to adding the amount of nuclease free water required to reach a 100µM stock concentration as per the manufacturer's instructions. A final working concentration of 10µM was used for all PCR analysis.

Gene of interest	*Reference*	*Forward primer*	*Reverse primer*
IL-1β	*Wang et. al. 2016*[192]	5'-TTGACGGACCCCAAAAGATGAAG-3'	5'-TTCTCCACAGCCACAATGAG-3'
TNF-α	*Brown et. al. 1995*[106]	5'-AGCCCACGTCGTAGCAAACCACCAA-3'	5'-ACACCCATTCCCTTCACAGAGCAAT-3'
IL-6	*Bryan et. al. 2005*[69]	5'-ATGAAGTTCCTCTCTGCAAGAGACT-3'	5'-CACTAGGTTTGCCGAGTAGACTC-3'
TGF-β1	*Brown et. al. 1995*	5'-GCTAATGGTGGACCGCAACAACG-3'	5'-CTTGCTGTACTGTGTGTCCAGGC-3'
PDGF-BB	*In-house*	5'-CGGAGTCGAGTTGGAAAGCTC-3'	5'-AATAACCCTGCCCACACTCT-3'
VEGF-A	*Wise et. al. 2018*[193]	5'-GCAGGCTGCTGTAACGATGAAG-3'	5'-GCTTTGGTGAGGTTTGATCCG-3'
IL-10	*Yee et. al. 2005*[194]	5'-ATTTGAATTCCCTGGGTGAGAAG-3'	5'-CACAGGGGAGAAATCGATGACA-3'
KC / CXCL-1	*Jentho et. al. 2017*[195]	5´-ACTGCACCCAAACCGAAGTC-3´	5´-TGGGGACACCTTTTAGCATCTT-3´
LIX / CXCL-5/6	*In-house*	5'-CTCGCCATTCATGCGGAT-3'	5'-AGCTTTCTTTTTGTCACTGCCC-3'
Col3A1	*Chalmers et. al. 2008*[196]	5'-TGGCACAGCAGTCCAACGTA-3'	5'-TGACATGGTTCTGGCTTCCA-3'
Col1A1	*Marek et. al. 2017*[197]	5'-TCACCTACAGCACCCTTGTGG-3'	5'-CCCAAGTTCCGGTGTGACTC-3'
EF1A1	*Prokopec et. al. 2013*[198]	5'-GATGTTAGACGAGGCAATGTTG-3'	5'-CAATCCAGAACAGGAGCGTAG-3'
Polr2A	*Brattelid et. al. 2010*[199]	5'- CTCCTTTGAGGAAACGGTGGAT-3'	5'-GACTCCCTTCATCGGGTCACT-3'
Tuba1A	*Sanchez-Alvarez et. al. 2013*[200]	5'-CCTGGAACCCACGGTCATC-3'	5'-TGTAGTGGCCACGAGCATAGTTAT-3'

Table 2.1: Primers used for conventional polymerase chain reaction and quantitative, real-time polymerase chain reaction experiments. Housekeeping genes were: EF1A1 (elongation factor 1-α, Polr2A (RNA Polymerase II Subunit A), and Tuba1A (Tubulin α-1A chain).

2.4.4. Primer specificity testing – conventional Polymerase Chain Reaction (PCR)

Primer specificity testing was undertaken using cDNA synthesised for only a "T" sample, e.g. SG001T, as well as a *no RTC* and *no RNA* negative controls for the sample using conventional PCR. This was performed using the GoTaq® G2 Master Mix (Promega, M7822). Volumes added to a microtube were as below.

Component	**Volume (µL)**	**Final Concentration**
GoTaq® G2 Green Master Mix	10	1X
Nuclease free water	7	N/A
Forward primer	1	0.8µM
Reverse primer	1	0.8µM
cDNA template	1	500ng
Final microtube volume	***20***	

All labelled tubes were vortexed and briefly centrifuged. A BioRad ThermalCycler was used for PCR synthesis with the following protocol:

1. 95°C for 2 min HotStart DNA polymerase activation
2. 95°C for 30s (denaturation)
3. 60°C for 30s (annealing)
4. 72°C for 35s (extension) [steps 2-4 repeated 34 times]
5. 72°C for 5 min (final extension)
6. 4°C for 5 min (cooling)

Samples were loaded onto a 1.2% agarose gel (agarose in TAE (Tris-Acetate-EDTA)) with 5µL of SYBR Safe DNA gel stain (Invitrogen, S33102).

The gel was placed into a separator (BioRad) with 1x TAE buffer. 20µL of each sample was loaded into a lane, as well as a DNA ladder for comparison (100bp DNA Ladder and dye, New England Biolabs, N3231S) in the first lane of the gel. PCR products were allowed to separate at 110 volts for 50-60 minutes. Results were visualised using a ChemiDoc™ Gel Imaging System (BioRad).

2.4.5. Quantitative PCR

Q-PCR was undertaken to using the GoTaq® qPCR MasterMix (Promega, A6002) and a 384-well plate. Each plate tested the cDNA of the wound samples, the tail sample, and the two negative controls for each sample. Master mixes (no. of wells +1 extra) were made per gene of interest and three reference housekeeping genes for the plate. These consisted of primers, the master mix, and nuclease free water in the volumes, per well, as below.

Component	**Volume (µL)**
GoTaq® Hot Start MasterMix	5
Forward primer	0.25
Reverse primer	0.25
Nuclease free water	2.5
Total	***8***
+ cDNA template	+ 2
Final volume in well	***10***

The plate was set up with 8µL of the target or reference gene master mix, and 2µL of the cDNA template in each well. Samples were run in triplicate. The plate was then sealed with film (ThermalSeal RT sealing film, Excel Scientific), spun in the plate spinner for 30 seconds, and kept on ice until reading using the LightCycler @480 System (Roche). The program used to read each plate was as below.

	Target [°C]	**Acquisition Mode**	**Hold [hh:mm:ss]**	**Ramp Rate [°C/s]**	**Acquisitions [per °C]**
Pre-Incubation	95	None	00:10:00	4.8	–
Amplification	95 60 (annealing) 72 (extension)	None None Single	00:00:15 00:00:30 00:00:30	4.8 2.5 2.5	–
Melting Curve	95 65 97	None None Continuous	00:00:05 00:01:00 -	4.8 2.5 -	- - 5-10
Cooling	40	None	00:00:30	2.0	-

Threshold cycle (C_T) values were extracted using the machine's Abs Quant/2nd Derivative Max function for all samples, and saved as a text file for later analysis.

Analysis of PCR

mRNA expression levels were calculated using the Comparative Method[201], which uses the CT values to evaluate the fold expression of each target gene. The fold expression is defined as $2^{-\Delta\Delta C}T$, where:

$-\Delta\Delta CT = [(C_T$ Gene of interest A – C_T endogenous control gene A) - (C_T Gene of interest B – C_T endogenous control gene B)]

Where: A =graft, B = internal control.

2.5. Protein Methods

2.5.1. Protein Extraction and purification of tissue lysates: TriReagent Method

Protein was precipitated by adding 1500µl of 2-propanol (Sigma-Aldrich, Merck) per 1000µl of TR to the pink protein phase samples and gently mixed prior to letting stand in room temperature for 10-15 minutes. These were then centrifuged at 12,000 *x* g for 10 minutes at 2-8°C to precipitate a protein pellet at the bottom of the Eppendorf tubes. Supernatants were discarded prior to washing.

The pellets were washed by adding 0.3M guanidine hydrochloride/95% EtOH solution (guanidine hydrochloride, MW = 95.53 gmol^{-1}, Sigma Aldrich) (2000µL per 1000µL of TR used) to the tube, allowing to stand for 15-20 minutes, and centrifuging at 7,500 *x* g for 5 minutes at 2-8°C. Washing with the guanidine hydrochloride was repeated a further two times for a total of three washes.

Following this, 2000µl of 100% EtOH was added to the pellets, and the samples allowed to stand for 15-20 minutes at room temperature prior to centrifuging at 7,500 *x* g for 5 minutes at 2-8°C.

The supernatant following this final wash was discarded, leaving the pellets to air-dry until the EtOH evaporated. Excess EtOH was carefully removed with a KimWipe (Kimberly-Clark). Once dry, the pellets were allowed to dissolve in 300µL of RIPA buffer with added Phenylmethylsulfonyl fluoride (PMSF) and protease inhibitor. To facilitate dissolution, the samples were pipette mixed carefully.

The samples were spun down a final time at 10,000 *x* g for 10 minutes at 2-8°C. Protein samples were stored at -80°C until use.

2.5.2. Protein Extraction and purification of tissue lysates: snap freezing method

Snap-frozen tissues were kept on dry ice prior to processing to allow for ease of homogenisation and maximise breakdown by the blade. The homogeniser blade was cleaned with MilliQ and EtOH (3 x 10 second pulses) prior to processing. 200µL of the RIPA buffer was then added to the Eppendorf tube and the homogeniser blade placed within the tube. Homogenisation was performed (3 x 10 second pulses). Samples were then centrifuged at 10,000 *x g* for 10 minutes at 2-8°C. The supernatant was transferred to a new tube, and samples kept at -80°C storage for later use.

2.5.3. Protein quantification assays

The Pierce™ bicinchoninic acid (BCA) Protein Assay Kit (ThermoFisher, #233227) was used to quantitate the amount of total protein isolated from each sample. Standards were prepared by serially diluting the stock BSA (2000µg/ml) in PBS, to final BSA concentrations of 2000, 1500, 1000, 750, 500, 250 and 125µg/ml. The samples were prepared for triplicate in a 1:5 dilution with PBS.

10µL of both the samples and the standards were pipetted into a 96-well plate, as well as a blank of PBS. The working reagent was made as per the manufacturer's instructions by mixing Reagent A (buffer) with Reagent B (copper sulfate) in 50:1. Two hundred microlitres of the working reagent was then added to the wells with the samples, standards and blank, and mixed with pipetting. The plate was then mixed further on a shaker for 1 minute and incubated at 37°C for 1 hour. This was then allowed to cool for 10 minutes. The plate was read using a reader at 595nm (FLUOStar Omega Microplate Reader, BMG Labtech) and the absorbance values recorded.

To calculate the total protein of samples, the blank-corrected absorbances of the standards were plotted against their known BSA concentrations, and the gradient the slope calculated using Microsoft Excel. This resulted in a formula as calculated by the standard curve that enabled calculation of the final protein concentration of the samples using the mean of their absorbances as read off the plate.

2.5.4. Elimination of spurious absorbance readings: Radioimmunoprecipitation Assay Cell Lysis (RIPA) buffer optimisation

The RIPA buffer used in our lab was previously 50mM HEPES pH 7.4, 150mM NaCl, 10% Glycerol, 1.5mM $MgCl_2$, 1mM EGTA, 1Mm NaOv, 1% Triton X-100, 1% Sodium deoxycholate, 0.1% SDS, and 100mM NaF. Protease inhibitors (cOmplete™, Mini, EDTA-free Protease Inhibitor Cocktail; Merck/Roche; 1 tablet for 10mL of buffer) were added to the buffer prior to use. Additives were systematically eliminated and their absorbances read against the standard curve produced by the BCA protein assay. The final buffer used in experiments to facilitate protein pellet dissolution was 10mM Tris-HCl pH 7.3, 150mM NaCl, 0.1% SDS, 1% Triton X-100, 1% Sodium deoxycholate, 1mM EGTA and 1.5mM $MgCl_2$.

2.5.5. Enzyme-linked Immunosorbent Assays (ELISA)

IL-6 protein was evaluated using the BD OptEIA™ Set Mouse IL-6 Kit (BD Biosciences, 555240). A 96-well ELISA plate (NUNC-96, ThermoFisher) was coated with the capture antibody from the kit diluted in coating buffer (100µL per well, 1:250 dilution) (100mL of coating buffer: 100mL of MilliQ, 0.713g of $NaHCO_3$, 0.159g Na_2CO_3; pH altered to 9.5 with 10M of NaOH). The plate was sealed with parafilm and incubated in 4°C overnight.

The following day, multiple diluents were prepared prior to removing the incubating plate out of the fridge as follows:

- Sample diluent – 0.1% BSA in Dulbecco's Modified Eagle Medium (DMEM)
    - 8 standards require 500µL of sample diluent each ∴4000µL required for standards
    - *n* x 950µL of sample diluent, where *n* = no. of samples
- Assay diluent – PBS with 10% FBS
    - Needed approximately 20mL/plate for blocking the plate at an earlier step and 10mL/plate to make the working detector solution at a later step
- Wash buffer – PBS with 0.05% of Tween-20

Once these were made, the plate was taken out of incubation and washed with wash buffer (thrice, 200µL/well using a multi-channel pipette unless otherwise stated), and then blocked with assay diluent at room temperature for 1 hour.

The standards and samples were prepared whilst this occurred. Preparation of the standards were as per the manufacturer's instructions. Samples were prepared using a 40µg of protein per sample. An undiluted, 1:10 and 1:50 dilutions were prepared.

Following blocking, the plates were washed, and 100µL of the samples and standards were added to the plate. The plate was sealed and incubated for 2 hours at room temperature. Post incubation, the plate was washed five times.

100µL/well of working detector was added to the plate (20µL of detection antibody to 10mL of assay diluent for a 1:500 dilution, with 80µL of enzyme reagent solution added for 1:250 dilution), sealed, and incubated for an hour at room temperature.

Post incubation, the plate was washed 7 times. 100µL/well of substrate solution was added to the plate (TMB Microwell peroxidase substrate system, KPL Product/Australian Biosearch, 51200-00-53) and incubated under aluminium foil for darkness in room temperature. The plate was monitored for colour saturation in the wells.

Once the colour saturation was adequate (the solution in the wells turned to blue), 50µL of stop solution (1M H_3PO_4) was added to each well (turning the blue into yellow). The plate was read at 450nm.

2.5.6. Antibody Arrays

Protein amounts for various targets was assessed using Antibody Arrays (Mouse Neuro Antibody Array; Membrane, 23 Targets; AbCam, ab211069). Targets evaluated were: Fas Ligand, Fractalkine, GCSF, IFN-γ, IGF-1, IL-10, IL-1α, IL-1β, IL-4, IL-6, KC/CXCL-1, LIX/CXCL-5/6, MCP-1, M-CSF, MIP-1α, MMP-2, MMP-3, RAGE, TARC, SDF-1α, TGF-β, TNF-α, VEGF-A.

Protein arrays are analogous to ELISA, but use a membrane as a substrate rather than a plate, with the capture antibodies pre-manufactured on the membranes.

Protein lysates were thawed on ice with the blocking buffer that came with the kit. The 8-well plate and membranes were brought to room temperature. Membranes were only handled with forceps in one corner that was indicated with the "-" sign to signify the top-left corner of the membrane. Once thawed, 2ml of the blocking buffer was gently pipetted into each well with a membrane, and incubated on a rocker at room temperature for 30 minutes.

Lysates were used at a 50µg quantity. Volumes at this quantity were brought to 1µg/µl dilution using fresh RIPA buffer with added protein inhibitor. Diluted lysates were brought up to a volume of 1000µl with blocking buffer.

Once the membranes were blocked, the buffer was aspirated from each well, and the samples were pipetted into each well and incubated in a 4°C cool room overnight on a rocker.

The following day, 20x Wash Buffer I and 20x Wash Buffer II were diluted to 1X with MilliQ, and the Biotinylated Antibody Cocktail were prepared by adding 2ml of blocking buffer to each vial. The plate and rocker were then taken out of the cool room and samples aspirated from the wells. Two millilitres of 1x Wash Buffer I was pipetted into each well and placed on the rocker for 5 minutes three times for washing. Washing then followed with 2ml of 1x Wash Buffer II twice. After completing the washes, 1ml of the Biotinylated Antibody Cocktail was pipetted into each well, and left to incubated for two hours at room temperature on a rocker.

The 1000x HRP-Streptavidin was diluted down to 1x with blocking buffer. Following incubation with the antibody cocktail, the membranes were washed again as per previous, 2ml of the 1x HRP-Streptavidin pipetted into each well, and incubated for two hours at room temperature on a rocker.

Membranes were washed again as per previous following incubation with the HRP-Streptavidin. During the last wash, equal amounts of Detection Buffer C and D from the kit were placed in to a fresh tube. Once washed, the membranes were carefully removed from the wells and placed onto a plastic sheet provided in the kit. Five hundred microlitres of the detection buffer mixture was pipetted onto each membrane and incubated at room temperature for two minutes. Following this, another plastic sheet was carefully rolled onto the first sheet so that the membranes (4 membranes to a plastic sheet) were sandwiched in-between two plastic sheets. This was then read using a Chemidoc machine (BioRad).

2.6. Data analysis

2.6.1. Histological image analysis

Three fields of view from each section stained with Masson's Trichrome staining (left wound edge, wound bed, right wound edge) were imaged with a 20x objective. Image analysis was performed using Image J software (National Institutes of Health) using the colour threshold method. The threshold value was kept constant across all sections.

2.6.2. Protein Array Analysis

Membranes were analysed using the Protein Array Analyser plug-in available through Image J.

2.6.3. Wound contraction analysis

The macroscopic images taken for the mice whose endpoints were at D21 were analysed for wound contraction analysis. Images taken at the day of surgery (D0) and at every wound change (D5, D10 and D15) were used. Wound surface area (mm^2) was analysed using the Measurement/Analysis tool in ImageJ, using a ruler for scale within the analysed image. The mean of these measurements for both arms, and in each condition in Arm 2 (i.e. ungrafted vs. grafted wound bed), was used for statistical analysis.

2.6.4. Statistical analysis

Data collation and statistical analysis was performed using GraphPad Prism (Prism 8 for Windows, GraphPad Software LLC, version 8.3.1). Statistical analyses were performed using (paired) T-tests; if there was a comparison of more than two groups, ANOVA was used instead.

CHAPTER 3: RESULTS

Establishing a mouse model for studying changes in wound microenvironment when spontaneously repaired

3. Results: Establishing a mouse model for studying changes in wound microenvironment when spontaneously repaired

3.1. Introduction

In order to investigate how an autologous and synthetic graft modulates the normal trajectory of repairing a full-thickness wound, the stages of wound repair must first be defined in our mouse model. SKH-1 Hairless mice are used widely for dermatological research, particularly with chemically-induced wounds [67, 68]. Here we investigated whether we can use SKH-1 mice as a model to emulate the epithelialisation that leads to wound repair as seen in humans, rather than repair by contraction. Two full-thickness wounds were created on the dorsal side of each mouse. Mice were humanely sacrificed on D1, D2, D5, D8, D11, D14 and D21. Here, we utilised histological, RNA and protein analysis of well-known wound healing markers to characterise full-thickness excisional wound repair in SKH-1 mice.

3.1.1. Macroscopic changes of the wound over 21 days

The total body surface area (TBSA)% of the two wounds, sized at 15 mm in diameter, was measured as less than 5% [202, 203] (see below for the formula), even for mice that were at the minimum weight of 21 grams. This was below the maximum TBSA recommended by our institution's guidelines when introducing full-thickness wounds in animal models.

$$\mathbf{TBSA} = \boldsymbol{k} \times \mathbf{W}^{(2/3)}$$

Where: TBSA = area in cm^2, k is Meeh's constant (k = 9.82 or 9.66) [202, 203] and W = weight in grams.

On the day of surgery (D0), the wound edges were encircled by the silicon rings remained visible, and the wound bed was moist. Minimal changes to the appearance of the wound edges and wound bed were appreciated at the day 5 (D5) dressing change (see Figure 3.1a). The wound bed remained moist. At the day 10 (D10) dressing change, wound contraction was more evident macroscopically, as well as changes to the appearance of the wound bed such as a cloudy, matte-like appearance around the periphery of the wound. This continued to develop through to the day 15 (D15) dressing change, where the matte-like appearance extended the width of the wound despite remaining patchy in most cases. This culminated in an epithelialized wound at the day 21 (D21) endpoint. The epithelialized wound visualised at D21 was of a slightly lighter shade compared to the native skin surrounding the wound, and

was also opaquer. The dressings at D10 and D15 were slightly adhered to the wound bed, whereas the dressing was easy to remove due to the moist wound bed at D5.

Wound measurements demonstrated that the wound surface area (SA) at D0 was approximately 150 mm^2, with a steady decline to less than half the size of the original wound at the D21 endpoint (see Figure 3.1b). The largest incremental decrease in wound size was between D10 and D15, and this is also depicted in the macroscopic observations of the wound. The size of the wound remained relatively stable between D15 and D21.

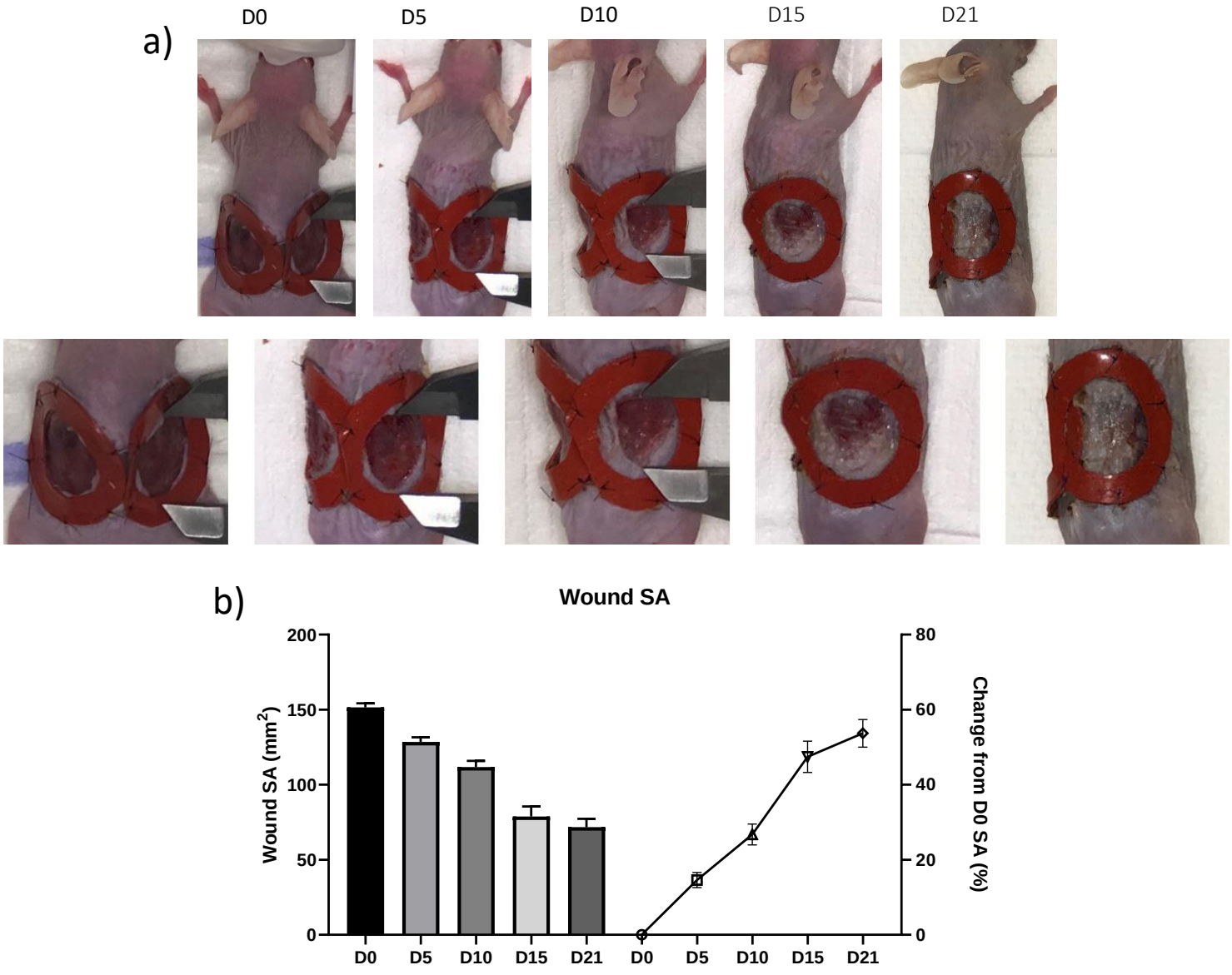

Figure 3.1: Wound contraction in a murine full-thickness wound over 21 days. (a)*:* Images taken with a camera phone on a tripod at a fixed length and zoom. Below is a zoomed-in picture of the wounds. **(b):** Wound (SA) changes measured using Image J. Left Y-axis indicates wound size and the right Y-axis indicates the change from the original measured wound size at D0. *N* = 6.

3.1.2. Histological evaluation of spontaneous wound repair using haematoxylin and eosin staining

The dermis in SKH-1 mice skin consists of an ECM that is stained densely pink with hair follicles at various stages of arrest. The panniculus carnosus lies below the dermis, with a thin connective tissue-like structure sitting below this. No hypodermis is evident. The epidermis, the outermost layer of the skin, undulates throughout its course. It is a few layers thicker in the dorsal skin (skin removed from the wound bed excised on the day of surgery, "D0") than the tail (samples taken at the tail on the day of the cull, "tail") (Figure 3.2a).

Between days 1 to 5, the wound bed consisted mainly of disorganised inflammatory cells with no discernible difference between epidermal and dermal layers or granulation tissue. Under high magnification, these cells had multi-lobar nuclei (data not shown). A thin, acellular, wound fluid sat atop of the granulation tissue above panniculus carnosus if present in the section. Clusters of nucleated cells were evident in the wound bed at the wound edge and at the wound bed at days 1 and 2 (see Figure 3.2a). The number of cells, possibly including endothelial cells and/or fibroblasts, at the wound bed increased between days 2 and 5, and again between days 5 and 8. Although, their identity and prevalence are yet to be determined.

At day 5, a different type of cell, possibly contractile fibroblasts, that is orientated perpendicularly to the others became evident at the wound edge, and is most evident at day 8, where they also appeared at the wound bed (see Figure 3.2b). Neo-epidermis was visible at the wound edges from day 8; and by day 11, there was a clear distinction between the two layers of the epidermis and dermis. The epidermis hyperproliferated at days 11 and 14, then eventually thinned out on the final endpoint at day 21. The cells of the dermis were stained densely purple. Hair follicles had regenerated by this point at the wound edge but not in the middle of the wound bed.

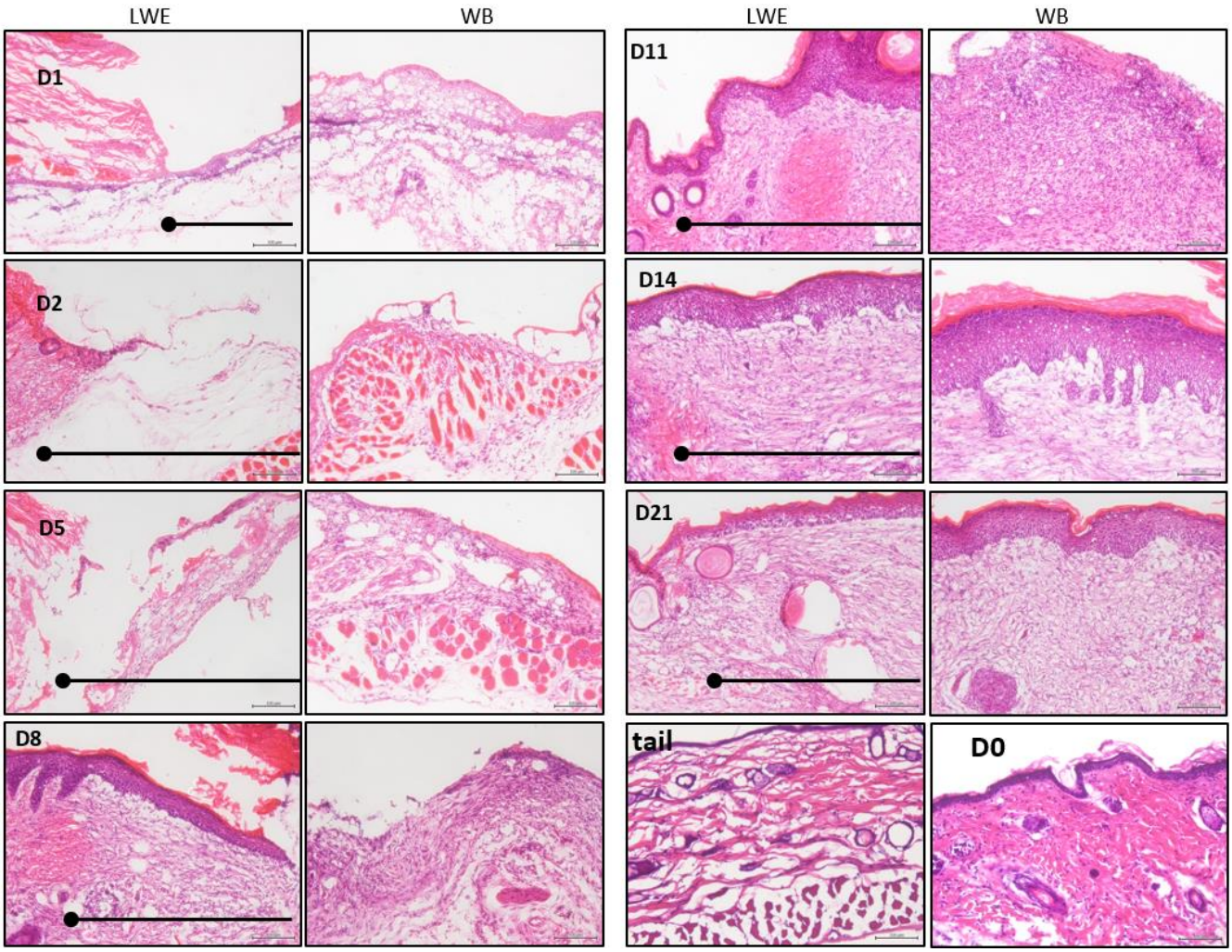

F**igure 3.2: (a) Haematoxylin and eosin staining of a murine full-thickness wound at Days 1, 2, 5, 8, 11, 14 and 21 post-operation.** Line with left-sided dot indicates on LWE images indicates wound edge (dot) and wound bed (line). Bottom right corner images are tail (dorsal taken at day of cull) and D0 images (skin taken on day of operation from excisional wound). Scale bar reads 100µm for all images. *LWE: Left wound edge, WB: wound bed.*

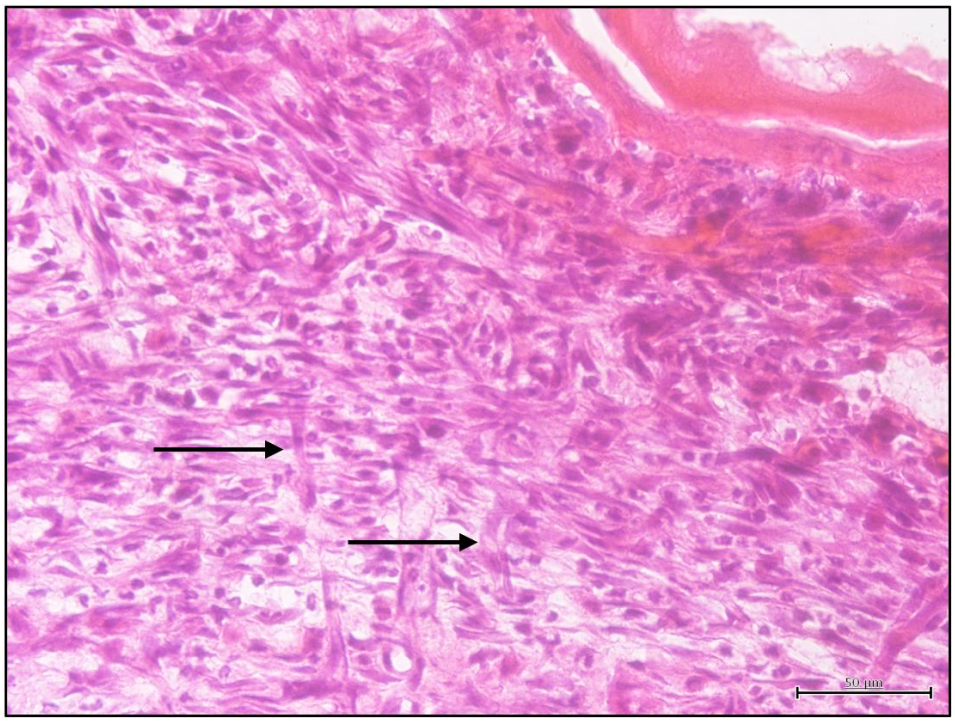

Figure 3.2: (b) Haematoxylin and eosin staining of a full-thickness wound at the right wound edge on D5 post-operation. Arrows indicate perpendicular oriented cells to most other cells within the granulation tissue. Scale bar reads 50µm.

3.1.3. Collagen deposition during spontaneous wound repair

Masson's Trichrome staining of wounds at D1, D2, D5, D8, D11, D14 and D21 post-surgery was employed to quantify collagen deposition (Figure 3.3a). Native dermis in the SKH-1 mouse is densely stained with a dark blue marking collagen. Hair follicles, epidermis and the panniculus carnosus were stained red or pink.

At the earlier endpoints (days 1-5), very little collagen was evident at the wound bed, and some collagen was present at the edges. If a panniculus carnosus was present in the section, collagen was evident both above and below the muscle (see Figure 3.3a). Only collagen above the panniculus carnosus (i.e. dermis) was quantified.

By D8, collagen fibres were denser at the edges as well as at the bottom of the wound bed. Collagen fibres were mostly oriented in a parallel-like fashion at the base of the wound bed. Wound fluid, stained in red, was present more superiorly at the wound bed. The blue collagen staining density increased between D11 and D21. By D21, the darkest blue (dense) staining was most evident at the bottom of the wound bed, with a basket-weave like structure

representing mature collagen. Collagen underneath neo-epidermis had a parallel-like structure representing new collagen as well as at the edges of the wound.

The total area of the wound stained for collagen was quantified for both wound edges and the middle of the wound bed. This demonstrated that the amount of collagen deposited at the wound at D1 post-operation was significantly less than the collagen deposited at D11 (p = 0.02), D14 (p = 0.04) and D21 (p < 0.01). The same was true for D2 to D11 (p < 0.01), D2 to D14 (p = 0.01), D2 to D21 (p < 0.01), D5 to D11 (p = 0.02), D5 to D14 (p = 0.02), D5 to D21 (p < 0.01), for D8 to D14 (p = 0.04) and D8 to 21 (p = 0.02) (see Figure 3.3b). One-way ANOVA was employed for the comparison of the groups over the seven time-points, yielding a p = 0.004.

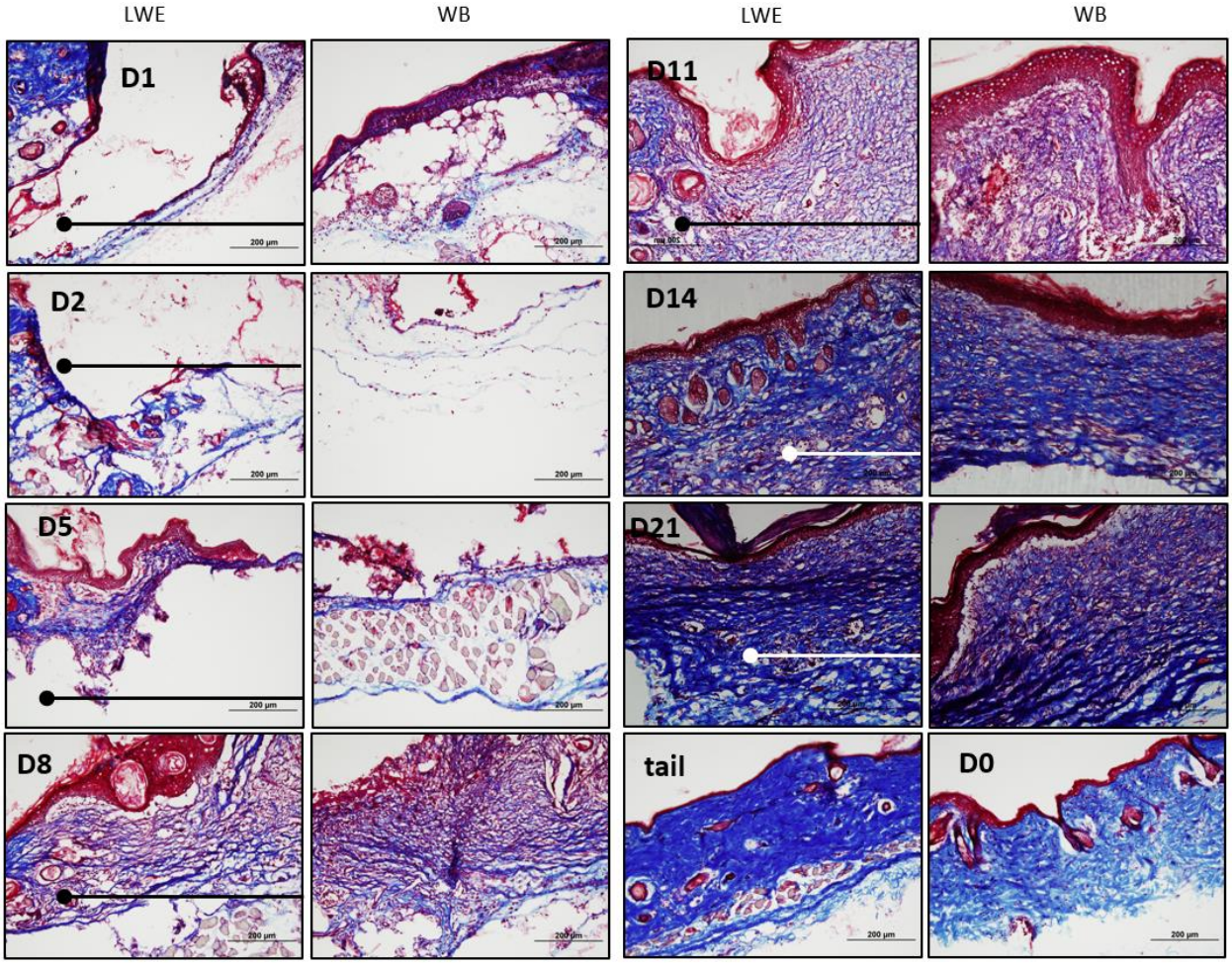

Figure 3.3: (a) Collagen deposition using Masson's Trichrome staining of a murine full-thickness wound at Days 1, 2, 5, 8, 11, 14 and 21 post-operation. Keratin and cytoplasm is stained pink/red, and collagen is stained blue. The darkness of blue denotes that the collagen stained is older. Line with left-sided dot indicates on LWE images indicates wound edge (dot) and wound bed (line). Bottom right images are tail and D0 images. Scale bar reads 200µm for all images. *LWE: Left wound edge, WB: wound bed.*

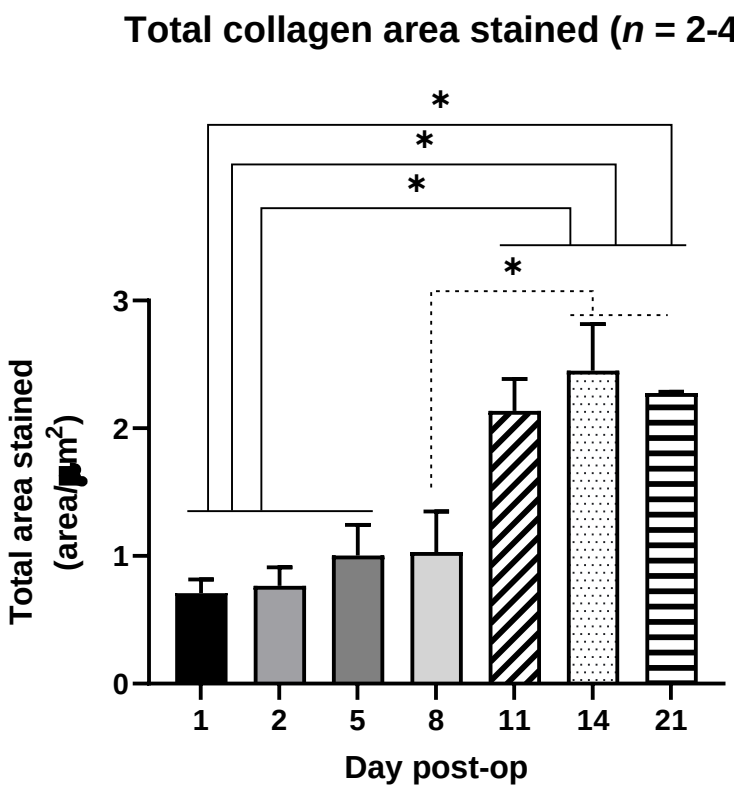

Figure 3.3: (b) Quantification of the total collagen area stained with Masson's Trichrome (area per µm^2) with Masson's Trichrome at Days 1, 2, 5, 8, 11, 14 and 21 post-operation. Images were taken of sections at both wound edges and the middle of the wound bed with BX100 camera and quantified using ImageJ. Statistical analysis was performed using ANOVA. The amount of collagen deposited at the wound at D1 was significant less than the collagen deposited at D11, D14 and 21 (p = 0.03, p = 0.008, p = 0.02 respectively). The collagen deposited at D2 was significantly less than the collagen deposited compared to D11 (p = 0.02), D14 (p = 0.004) and D21 (p = 0.01). The total area of collagen stained at D5 was less than the area stained at D11 (p = 0.049), D14 (p = 0.009) and D21 (p = 0.02). The collagen deposited at D8 was less than the area at D14 (p = 0.02) and D21 (p = 0.04). The difference in collagen deposition over the 7 time points was significant (p = 0.004). N = 2 for D1, n = 4 for D5, n = 3 for all other days post-operation.

3.1.4. Inflammatory and proliferative growth factor profiles at an RNA level during spontaneous wound repair

Skin from the tail and wound beds were harvested on D1 and days 2, 5, 8, 11, 14 and 21. RNA samples were purified and analysed for the expression of the inflammatory cytokines/growth factors of interest TNF-α, IL-1β, IL-6 and the IL-8 homologues, CXCL-1 and CXCL-5/6, using Q-PCR. These were calculated as expression-fold change and normalised to the tail skin of that same mouse, with a fold change of 1 expressing "no change". At all

timepoints, all inflammatory cytokines/growth factors of interest expressed a fold change greater than 1 (see Figure 3.4, dotted lines). The expression fold changes for TNF-α, IL-1β and IL-6 were similar between D1 and D2. All three target genes peaked at D5 and again at later timepoints (D21 and D14, see Figure 3.4, a-c). The IL-8 homologues, CXCL-1 and CXCL-5/6, both peaked at D5 and at D21 (see Figure 3.4, d and e).

The expression of proliferative markers TGF-β1, IL-10, PDGF-BB, VEGF-A, Collagen 3 (Col3) and Collagen 1 (Col1) in the wounds were also investigated. TGF-β1 and VEGF-A peaked at D5. IL-10 peaked earlier at D2, and fold expression changes of PDGF-BB were similar between D2 and D5. Col1 increased significantly between D2 and D5, with an overall peak at D21. Fold expression changes for Col3 were similar between D11-21, following a rise between D1-D5 (see Figure 3.5, a-f).

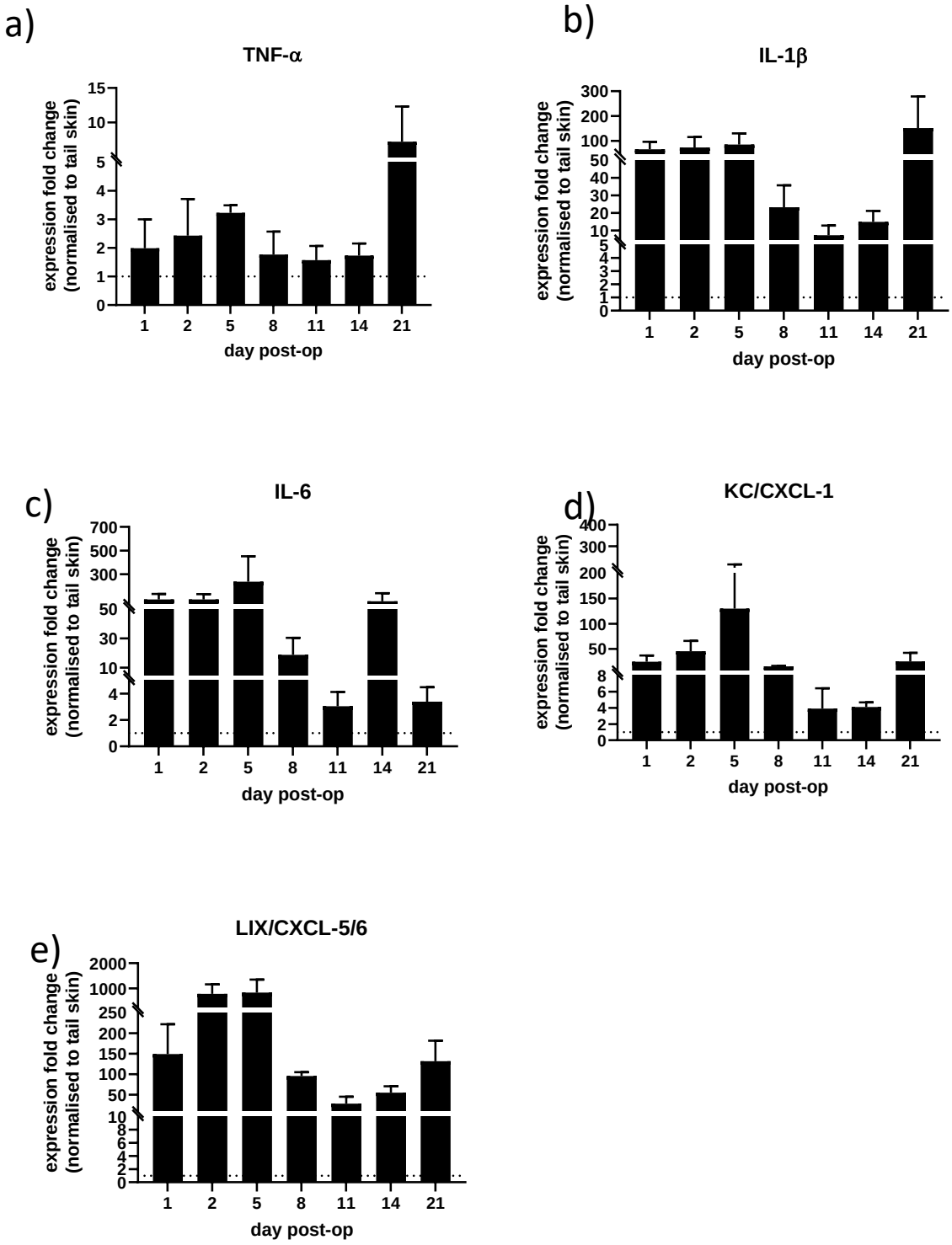

Figure 3.4: (a-e) Quantitative RT-PCR results of inflammatory cytokines targets. Data was analysed as expression fold changes of the targets against the average of the C_t values of three housekeeping genes (Polr2A, EF1A1, Tuba1A), and normalised against the C_t values of the same genes of the tail skin. Statistical analysis was performed using one-way ANOVA, which did not yield any significant results. Dotted line indicates expression fold change = 1 (i.e., no expression fold change below this). *N* = 3.

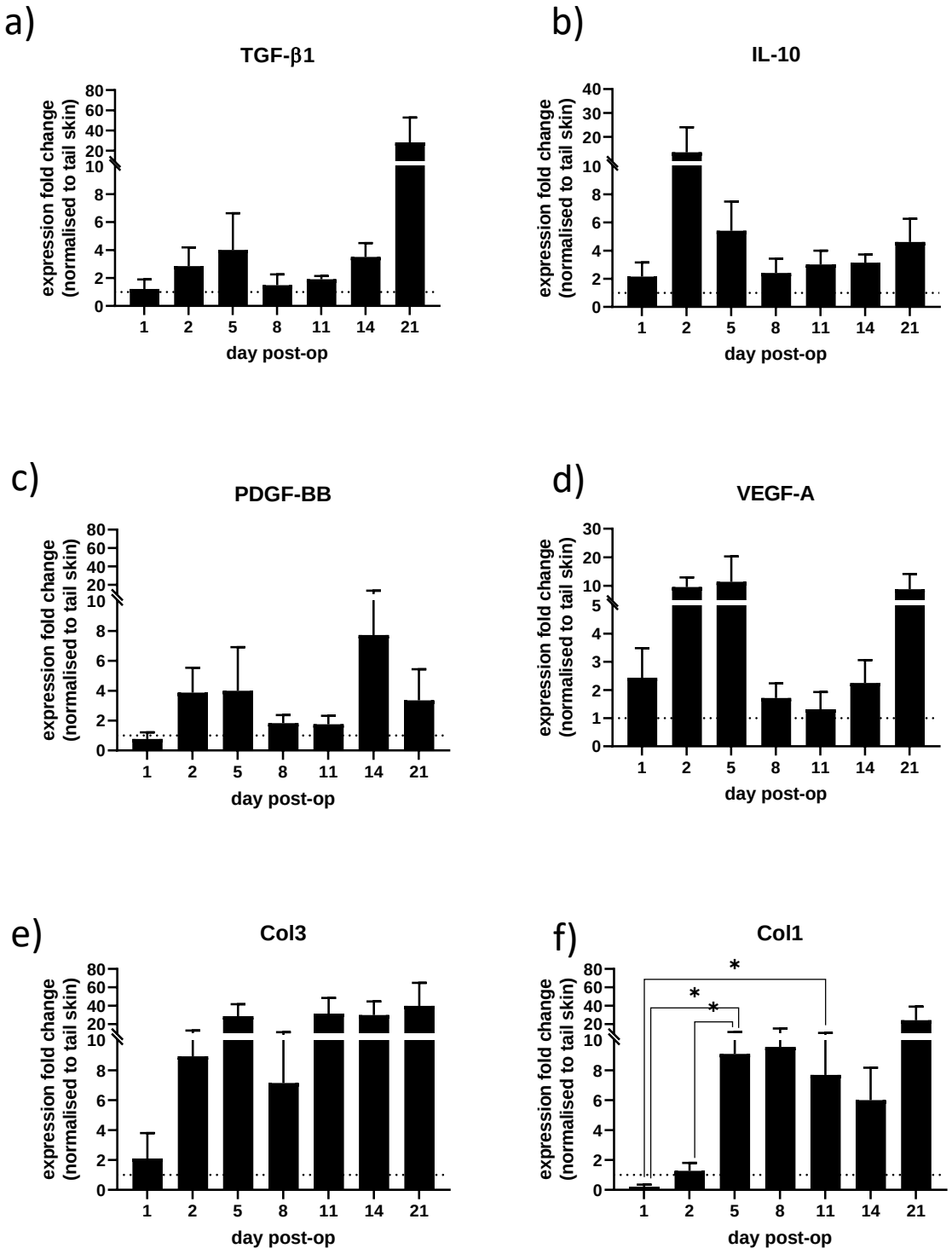

Figure 3.5: (a-f) Quantitative RT-PCR results of proliferation cytokine/growth factor targets. Data was analysed as expression fold changes of the targets against the average of the C_t values of three housekeeping genes (Polr2A, EF1A1, Tuba1A), and normalised against the C_t values of the same genes of the tail skin. Statistical analysis was performed for all genes of interest using one-way ANOVA. Expression fold changes of Col1 were significantly higher at D5 and D11 compared to D1 (p = 0.02 and p = 0.04, respectively), and higher at D5 compared to D2 (p = 0.03). Dotted line indicates expression fold change = 1 (i.e., no expression fold change below this). *N = 3.*

3.1.5. IL-6 levels during spontaneous wound repair

IL-6 and CXCL-5/6 were the most abundant inflammatory growth factors during spontaneous wound repair at an RNA level. IL-6 levels were analysed at protein levels in the wound bed and tail. There was a difference between the levels of IL-6 expressed at the wound and at the tail. The latter was considered to be a more systemic expression of the protein. Systemically, IL-6 expression reached its maximum at day 1, with its lowest at day 11. There was an overall downwards trend for the IL-6 expression systemically (see Figure 3.6). At the wound, IL-6 peaked slightly at day 5, but reached its nadir at day 21. Its lowest was measured at day 1. There was a statistically significant difference in the IL-6 expressed between the wound and the tail (p = 0.04) at D5 post-operation.

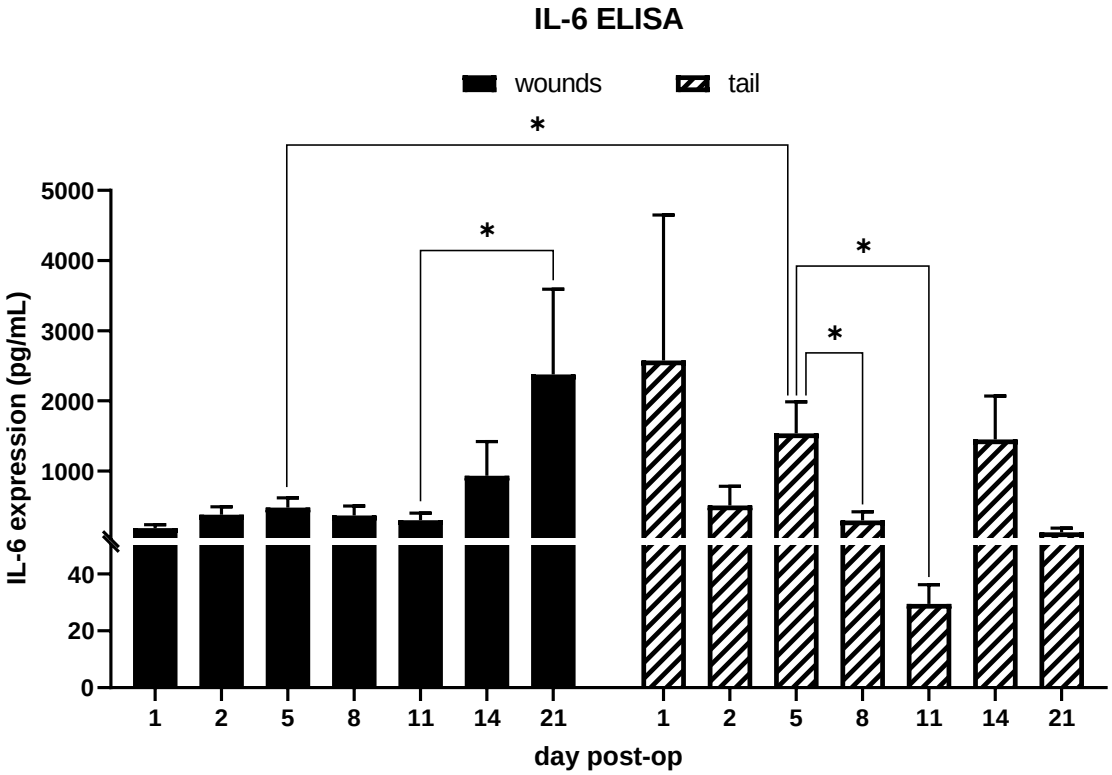

Figure 3.6: Protein expression of IL-6 at the wound beds and at the tail in the full-thickness wound mouse model using ELISA. The protein expression was averaged between the left and right wounds. There were significant differences in the levels of IL-6 expressed at both wound beds at D5 compared to the tail at D5. The IL-6 expressed at the wounds at D21 was also significantly higher compared to the wounds at D11. In addition, IL-6 expressed at D8 and D11 at the tail were significantly lower than on D5 at the tail. (* $p < 0.05$). *N = 3.*

3.1.6. Discussion

The behaviour and trends of various target inflammatory and proliferative genes have previously been investigated in mouse models of wound healing[69, 192]. However, the temporal profile of key inflammatory and proliferative growth factors and cytokines has yet to be characterised in the SKH-1 mouse strain. This strain is an adequate murine model of full-thickness wound repair, as it is immunocompetent. It also has fewer hair follicles after shedding its hair at approximately three weeks of age, which would thus hinder the brisk wound repair that would occur due to the presence of epidermal stem cell niche within hair follicles.

In order to facilitate the wound repair by epithelialisation as seen in humans, silicon rings were attached to the periphery of the wounds given to the mice. Wound splints have previously been successful in various other studies investigating murine wound repair[204-206]. Following a similarly described protocol of wound splinting[190], the contraction as normally described[187] that repairs murine wounds was impeded using our model. The wound remained open by the D1, D2, D5 and even the D8 endpoints.

The splinting resulted in the successful epidermisation, similar to humans, that begins during the proliferative phase of wound repair. This was also reflected in our mouse model, with evidence of an epidermis beginning at D5 visible through haematoxylin and eosin staining (see Figure 3.2a). The deposition of collagen beginning during the proliferative phase of wound healing is also evident in the model. The behaviour of various cytokines and growth factors involved in wound repair also seem behave similarly to the temporal profile of the cytokines/growth factors seen in humans and pre-existing wound models.

Protocol Streamlining

Protein extraction

Throughout the process, protocols were streamlined and improved in order to maximise and maintain result integrity. One such alteration was the method by which protein was exacted from the tissues collected at the wound bed and the tail.

The primary method for collection of RNA and protein was the utilisation of TriReagent (TRIzol, TR), given this method would allow for the collection of both RNA and protein from the same tissue, and therefore reducing overall tissue requirement. However, it was clear early on in the execution of the murine full-thickness wound model that the protein pellet

extracted through the steps as outlined by the manufacturer's methods was difficult to dissolve in the 1% SDS solution recommended.

Various extra steps were included as per the manufacturer's instructions to facilitate improvement of pellet dissolution. These steps included the elimination of extracellular material that may render the pellet difficult to dissolve via centrifugation following initial tissue homogenisation (see Section 2.3.1), and incubation of the pellet sample suspended in buffer for 50°C. Despite the incorporation of these steps, the pellet remained difficult to dissolve into solution. Therefore, the total amount of protein yielded was less than expected (results not shown), even so far as producing amounts as little as 10µg in 200µL. This was deemed insufficient for performing an ELISA to examine the expression of a single growth factor or cytokine for that particular protein sample.

The size of the wound bed was increased from 0.8 cm diameter to a 1.5 cm diameter (data presented in Chapters 4 and 5) in order to increase the total protein yield, as there was lack of starting material present at the wound, particularly during the earlier stages of repair such as D1-5 where tissue collected from the wound bed could have been as little as 10 mg.

Poor protein yield through the TR method is a common issue[207], and as such, a different buffer was used to facilitate the improvement in pellet dissolution as recommended by various other studies[207, 208]. Kopec *et. al.* (2017) recommended an optimised standard lysis buffer (20mM EDTA, 140mM NaCl, 5% SDS, 100mM Tris pH 8.0, 50mM NaF, 1mM activated NaOv, protease inhibitors).

Our laboratory has previously used a similar buffer with extra additives for protein extraction through snap-freezing by liquid nitrogen, and so this buffer was used to facilitate the dissolution of the protein pellet extracted through TR. The radioimmunoprecipitation assay (RIPA) buffer contained 50mM HEPES pH 7.4, 150mM NaCl, 10% Glycerol, 1.5mM $MgCl_2$, 1mM EGTA, 1Mm NaOv, 1% Triton X-100, 1% sodium deoxycholate, 0.1% SDS, and 100mM NaF. Protease inhibitors were added to the buffer prior to use. The RIPA buffer did demonstrate a more efficacious dissolution of the protein pellet. However, it was also noted that when accounted for as the blank during the BCA Protein Assays for protein quantification (see Section 2.6.3), the RIPA buffer was providing an absorbance that negatively affected the absolute quantification of protein.

The systematic elimination of additives indicated that glycerol was responsible for producing the absorbance readings that were likely to have been affecting total protein quantification. Glycerol prevents protein aggregation and enhances the stability of proteins in an aqueous solution[209], however $MgCl_2$ has also been shown to improve protein extraction[210] as well as reduced contamination of final protein and less interaction with other proteins[211]. Finally, the buffer used in experiments to facilitate protein pellet dissolution was 10mM Tris-HCl pH 7.3, 150mM NaCl, 0.1% SDS, 1% Triton X-100, 1% Sodium deoxycholate, 1mM EGTA and 1.5mM $MgCl_2$.

RNA extraction

RNA was initially extracted using the TR method, with no requirement for further purification by use of columns or other method as per the manufacturer's instructions. However, the 260/280 absorbance value ratios ($A_{260/280}$) read via the Nanodrop Spectrophotometer for the RNA processed through this method were consistently 1.7-1.8, which is below the ratio considered for purity with RNA samples (2.0)[212]. The quantities as assessed using the Nanodrop Spectrophotometer were the values initially used for cDNA synthesis. However, it was noted that he C_T values of our housekeeping genes (Polr2A, EF1A1, Tuba1A) were inconsistent particularly for the RNA samples of mice culled for the full-thickness wound model. Other housekeeping genes (GAPDH, 18S) were trialled, with similar inconsistencies. Further, 18S as a gene is without introns, which would thus make the amplification of genomic DNA as a contaminant likely should the RNA product be impure.

Following this, various steps were taken to ensure the integrity of the RNA was well as the resultant RT-PCR data. The first was to improve the RNA extraction, increasing the purification steps involved. This required hybridisation of the TriReagent method and a column purification method. A similar protocol can be found on the Qiagen website[213]. This method ensures that any genomic DNA contamination is inhibited through DNAse digestion, as well as protecting the final RNA from degradation by the addition of RNAse inhibitor as a final step prior to storage.

The second step was deviating from the Nanodrop Spectrophotometer. It has previously been reported that the phenol component in TriReagent has an absorbance that can be read at 270 nm when the RNA quantity is low[214, 215]. The Nanodrop reads absorbances at both the 260 and 280 nm wavelengths. The spurious reading from the phenol may thus over-estimate the

quantity of RNA read via the Nanodrop. The resultant inaccurate measurement could determine whether or not the following PCR procedures are deemed successful, and if so, accurate. Correction has been suggested via a computational method[215] or by using 1-butanol to precipitate the RNA instead of ethanol during the early stages of extraction[214] to improve Nanodrop readings.

However, compared to spectrophotometric methods, fluorescent methods are more specific to nucleic acids and are less affected by other components present in samples such as phenol[216]. This leads to a more accurate determination of nucleic acid concentration. Thus, a fluorometer was utilised in quantification procedures when working with RNA (see Section 2.5.1). The RT-PCR results that used these readings successfully eliminated the inconsistencies between housekeeping genes, as well negating the need for extra corrective steps of RNA quantity.

CHAPTER 4: RESULTS

Investigating the molecular occurrences in autografted full-thickness wound bed

4. Results: Investigating the molecular changes in an autografted full-thickness wound bed

4.1. Introduction

Following the establishment of full-thickness wound repair, the differences in the wound repaired by a graft was characterised. In this section of the study, histological, RNA and protein analysis were applied to investigate how an autologous full-thickness skin graft modulates the repair of a full-thickness wound in our model compared to a wound allowed to heal without intervention. Based on data presented in Chapter 3, wounds were analysed D1, D5 and D21 following culls to represent the inflammation, proliferation, and remodelling phases of wound repair.

4.1.1. Macroscopic changes of an autologous-grafted wound over 21 days

As with the previous group, two wounds on the dorsum of the mice were applied. For this group, one wound was grafted with an autologous full-thickness skin graft (FTSG) with the other left to heal spontaneously. Similar to the full-thickness wound model described in the previous chapter, the full-thickness wound bed was moist prior to the application of the dressing and waking the animal from anaesthesia. Minimal macroscopic changes were appreciable at the D5 dressing change in this ungrafted wound, behaving similarly throughout dressing changes to the wounds of the full-thickness wound model.

The full-thickness wound had epithelialized, as we were able to separate it into its epidermal and dermal layers for tissue processing by soaking it in 1M NaCl for 1.25 hours (see Section 2.3). This was done in order to isolate the dermis from the epidermis, and to ensure that any changes the grafts and the wound were attributed to the dermis.

The FTSG sutured onto the other wound bed was of similar colour to the surrounding native skin at D0. At D5, the edges of the graft were pale as opposed to the hyperaemia evident at the middle of the graft (see Figure 4.1 b). Eschar surrounded the graft, delineating the original outline of the wound bed.

The colour of the graft was not homogeneous at the D10 dressing change. By D15, the graft looked to have a pale layer that had begun to lift at the wound edges. By the D21 endpoint, the top layer was able to be lifted off completely, revealing *de-novo* epidermis underneath. The *de novo* epidermis was pink and integrated to the original wound edges. All mice assigned

to complete the full 21 days of the experiment were deemed to have “taken” grafts with no signs of wound infection.

Macroscopically, the size of the grafted wound underwent minimal contraction, compared to the decrease in wound size of the ungrafted wound bed (see Figure 4.1f). There were significant differences in the wound sizes between the ungrafted wound and the wound with FTSG at the D15 and the D21 endpoint ($p < 0.0001$ and $p = 0.003$, respectively), with the ungrafted wound contracting to less than half its original size at D0 compared to D21.

a) D0

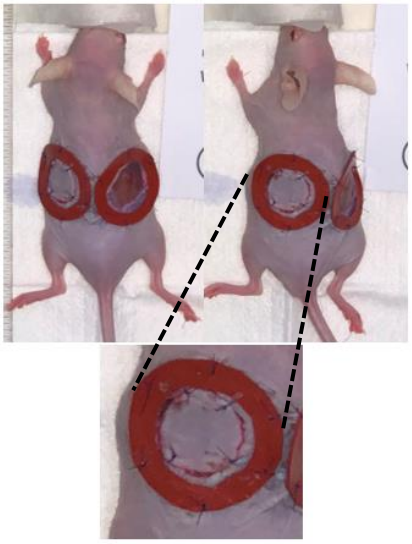

b) D5

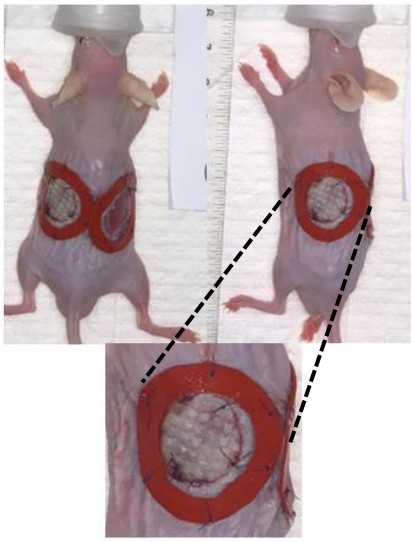

c) D10

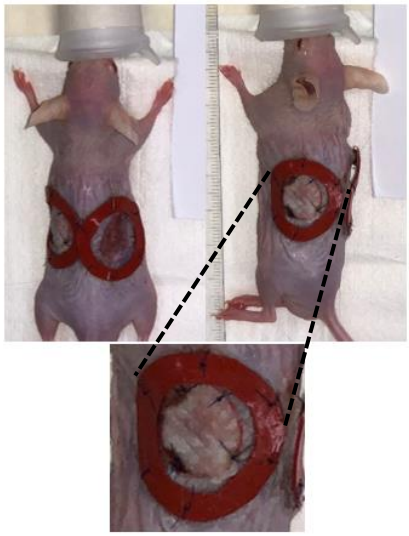

d) D15

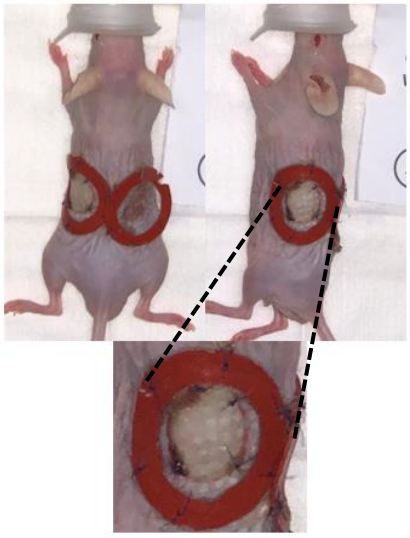

e) D21

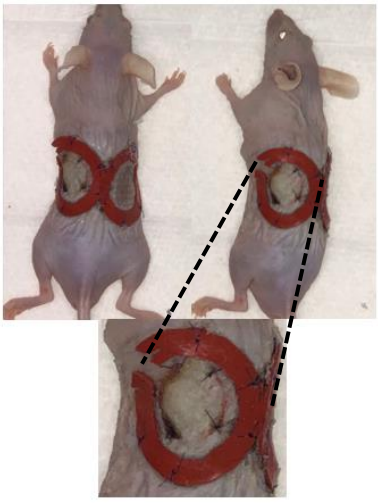

f)

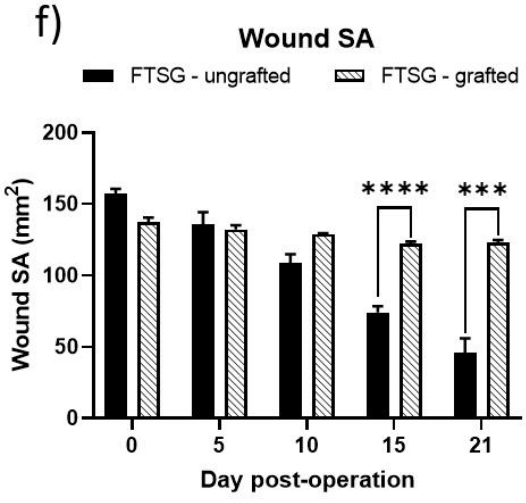

Figure 4.1: (a-e): Contraction in an murine full-thickness wound grafted with a FTSG over 21 days. Macroscopic images taken with a camera phone on a tripod at fixed length and zoom. A ruler for scale within the image (not shown) was used for image analysis**.** The wound bed, zoomed-in, is below the images of the mice. **(f):** Graph indicating the changes in the size of the wound surface area (SA) of the ungrafted (solid bars) and the grafted (shaded bars) wounds. The surface area of the grafted wound was significantly greater at D15 and D21 compared to the ungrafted wound (****$p < 0.0001$, *** $p < 0.001$). $N = 4$.

4.1.2. Histological evaluation of autologous-grafted wound repair using haematoxylin and eosin staining

Both the grafted and ungrafted sides of the mice were collected, fixed in 4% PFA, embedded and cryopreserved. The haematoxylin and eosin staining was performed in a similar fashion described in section 2.4.2.

Similar to the full-thickness spontaneous wound repair group, the ungrafted wound beds at D1 and D5 were populated with dense amounts of disorganised nucleated cells on a thin layer of granulation tissue. The same clusters of nucleated cells evident at both the edges and bed were present in the ungrafted controls at D1 and D5. The number of cells, again possibly endothelial cells and fibroblasts, increased between D1 and D5 (Figure 4.2a-c).

The edges of the graft and the native tissue surrounding the wound bed were still disparate at D1. Inflammatory cells with varying nuclear shapes, evident under high magnification (data not shown), were seen at the bottom of the wound edge at the side of the native skin. These were also seen at the bottom of the graft itself, below the panniculus carnosus. Unlike the full-thickness wound model, it was difficult to visualise the enucleated wound fluid evident on top of the granulation tissue in this group.

By D5, a bridge of purple-stained, nucleated cells (possibly immune cells) had formed between the graft at the wound edge, with the number of cells remaining similar below the graft between D1 and D5 (although this has not been quantified). The graft and native skin had united by D5. The architecture of the skin of the graft remained relatively undisturbed at D1 and D5.

By D21, there seemed to be fewer purple-stained cells that marked the cellular bridge between the graft and native skin. Underneath the graft was a layer of granulation tissue of similar appearance to that of the ungrafted control but with an increased number of nucleated cells stained purple (data not shown). Images of the epidermal layer of the graft taken at the middle of the wound bed show that a new stratum corneum forming underneath a layer of lifting epidermis (see Figure 4.2 d).

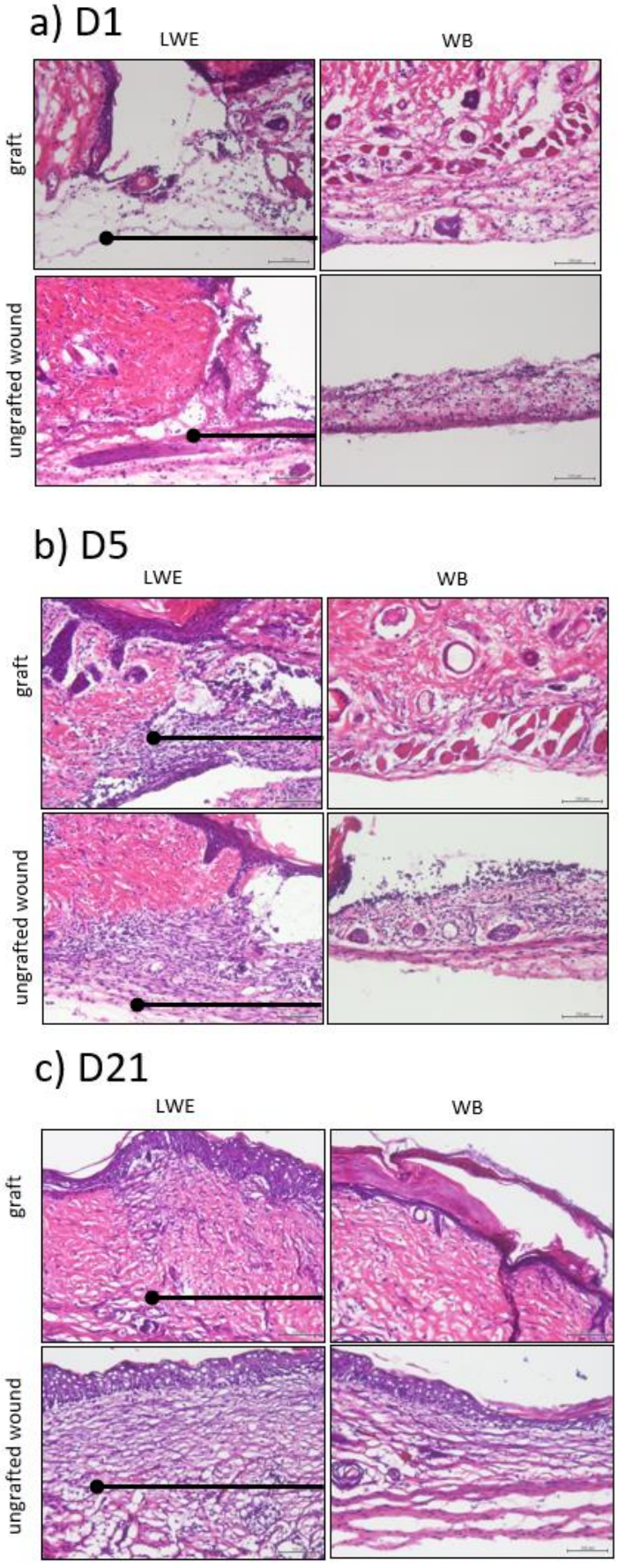
a) D1
LWE
WB
graft
ungrafted wound
b) D5
LWE
WB
graft
ungrafted wound
c) D21
LWE
WB
graft
ungrafted wound

d)

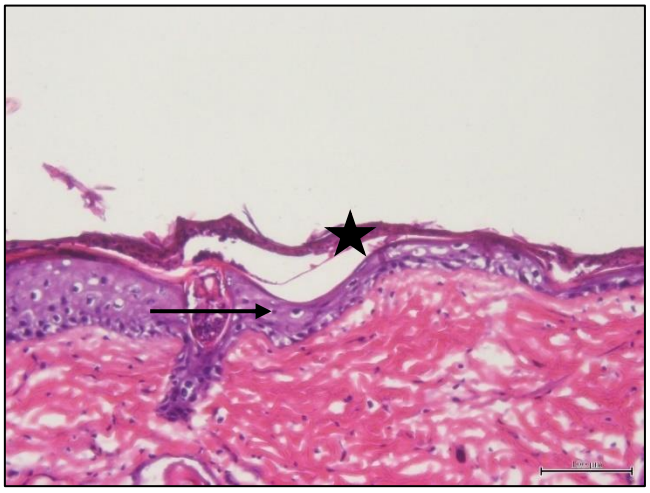

Figure 4.2: Haematoxylin and eosin staining of a murine full-thickness wound bed with FTSG and an ungrafted full-thickness wound at the inflammatory (a, D1), proliferative (b, D5) and remodelling (c, D21) timepoints. Line with left-sided dot indicates on LWE images indicates wound edge (dot) and wound bed (line). Scale bar reads 100µm for a-c. **(d) Haematoxylin and eosin staining of the epidermis at middle of the wound bed grafted with FTSG on D21.** Image demonstrates the lifting of the old epidermis (topmost layer, star) and the new epidermis forming below this (arrow head). Scale bar reads 50µm. *LWE: Left wound edge, WB: wound bed.*

4.1.3. Inflammatory and proliferative growth factor profiles during wound repair in an autologous-grafted wound at an RNA level

IL-6, CXCL-1, CXCL-5/6, VEGF-A, TGF-β1, Collagen III and Collagen I were selected from the range investigated in the previous chapter. This was due to their significant activity at the wound bed (and at the tail, as with IL-6), their recorded activity at all periods of wound healing in the literature, as well as their having further data with which to correlate histological analysis.

The fold expression of the inflammatory targets IL-6, CXCL-1, and CXCL-5/6 were all higher in the ungrafted wound beds compared to their grafted counterparts at during the inflammatory and proliferative timepoints (see Figure 4.3 a-c). CXCL-1 levels were significantly lower on D1 and D5 at the grafted wounds ($p = 0.033$ and $p = 0.0140$, respectively). CXCL-5/6 was significantly lower at the grafted wounds on D1 ($p < 0.05$). Levels of IL-6 were also lower at the grafted wounds at D1 and D5, though these differences were not statistically

significant. The levels of IL-6, CXCL-1 and CXCL-5/6 were higher in the grafted wounds on D21 compared to the ungrafted wounds, though it did not reach a significant level.

VEGF-A and TGF-β1 were lower at the wound beds grafted with an autologous full-thickness graft than the wound beds without a graft on D1 and D5. This difference was significantly lower for VEGF-A at D5 ($p = 0.03$), for TGF-β1 at D1 ($p = 0.04$) and for TGF-β1 at D5 ($p = 0.02$). Col3 expression was also significantly lower at the grafted wound beds, with on D1 ($p = 0.04$) and D5 ($p = 0.003$). Although also lower at the grafted wound at D21, this difference was not significant. Levels of Col1 were also significantly lower at the grafted wound bed on D5 ($p = 0.003$), with the highest expression of Col1 existing in the ungrafted wound bed at D5 prior to decreasing again on D21.

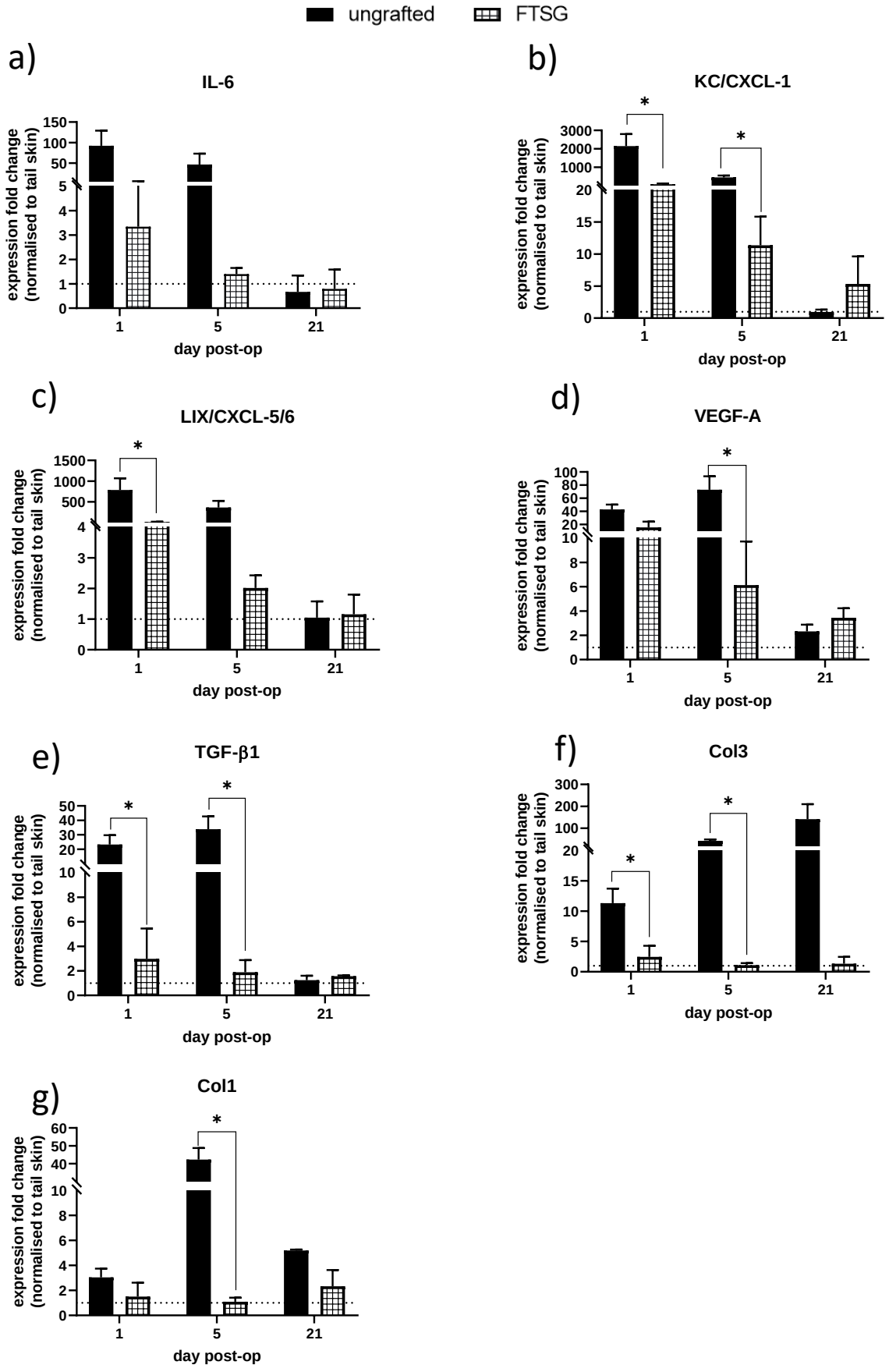
ungrafted
FTSG
a)
IL-6
b)
KC/CXCL-1
c)
LIX/CXCL-5/6
d)
VEGF-A
e)
TGF-β1
f)
Col3
g)
Col1
expression fold change (normalised to tail skin)
day post-op
1
5
21
*

Figure 4.3: (a-g) Quantitative RT-PCR results of inflammatory and proliferative cytokine/growth factor targets of ungrafted full-thickness wounds (solid bars) and wounds grafted with FTSG (checked bars). Data was analysed as expression fold changes of the targets against the average of the C_t values of three housekeeping genes (Polr2A, EF1A1, Tuba1A), and normalised against the C_t values of the same genes of the tail skin. **(a)** Expression fold changes of IL-6 were higher at the ungrafted wound beds at all timepoints, but not significantly so. **(b)** Expression fold changes of KC/CXCL-1 were significantly lower at the grafted wounds compared to the ungrafted wounds at D1 ($p = 0.033$) and D5 ($p = 0.014$). **(c)** Expression fold changes of LIX/CXCL-5/6 were significantly lower at the grafted wounds compared to the ungrafted wounds at D1 ($p < 0.05$). **(d)** Expression fold changes of VEGF-A were significantly lower at the grafted wounds compared to the ungrafted wounds at D5 ($p = 0.03$). **(e)** Expression fold changes of TGF-β1 were significantly lower at the grafted wounds compared to the ungrafted wounds at D1 ($p = 0.04$) and at D5 ($p = 0.02$). **(f)** Expression fold changes of were Col3 significantly lower at the grafted wounds compared to the ungrafted wounds at D1 ($p = 0.04$) and at D5 ($p = 0.003$). **(g)** Expression fold changes of Col1 were significantly lower at the grafted wounds compared to the ungrafted wounds at D5 ($p = 0.003$). Dotted line indicates expression fold change = 1 (i.e., no expression fold change below this). *N = 3.*

4.1.4. Inflammatory and proliferative growth factor profiles during wound repair in an autologous-grafted wound at a protein level

The antibody array quantified the relative protein expression of 23 targets (IGF-1, MCP-1, MIP-1α, TGF-β, VEGF-A, M-CSF, IL-10, TNF-α, IL-1α, IL-1β, IL-6, KC/CXCL-1, LIX/CXCL-5/6, IL-4, MMP-2, MMP-3, Fas Ligand, Fractalkine, RAGE, GCSF, TARC, IFN-γ and SDF-1α) in autologous-grafted beds (FTSG) and the ungrafted wound. When normalised against their own tail sample, there were no significant differences in the levels of the targets between the ungrafted wound ('FTSG – ungrafted' – see Figure 4.4) and the grafted wound ('FTSG – grafted').

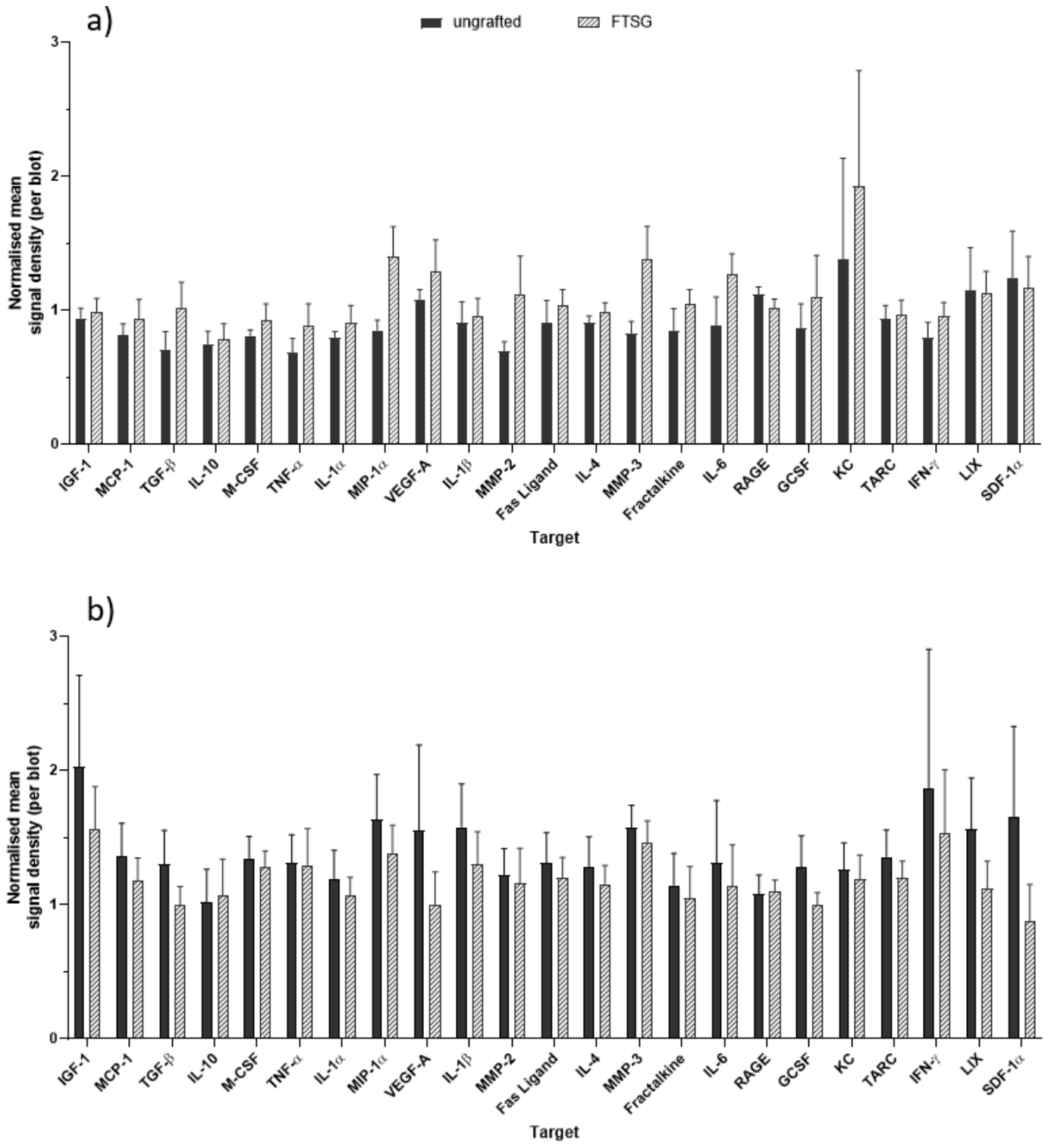

Figure 4.4: Protein levels of 23 targets in ungrafted full-thickness wounds (solid bars) and wounds grafted with FTSG (hashed bars) at (a) D5 and (b) D21 post-operation using Protein Array Membranes. Data was analysed using Array Analyser on ImageJ as signal densities, and normalised against the positive and negative controls as well as the blank spots on the array. The signal density of the particular target was also then normalised against the signal density of the tail of the same target. *N = 4.*

4.1.5. Discussion

Following investigation of wound repair in a full-thickness wound, the novel SKH-1 model was also utilised to investigate wound repair in grafted wounds. This also proved to be an effective facsimile for the trajectory of graft healing macroscopically. As there are limited studies that investigate the course of successful graft healing, it is somewhat more difficult to compare the histological and biomolecular results of our study. Nevertheless, all autologous FTSG for all four mice taken to the D21 endpoint were successfully taken, indicating that the model itself may have a future as a vehicle for investigating the behaviour of skin grafts.

There are clear differences in the way inflammatory and proliferative cytokines and growth factors behave at grafted and ungrafted wound beds at an RNA level within our model. If merely evaluating the effect of grafts on an ungrafted wound bed, it would be pertinent to state that grafts clearly dampen the effects of inflammation by reducing the levels of inflammatory growth factors and cytokines at an RNA level. However, these differences were not sustained at a protein level. This will be discussed further in Chapter 6.

CHAPTER 5: RESULTS

Investigating the molecular occurrences in a synthetically-grafted full-thickness wound bed and its differences with autografted beds

5. Results: Investigating the molecular changes in a synthetically-grafted full-thickness wound bed and its differences with autografted wounds

5.1. Introduction

In a similar fashion to the autologous-grafted full-thickness wound, we applied histological and protein analysis to investigate how a synthetic graft of BTM differs from the repair of a full-thickness wound in our model. This was also contrasted to how BTM and FTSG compare with each other in regards to the repair of a full-thickness wound

5.1.1. Macroscopic changes of a synthetically-grafted wound over 21 days

In this model, mice were grafted with 2 mm-thick BTM in place of a FTSG. The second, ungrafted full-thickness wound left to heal spontaneously as per previous. Mice wounds were analysed on D1, D5 and D21The full-thickness wound behaved similarly to the wounds of the full-thickness wound model (see Section 3.2) and the ungrafted wound from the FTSG-grafted group of mice (see Section 4.1).

The matte-like appearance of the ungrafted wound began to appear D10, with a continual development of the left-to-right contraction of the wound from this day through to the endpoint, as seen with the FTSG group. The nude colour of the wound bed was opaque compared to the colour of the native skin surrounding the wound. Again, epithelialisation was evident by the final endpoint of D21, and the wound was able to be separated into its epidermal and dermal layers for tissue processing following the cull.

The BTM sutured onto the other wound bed was cream and pink coloured and had its top polyurethane seal in-situ prior to the application of dressings at D0 (see Figure 5.1, a). By the first dressing change at D5, the BTM was more adhered to the wound bed and the centre of the graft appeared similar in colour to the adjacent, ungrafted wound. There remained an area of cream appearance around the periphery of the graft (see arrows on Figure 5.1, b). A strong chemical smell was appreciable upon removal of the dressings for all of the mice grafted with BTM that was not present in the mice grafted with FTSG. There was a minimal difference in the colour of the wound bed as seen under the BTM between days 10 and 15, which was a pink colour similar to the ungrafted wound. The cream appearance around the

periphery of the graft remained. A white wound exudate (not shown) was present for one of the mice grafted with BTM at D10, however this mouse remained well.

By the D21 endpoint, the colour of the wound underneath the BTM had changed from a pink to an almost completely cream colour, although different from the original appearance of the synthetic graft (see Figure 5.1, a vs. 5.1, e). The edges of the BTM seal were beginning to lift for all mice at this point; however, the centre remained adhered to the wound bed. The wound exudate observed for the single mouse out of continued to be present until D21. All mice that had synthetic grafts were completely integrated to the original wound bed edges, despite the slight lift of the seal around the graft periphery.

Some wound contraction was evident for both grafted and ungrafted wounds. The decrease in wound size from D0 was greater in the ungrafted wound compared to the grafted wound. By D21, the surface area of the wound sizes between the two were significantly different, with the grafted wound retaining 60% of its original wound size compared to the ungrafted wound, which retained less than 30% of its original wound size at D21. The difference between the surface area of the two wounds at D21 was significant (p = 0.02).

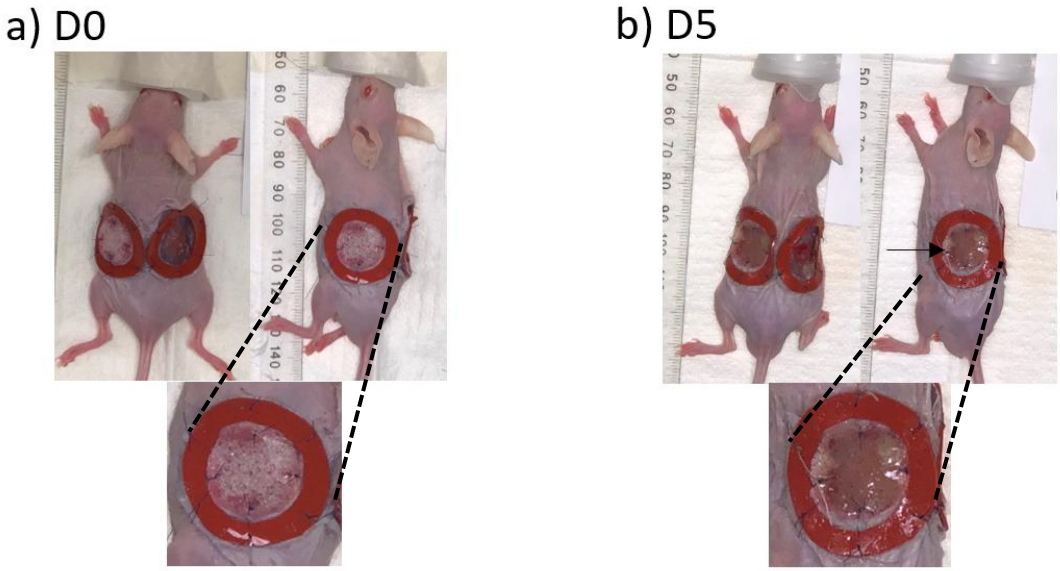

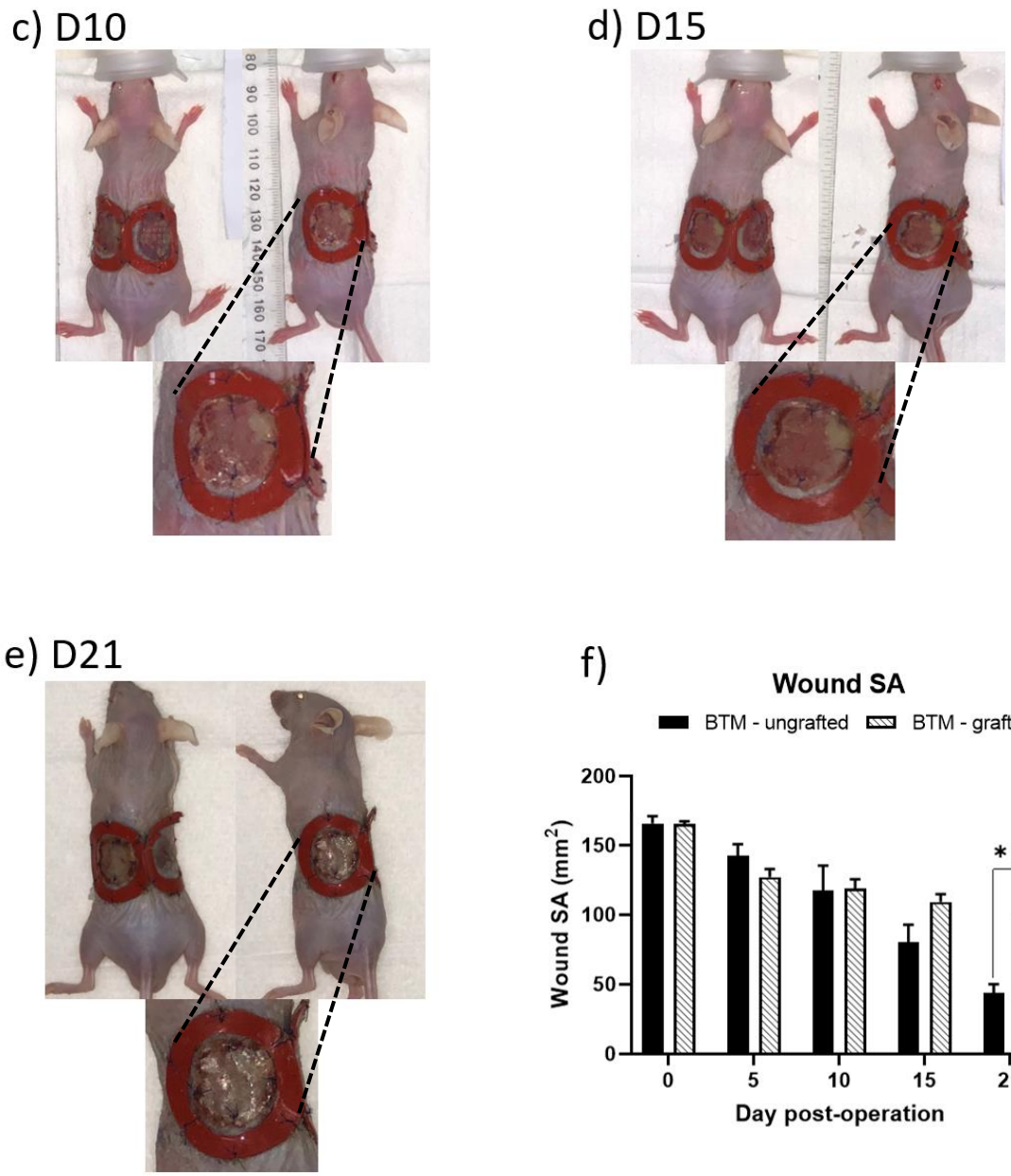

Figure 5.1: (a-e): Changes in a murine full-thickness wound grafted with BTM over 21 days. Macroscopic images taken with a camera phone on a tripod a fixed length and zoom. A ruler for scale within the image (not shown) was used for image analysis. The arrow on image (b) denotes the white graft edge. The wound bed, zoomed-in, is below the images of the mice. **(f):** Graph indicating the changes in the size of the wound surface area (SA) of the ungrafted (solid bars) and the grafted (shaded bars) wounds. The surface area of the grafted wound was significantly greater at D21 compared to the ungrafted wound (p = 0.001). *N = 4.*

5.1.2. Wound contraction in an autografted full-thickness wound versus a synthetically-grafted full-thickness wound

The size of the wounds with FTSG remained relatively stable whilst the wounds grafted with BTM experienced minor decrease in wound surface area (see Figure 5.2), decreasing in size over time through to the D21 endpoint. The wound surface area at the D21 endpoint was significantly less in those grafted with BTM than those grafted with FTSG (p = 0.01).

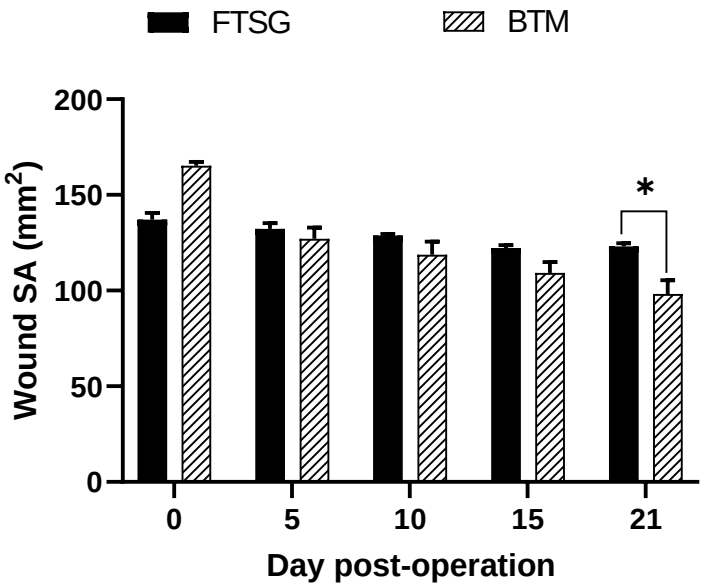

Figure 5.2: Wound surface area (mm^2) of full-thickness wounds grafted with FTSG versus full-thickness wounds grafted with BTM. Images of the mice that were taken through to D21 for both groups during the day of the operation, dressing changes and the D21 endpoint were analysed using ImageJ. Wound measurements for each grafted wound bed were normalised to the respective non-grafted wound control of each respective mouse before comparison between FTSG and BTM. The size of the wounds with FTSG remained relatively stable, whilst the wounds grafted with BTM experienced some minor decreases in wound surface area through to the D21 endpoint. The final surface area of wounds with FTSG were significantly greater than the wounds with BTM (p = 0.01). *N =4.*

5.1.3. Histological evaluation of synthetically-grafted wound repair using haematoxylin and eosin staining

The haematoxylin and eosin staining was performed in a similar fashion described in Section 2.4.2 and 4.2.

The appearance of the ungrafted wounds were similar to those at equivocal timepoints from the full-thickness wound model and the autografted-wound model. Again, nucleated inflammatory cells populated the wound bed at D1. Similar cells were seen at the bottom of the BTM in the grafted wound beds, and very few of these cells were present within the scaffold of the synthetic graft itself. It was difficult to appreciate clusters of possible endothelial cells or fibroblasts in the grafted wound bed sections. The synthetic graft, stained purple (see Figure 5.3a) was largely acellular. The top polyurethane seal was evident histologically in some, but not all specimens.

By D5, uncharacterised cells had begun to infiltrate the scaffold of the BTM, with inflammatory cells populating outside of the pores (see Figure 5.3b) and in an increased concentration at the wound edges. Neither an epidermis nor dermis were appreciable due to the disorganisation of the cells. By D21, the ungrafted wound bed had completely epithelialized. The edges of the wound bed grafted with BTM had epidermised (presumably, where the polyurethane seal had lifted); the middle of the wound bed did not have an epithelial layer. Again, the nucleated cells that populated the BTM resided around the pores of the synthetic scaffold. Masses of tissues/cells stained a dark pink and purple, possibly a breakdown of the scaffold were seen at the edges of the wound bed, although these have yet to be characterised.

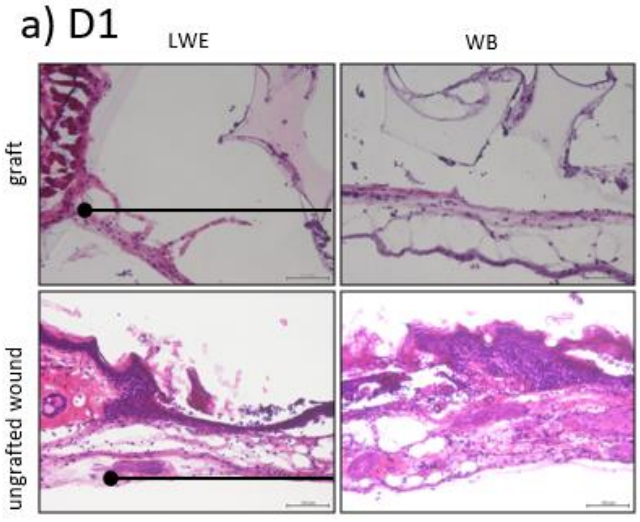

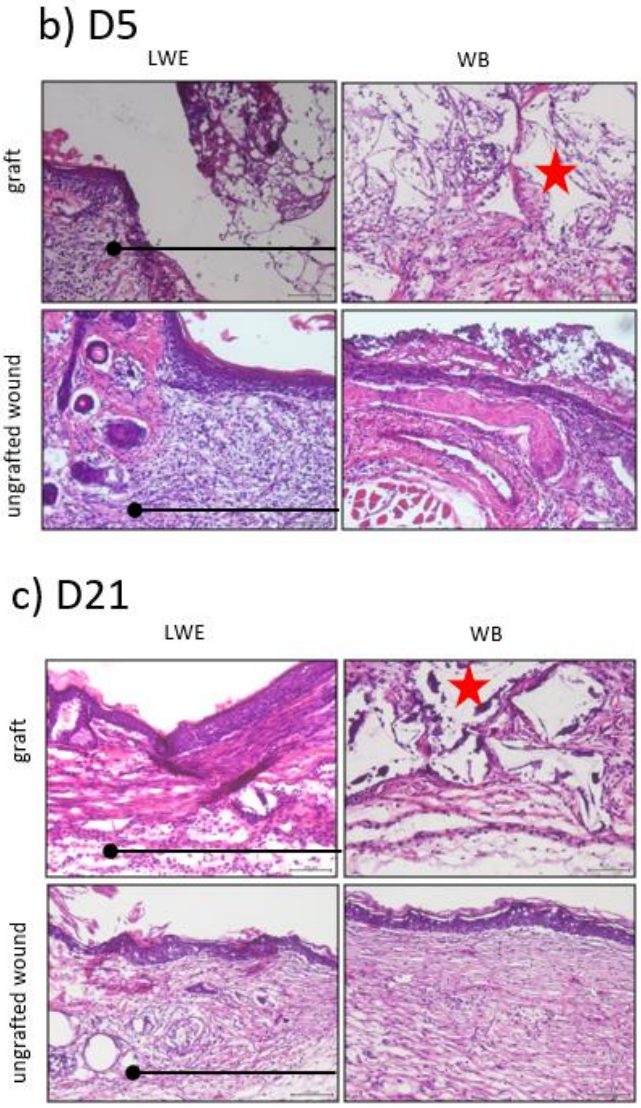

Figure 5.3: (a-c) Haematoxylin and eosin staining of a murine full-thickness wound bed with BTM and an ungrafted full-thickness wound at the inflammatory (D1), proliferative (D5) and remodelling (D21) timepoints. Line with left-sided dot indicates on LWE images indicates wound edge (dot) and wound bed (line). Stars on **(b)** and **(c)** denote the pores of the BTM scaffold. Scale bar reads 100µm for all images. *LWE: Left wound edge, WB: wound bed.*

5.1.4. Collagen deposition during wound repair in both autografted and synthetically-grafted murine full-thickness wounds

Masson's Trichrome staining of cryopreserved wound sections was again employed to investigate the collagen deposition in wounds. The collagen deposited in the ungrafted wounds of mice given grafts, as seen through staining, was similar in appearance to the wounds analysed in the full-thickness wound model (see Figure 3.3 and Section 3.4).

Comparatively, wounds grafted with FTSG had more collagen than wounds grafted with BTM. At the inflammatory, proliferative and remodelling endpoints encompassed in our study, wounds grafted with FTSG had significantly more collagen than those with BTM (D1: p = 0.0012, D5: p = 0.015, D21: p = 0.029).

In wounds grafted with FTSG, there was a more-than two-fold expression of collagen at D1 than wounds grafted with BTM. This increased slightly at D5, which was the endpoint that produced the highest amount of collagen staining, before decreasing again at D21. The difference between the amount at D1 and D5 was not significant. The differences between the other timepoints were significant (D1 and D21: p = 0.01, D5 and D21: p = 0.004) (see Figure 5.6).

The trend was similar for those wounds grafted with BTM (amount of collagen rising between D1 and D5 before decreasing again at D21. Within the BTM group, the area stained for collagen was highest at D5, with significant differences between D1 and D21 (p = 0.04).

Wounds grafted with FTSG experienced a 54% decrease in the amount of collagen (2.7 at D5 versus 1.5 at D21). Wounds grafted with BTM experienced a 58% decrease in the amount of collagen calculated between D5 and D21 (1.07 at D5 versus 0.64 at D21).

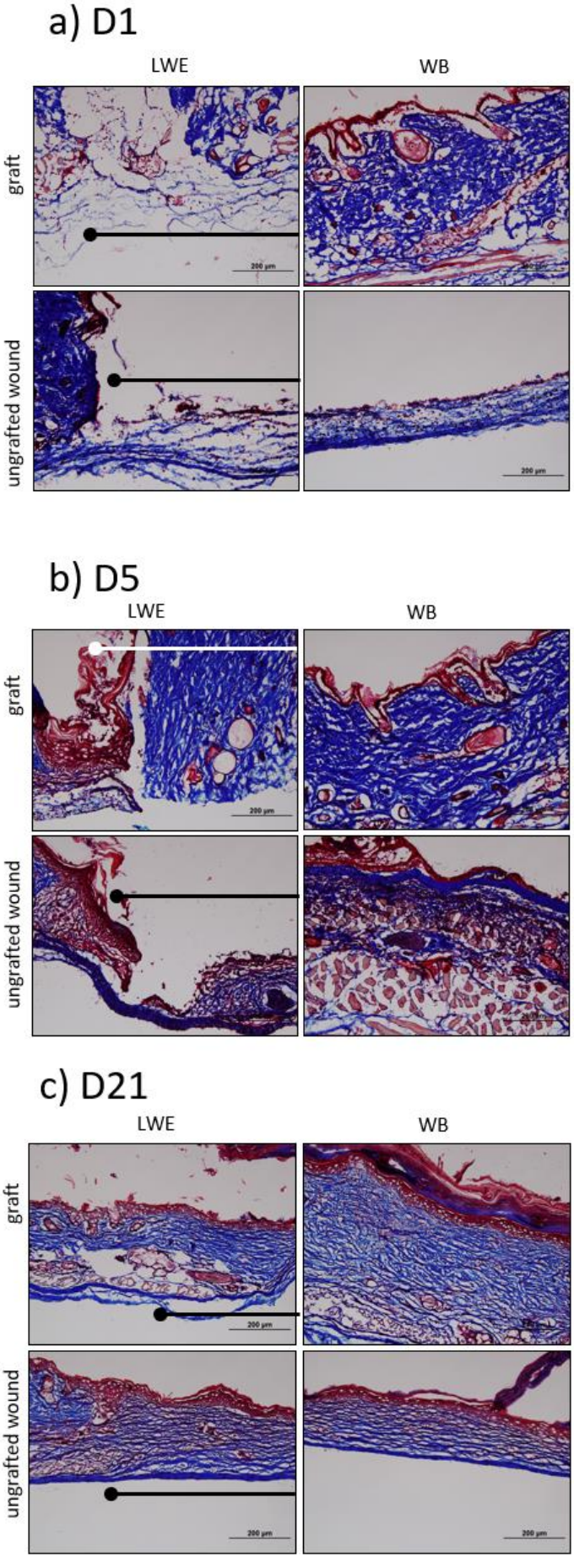
a) D1
LWE
WB
graft
ungrafted wound
b) D5
LWE
WB
graft
ungrafted wound
c) D21
LWE
WB
graft
ungrafted wound

Figure 5.4: Collagen deposition using Masson's Trichrome staining of a murine full-thickness wound with FTSG and an ungrafted full-thickness wound at the inflammatory (a, D1), proliferative (b, D5) and remodelling (c, D21) timepoints. Line with left-sided dot indicates on LWE images indicates wound edge (dot) and wound bed (line). Bottom right images are tail and D0 images. Scale bar reads 200µm for all images. *LWE: Left wound edge, WB: wound bed.*

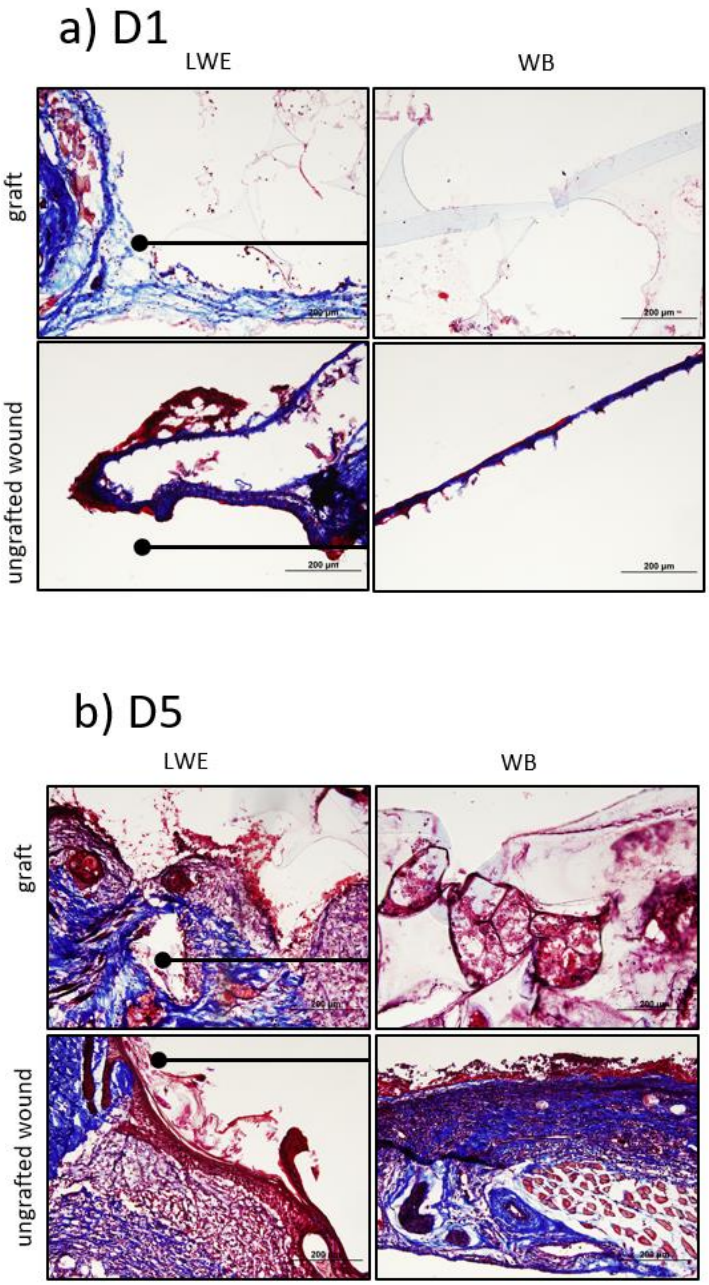

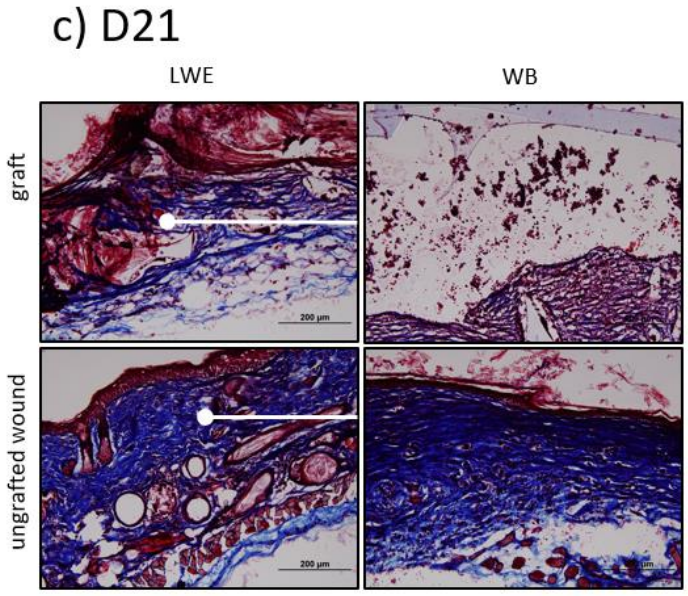

Figure 5.5: (a-c) Collagen deposition using Masson's Trichrome staining of a murine full-thickness wound with BTM and an ungrafted full-thickness wound at the inflammatory (a, D1), proliferative (b, D5) and remodelling (c, D21) timepoints. Line with left-sided dot indicates on LWE images indicates wound edge (dot) and wound bed (line). Bottom right images are tail and D0 images. Scale bar reads 200µm for all images. *LWE: Left wound edge, WB: wound bed.*

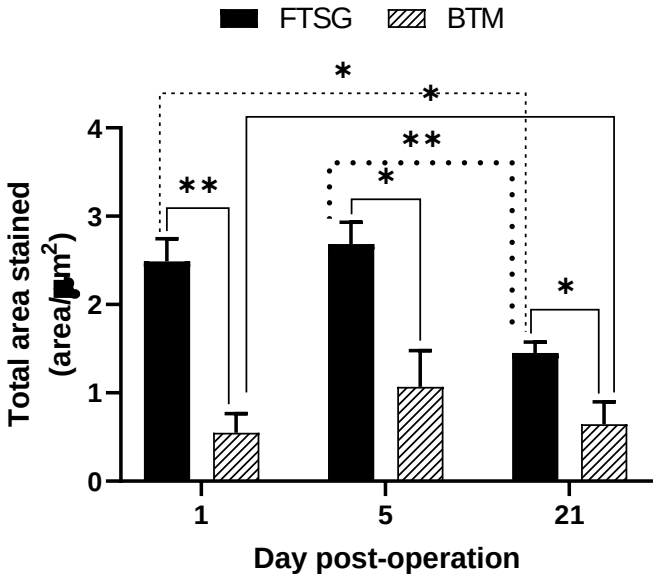

Figure 5.6: Quantification of the total collagen area stained blue (area per µm²) with Masson's Trichrome at Days 1, 5 and 21 post-operation in full-thickness wounds grafted with FTSG (solid bars) and BTM (hashed bars). The total area stained for collagen was normalised against the area of collagen stained at both wound edges rather for a consistent comparator directly at the wound bed. The total area stained for collagen was significantly lower at all timepoints in full-thickness wounds grafted with BTM (* $p < 0.05$, ** $p < 0.01$) compared to FTSG. $N = 4$.

5.1.5. Inflammatory and proliferative growth factor profiles during wound repair in a synthetically-grafted wound at an RNA level

The fold expression of IL-6, CXCL-1, and CXCL-5/6 were all higher in the ungrafted wound beds compared to their grafted counterparts at during the inflammatory and proliferative timepoints (see Figure 5.7 a-c). However, the only target to yield significance was IL-6 at D1 and D5, where levels of this inflammatory target were lower in the grafted wound beds.

Similar to the autografted group, levels of VEGF-A and TGF-β1 were lower at the grafted wound beds compared to the ungrafted control, however this did not reach significance (Figure 5.7 d-e). The levels of VEGF-A at D21 were also higher at the ungrafted wound bed, and although this was not significant, the difference in fold expression change was greater at this time point between grafted and ungrafted wound bed than at the two earlier time points.

Col3 expression at D5 was higher in the ungrafted wound compared to the grafted wound bed (p = 0.006) (Figure 5.7 d). Unlike the autografted group, levels of TGF-β1, Col3 and Col1 at D21 were higher in the grafted wound, although the differences were not significant.

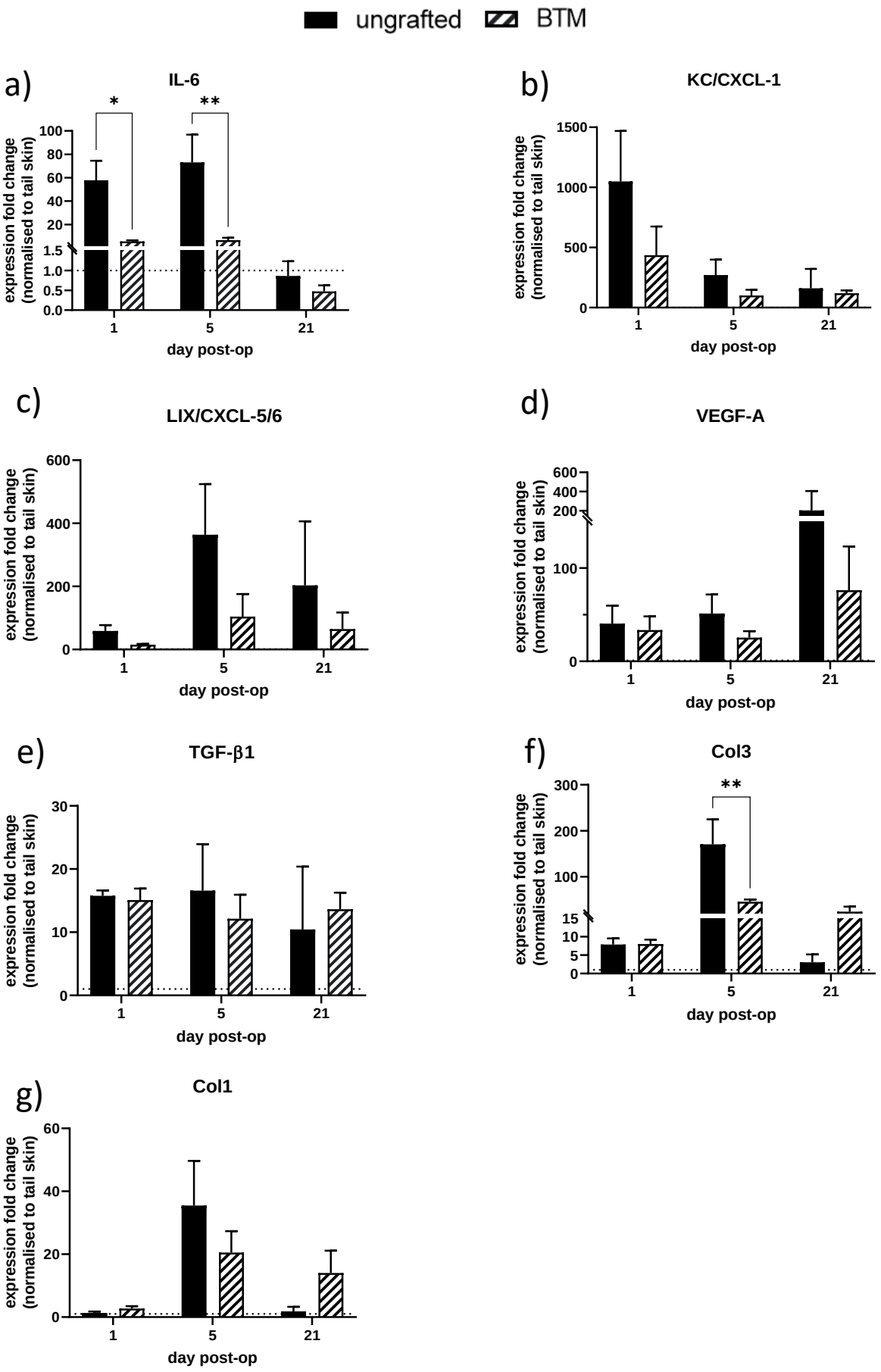
ungrafted
BTM
a)
IL-6
*
**
expression fold change (normalised to tail skin)
day post-op
b)
KC/CXCL-1
c)
LIX/CXCL-5/6
d)
VEGF-A
e)
TGF-β1
f)
Col3
g)
Col1

Figure 5.7: (a-g) Quantitative RT-PCR results of inflammatory and proliferative cytokine/growth factor targets of ungrafted full-thickness wounds (solid bars) and wounds grafted with BTM (hashed bars). Data was analysed as expression fold changes of the targets against the average of the C_t values of three housekeeping genes (Polr2A, EF1A1, Tuba1A), and normalised against the C_t values of the same genes of the tail skin. Two-way ANOVA was used to compare the two groups (ungrafted, BTM) at the three time-points. **(a)** Expression fold changes of IL-6 were significantly lower at the grafted wounds compared to the ungrafted wounds at D1 (* $p = 0.03$) and D5 (** $p = 0.006$). **(b-e, g)** Expression fold changes of CXCL-1, CXCL-5/6, VEGF-A, TGF-β1 and Col1 were not significant at any of the time points examined. **(f)** Expression fold changes of were Col3 significantly lower at the grafted wounds compared to the ungrafted wounds at D5 (** $p = 0.006$). Dotted line indicates expression fold change = 1 (i.e., no expression fold change below this). *N = 3.*

5.1.6. Inflammatory and proliferative growth factor profiles during wound repair in a synthetically-grafted wound at a protein level

The same protein antibody arrays were used as in the autologous-grafted mouse model as was in the synthetically-grafted model (*n*=4). Of the 23 targets, KC (CXCL-1) demonstrated the highest mean signal density for both the grafted and ungrafted wounds at the D5 endpoint. This, along with MIP-1α and IL-6, demonstrated differences in the mean signal density between the grafted and ungrafted wounds. Protein expression of MIP-1α at D5 was significantly higher in the grafted wound bed than in the ungrafted wound ($p = 0.02$); whilst expression of IL-6 was significantly lower in the grafted wound ($p = 0.04$) (see Figure 5.8a). The remaining targets demonstrated similar mean signal densities between the two wounds at D5.

At the D21 endpoint, levels of IGF-1 were higher in the grafted wound compared to the ungrafted wound, though this difference was not significant. Again, there were differences in expression levels of KC, with the higher expression in the wounds grafted with BTM compared to the ungrafted wounds ($p = 0.004$) (see Figure 5.8b). The other targets interrogated with the Protein Array Membranes did not reveal any differences between the ungrafted and grafted wounds of the mice in the BTM graft group.

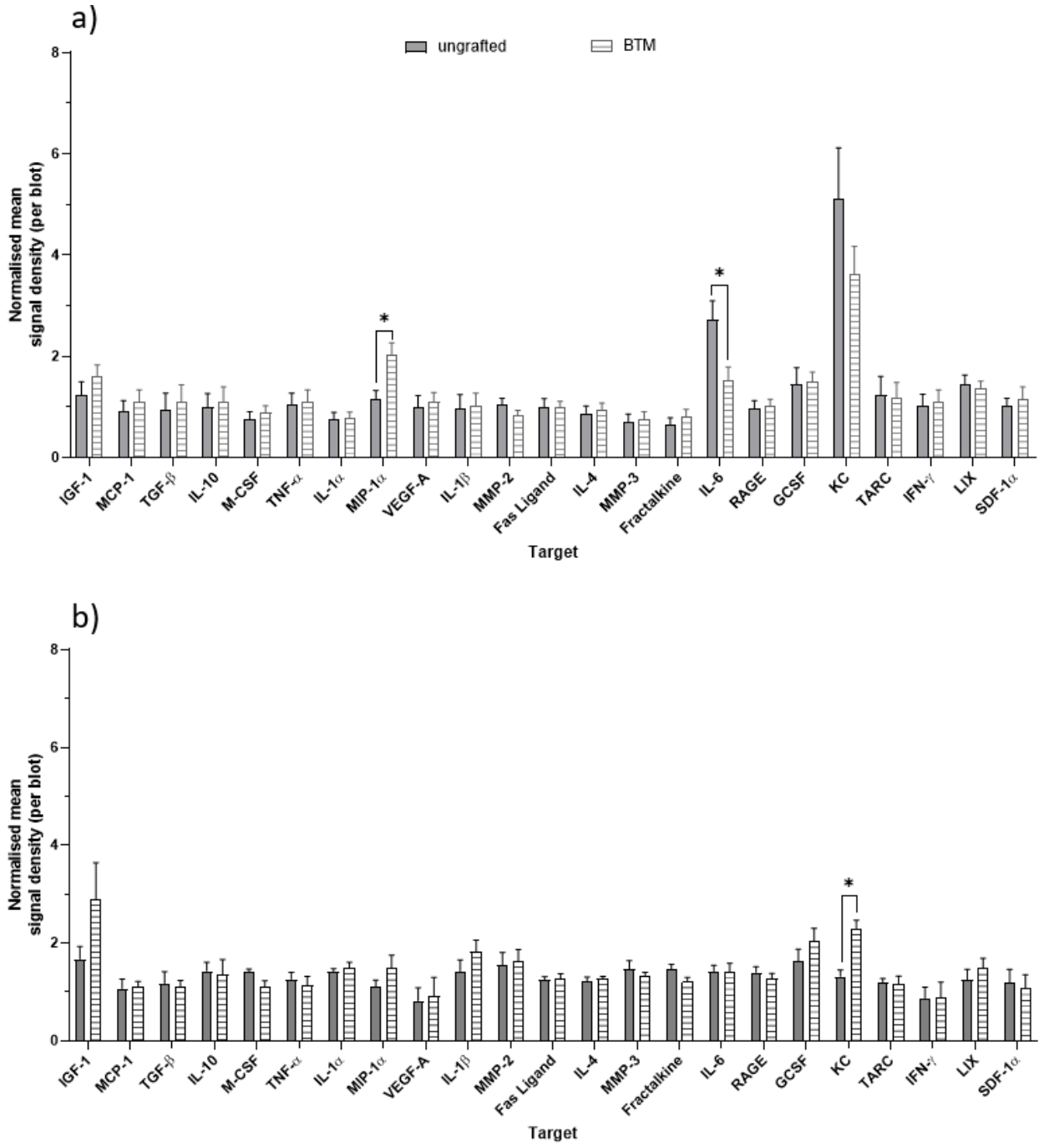

Figure 5.8: Protein levels of 23 targets in ungrafted full-thickness wounds (solid bars) and wounds grafted with BTM (hashed bars) at (a) D5 and (b) D21 post-operation using Protein Array Membranes. Data was analysed using Array Analyser on ImageJ as signal densities, and normalised against the positive and negative controls as well as the blank spots on the array. The signal density of the particular target was also then normalised against the signal density of the tail of the same target. ANOVA was used to analyse results. **(a)** Protein expression of MIP-1$^{\alpha}$ at D5 was significantly higher in the grafted wound bed than in the ungrafted wound (p = 0.02); whilst expression of IL-6 was significantly lower in the grafted wound (p = 0.04). **(b)** Protein expression of KC/CXCL-1 at D21 was significantly higher in the grafted than in the ungrafted wound (p = 0.004). *N = 4.*

5.1.7. Inflammatory and proliferative growth factor profile differences between wound repair in an autologous-grafted and synthetically-grafted wound at a protein level

When comparing between the two graft groups, the differences in protein expression was most evident at the D5 endpoint. IL-6 expression was significantly lower in wounds grafted with BTM than with FTSG at D5 (p = 0.02); and wounds grafted with BTM expressed significantly higher levels of IL-6 at D21 compared to D5 (p = 0.009) (see Figure 5.9b). IL-1β levels were significantly higher in wounds grafted with BTM at D21 (p = 0.02).

The IL-8 homologues also had significant differences, with KC/CXCL-1 expression significantly different between days and grafts. Wounds grafted with FTSG had higher levels at D5 (p = 0.04); the opposite was true at the D21 endpoint, where there were higher levels in wounds grafted with BTM at D21 (p = 0.01). Levels decreased significantly between D5 and D21 in wounds grafted with FTSG (p = 0.04) but increased between D5 and D21 in wounds grafted with BTM (p = 0.01). LIX/CXCL-5/6 expression was significantly higher in wounds grafted with BTM at D21 (0.007) (see Figure 5.9d and 5.9e).

There were no significant differences in the levels of TGF-β1, IL-10 or VEGF-A between D5 and D21 post-operation at either the wounds grafted with FTSG or BTM. MMP-2 expression was higher in wounds grafted with FTSG than in BTM (p = 0.04) at D5, but similar on D21 (see Figure 5.10d). Expression of the remodelling protein increased between D5 and D21 in wounds grafted with BTM (p = 0.02). The expression of MMP-3 decreased between D5 and D21 in wounds grafted with FTSG (p = 0.04) (see Figure 5.10e).

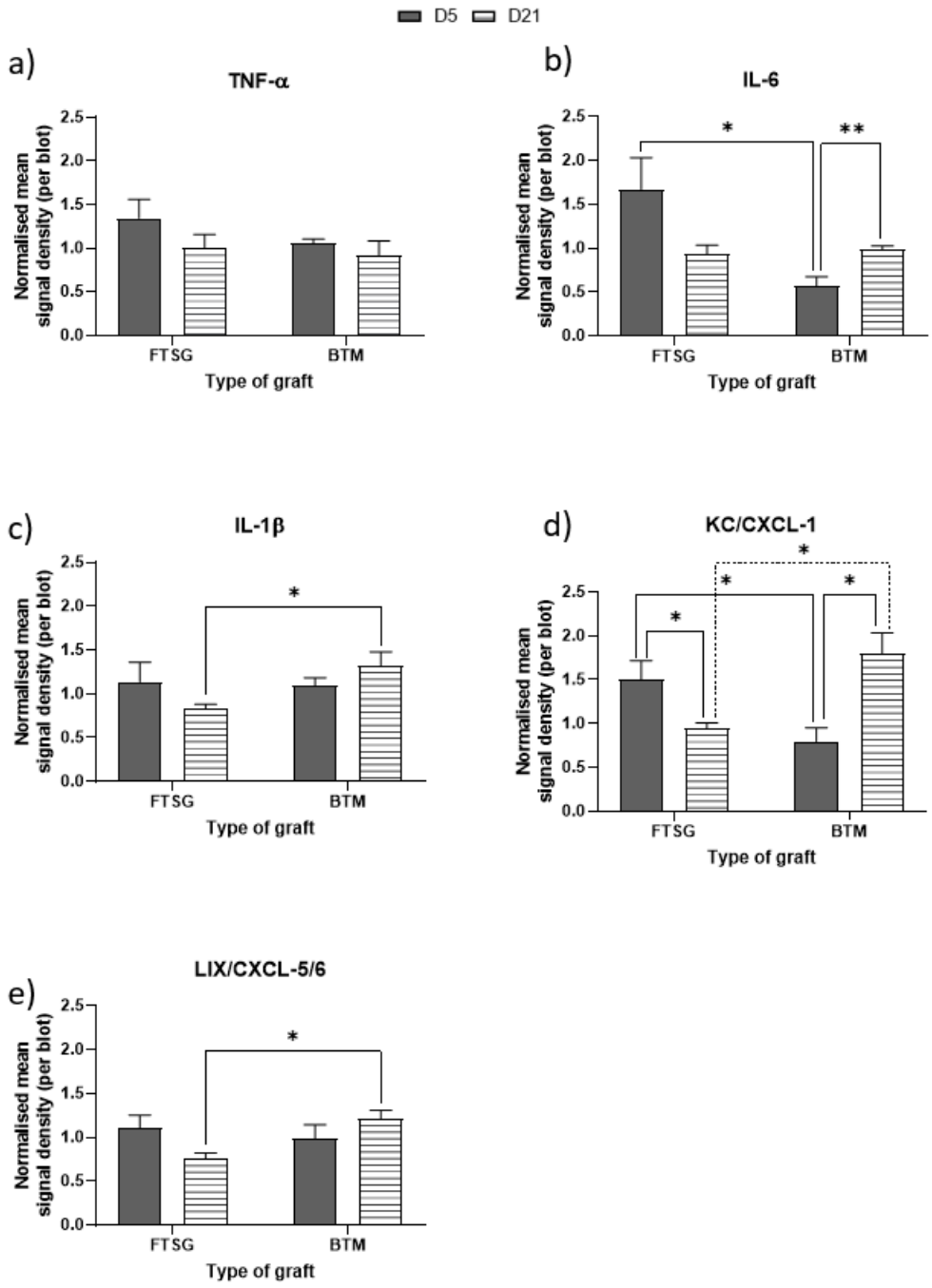

Figure 5.9: (a-e) Protein levels of inflammatory targets in grafted wounds at D5 (solid bars) and D21 (hashed bars) post-operation. Protein levels for each grafted wound bed were normalised to the respective non-grafted wound control of each respective mouse before comparison between FTSG and BTM. **(a)** There were no significant differences in the levels of TNF-α between D5 and D21 post-operation in either graft group. **(b)** IL-6 expression was significantly lower in wounds grafted with BTM than with FTSG at D5 and wounds grafted with BTM expressed significantly higher levels of IL-6 at D21 compared to D5. **(c)** IL-1β levels were significantly higher in wounds grafted with BTM at D21. **(d)** KC/CXCL-1 expression was significantly different between days and grafts, with higher levels in wounds grafted FTSG at D5, higher levels in wounds grafted with BTM at D21; as well as decreasing between D5 and D21 in wounds grafted with FTSG but increasing between D5 and D21 in wounds grafted with

BTM. **(e)** LIX/CXCL-5/6 expression was significantly higher in wounds grafted with BTM at D21. (* p <0.05, ** p <0.01). Grafted wound bed data is normalised to the non-grafted wound bed of the respective mouse prior to comparison between the two grafts. *N =4.*

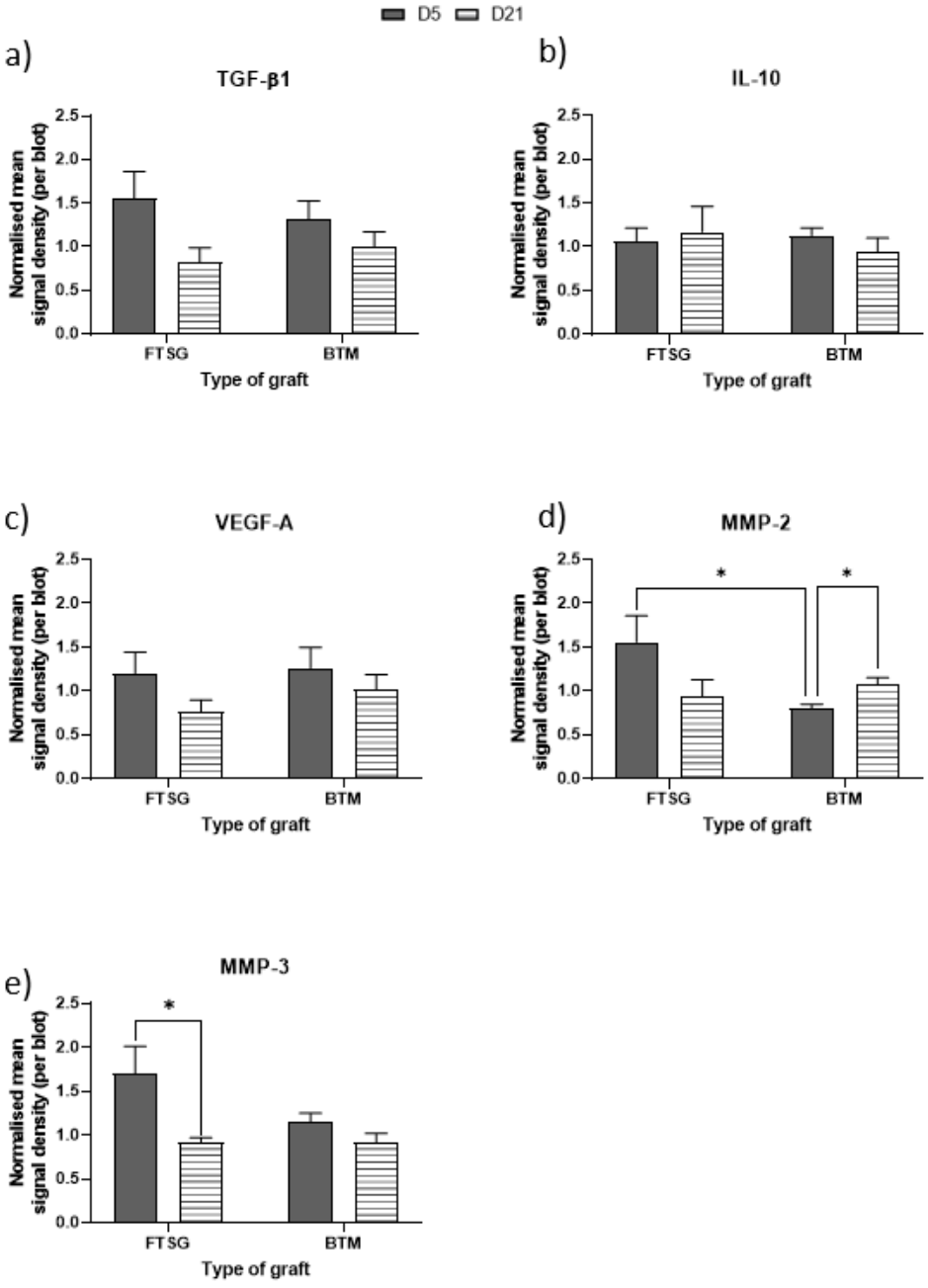

Figure 5.10: (a-e) Protein levels of proliferation/remodelling targets in grafted wounds at D5 (solid bars) and D21 (hashed bars) post-operation using Protein Array Membranes. Protein levels for each grafted wound bed were normalised to the respective non-grafted wound control of each respective mouse before comparison between FTSG and BTM. **(a-c)** There were no significant differences in the levels of TGF-β1, IL-10 or VEGF-A between D5 and D21 post-operation at either the wounds grafted with FTSG or BTM. **(d)** MMP-2 expression

was higher in wounds grafted with FTSG than in BTM at D5 but similar in D21; expression increased between D5 and D21 in wounds grafted with BTM. **(e)** MMP-3 expression decreased between D5 and D21 in wounds grafted with FTSG. (* $p < 0.05$). Grafted wound bed data is normalised to the non-grafted wound bed of the respective mouse prior to comparison between the two grafts. *N = 4.*

5.1.8. Discussion

The behaviour of wounds grafted with BTM clearly differs at a biomolecular level compared to wounds grafted with FTSG. Within the BTM graft group itself, the differences between ungrafted and grafted wounds are minimal. This result is similar to the FTSG group. Again, accounting for this may be as simple as increasing the cohort size from $n = 4$. It may also be that as BTM is an acellular dermal template, both ungrafted and grafted wounds need to be populated cells through their interactions at the matrix level, whereas the FTSG already has pre-existing fibroblasts and keratinocytes that accompany it as a native graft.

All four mice in the BTM groups required extra care and animal husbandry as they experienced weight loss between 5-16% of their initial post-operative weight with bandages on at D0 (all mice that lost greater than 5% of this initial weight was placed on a regimen of additional care, which included more regular animal checks and supplemental dietary additions such as seeds and diabetic jelly). In comparison, the four mice that received FTSGs did not lose the weight required for extra care by the D21 endpoint.

All of the four mice in the BTM groups had synthetic grafts that were considered to be successfully integrated into the wound bed. As these grafts did not have an epithelial layer, their grafts cannot be considered healed in the same fashion as the wounds with FTSG.

Similar to wounds in humans grafted with BTM, this non-biodegradable polyurethane seal would need to be removed (called “delamination”), and an epidermis provided by the D21 endpoint if the point of healing is to be considered as epidermisation. In humans, this epidermis is provided as an autologous split-thickness skin graft (STSG or SSG). It would be of interest to observe what would happen should the polyurethane seal be removed in a similar cohort of mice, the splinting silicon ring removed in this mouse model.

CHAPTER 6: DISCUSSION AND CONCLUSIONS

Investigating the molecular occurrences in synthetically-grafted full-thickness wound bed and its differences with autografted beds

6. Discussion

6.1. Wound repair in the novel SKH-1 full-thickness wound model is a close representation of wound repair in humans

6.1.1. The SKH-1 mouse wound during inflammation

A wound is generally hypoxic upon injury due to endothelial damage and the infiltration of leukocytes that require oxygen uptake for function. The early inflammation phase of wound repair in humans occurs 0-2 days post injury, and is marked by neutrophil recruitment and their invasion into the wound bed. Days 2-3 post injury sees macrophages replacing neutrophils as the major immune cell to affect changes within the wound bed.

The re-epithelialisation that is required for wounds close was replicated in this novel SKH-1 model. This process began with the infiltration of inflammatory cells into the wound bed at the first endpoint investigated, D1 (see Figure 3.2a, D1 boxes) This follows the normal trajectory of spontaneous wound repair in humans[54, 55]. Although the cells are uncharacterised in this study, observation of the cells stained with haematoxylin and eosin under high magnification revealed that these cells had multi-lobar nuclei. This gives us clues as to their possible identity as neutrophils. Future work could include the characterisation of these cells using immunohistochemical techniques, for example with Ly-6G/Gr-1^{+} to examine neutrophils[217].

During inflammation in humans, neutrophils are recruited to the injury site via the by-products of platelet degranulation such as histamine and bradykinin[60]. They release inflammatory mediators such as IL-1β, TNF-α, and IL-6.

Given it is not spontaneously produced by intact normal cells, IL-6 is commonly used as a marker to investigate the first stage of wound repair and inflammation. The IL-6 ELISA performed on wound bed samples and the tail demonstrated the significant differences in local and systemic IL-6 levels, respectively.

There was an upwards trend of IL-6 expression at the wound beds over 21 days, whereas the opposite was seen at the tail. This suggests that IL-6 has possible systemic functions, and that the systemic IL-6 may also differ in behaviour or interactions to the IL-6 function at the wound bed in this model. With this in mind, the growth factors' expression levels analysed by RT-PCR was normalised against the tail skin to account for the likelihood that the other

cytokines/growth factors of interest had systemic actions in unwounded skin, thus eliminating any confounding information and allowing the results to focus solely on the changes at the full-thickness wound bed.

Peaks of IL-6 are consistently seen within hours following injury in murine skin lesion and excisional wound models[67, 68], and again at greater than 72 hours following injury[73], suggesting the possible role of IL-6 during the later stages of wound repair.

The first 18-24 hours of wound repair in our model was generally not observed; however, the biphasic peaks of IL-6 at the wound bed seen in the literature is also seen in our model, with peaks at D5 and D14 post-operation at an RNA level, and to a lesser degree at a protein level.

Of the cells that produce IL-6, macrophages may be responsible for the first peak seen at D5 in the wound bed. By D14, it is more likely that epidermal keratinocytes are producing IL-6. Haematoxylin and eosin staining demonstrated the increasing organisation of the cells at the wound by D8, and a dermis likely populated with fibroblasts becomes more evident. Fibroblasts cause the proliferation and migration of keratinocytes through IL-6, which may thus account for the hyperproliferation of the epidermis in the SKH-1 model at this timepoint.

With increases in IL-6, there are concurrent increases of TNF-α and IL-1β within hours post-wounding in murine models of partial-thickness wound repair. TNF-α levels peaked at 72 hours at both RNA and protein levels in a murine excisional wound healing model[69]. The peak of IL-1β was seen at 24 hours post wounding compared to a non-wounded model[69]. Within the early stages of wound repair, our model demonstrated increasing levels of both TNF-α and IL-1β at an RNA level, peaking at D5, declining during the proliferative phase, and rising once again to reach a larger peak at 21.

Both TNF-α and IL-1β are produced by platelets during early inflammation, attracting neutrophils to the wound and subsequently being produced by macrophages[59]. This coincides with their rise in the inflammatory phase of wound repair in our model. IL-1β stimulates fibroblasts, which in turn causes the keratinocyte proliferation and migration through IL-6. In addition to their function within inflammation, both TNF-α and IL-1β induce and regulate collagen synthesis[218] through inducing matrix metalloproteinase transcription, which likely accounts for collagen and MMP peaks during proliferation (days 5-14).

IL-8 is also expressed in cutaneous repair. In humans, its levels begin to rise at D1 after cutaneous injury, declining at D4[219]. Rodents lack a direct homologue of IL-8; however, KC (keratinocyte-derived chemokine, CXCL-1) and LIX (CXCL-5/6) are considered functional homologues due to their heavy involvement in neutrophil recruitment[220]. Topically applied IL-8 on human skin grafts applied to a mouse model enhanced re-epithelialisation over non-grafted controls, with wound contraction significantly diminished by IL-8[221]. IL-1β has also been seen to stimulate keratinocytes and fibroblasts to produce KC[78].

The decline of IL-8 seen in humans during the proliferative stage is mimicked in our murine model, with RNA levels of both KC and LIX increasing to D5, subsequently declining, and rising again during the late proliferation/early remodelling.

6.1.2. The SKH-1 mouse wound during proliferation and remodelling

As well as the inflammatory phase, the SKH-1 mouse model also observed the proliferative phase, demonstrating epithelialisation from D5 both macroscopically and histologically. The model also exhibited the synthesis of an extracellular matrix/granulation tissue. It is expected that fibroblasts infiltrate the wound bed by D3-4 in human models, which is difficult to extrapolate to our model given neither day is specifically captured in our study. Nevertheless, the fact that a dermis begins to make itself evident by D5 in our mouse model may be enough to indicate that proliferation in our model is following the trajectory as stipulated in the literature[54, 57, 222].

As the levels of TGF-β1 increases in the wound bed, fibroblasts appear at the wound edge and may begin transforming into contractile cells, causing the wound to contract. The levels of TGF-β1 in our model increased from D1-D5, declined, before rising again to a larger peak at D21. Immunohistochemical staining for α-smooth muscle antibody (α-SMA) can be employed to evaluate the presence of contractile myofibroblasts in the wound beds. However, it is of interest to note that the unidentified cells as seen in Figure 3.2b, which sat at a perpendicular orientation to the rest of the cells in the granulation tissue, began to appear at the D5 timepoint. Cells of similar appearance have previously been seen in a healing diabetic foot ulcer in a human case study, when the wound was beginning to contract[223].

IL-10 regulates the synthesis of pro-inflammatory cytokines, which may explain why peaks of this anti-inflammatory cytokine are seen within the first few days post cutaneous injury in a

murine model[124] as well as in this study. It has also previously been postulated that IL-10 may play a suppressive role in fibrosis and scarring through the acceleration of re-epithelialisation and improved wound revascularisation, exhibiting a possible inverse relationship with TGF-β1[224]. This trend is also seen in our mouse model (see Figure 3.5a-b). PDGF-BB also directly increases fibroblast proliferation, as well as indirectly through its effects on other cytokines such as TNF-α, and TGF-β1[54]. It also induces the myofibroblast phenotype[59]; and in our study, it followed a similar trend in fold expression changes to TGF-β1 (see Figure 3.5c).

Vascularisation is important in spontaneous wound repair and wound repair via grafts. Hypoxia begins the initial infiltration of cells that secrete a cascade of growth factors which encourage vascularisation. Keratinocytes at the wound edge are the main source of VEGF-A in addition to macrophages, fibroblasts and other endothelial cells. Vascularisation was not directly investigated in our study. The initial steep rise of the RNA levels of VEGF-A (see Figure 3.5d) may indicate that vascularisation is crucial within the early phase of wound healing, as the formation of the granulation tissue requires a large amount of nutritional support that can only be acquired through vessels. Both TGF-β1 and IL-1 also indirectly induce VEGF production through their actions on the fibroblasts and myofibroblasts[54]. Thus, peak of VEGF-A mRNA corresponding with a peak of TGF-β1 and IL-1β is justifiable.

It is expected that as the cells of the wound begin to organise into an epidermis and dermis during proliferation, collagen synthesis and concurrent remodelling begins.

In humans, Col3 (the first subtype to appear at the wound bed as part of the provisional matrix laid down proliferation) is seen to appear earliest at 2-3 days following injury; Col1 appears later at approximately 5 days[225]. Col1 peaks between days 11 and 21 post wounding but continues to be modified in terms of fibre density, structure, orientation, and cross-linking over a long period of time[128, 130]. Our mouse model saw increases of Col3 and Col1 from D1 to D5, with significant differences only in Col1 levels. Although Col3 expression changes over 21 days did not reach significant changes, the trend remained similar as previously described to Col3 patterns in human wound repair, in that Col3 appears earlier than Col1 with a direction for an increase in the appearance and expression of both. As our study terminates at D21, an endpoint that sits at the cusp of proliferation and remodelling, the lack of a distinct difference between the expression fold change of Col3 and Col1 at D21 may be reflective of the matrix's state of change. Remodelling can last for months to years[54], and as such, perhaps the relative

amount of Col3 and Col1 and the difference are likely to be more apparent as the wound ages and remodels.

As well as RT-PCR data, Masson's Trichome staining was employed to histologically evaluate collagen synthesis to great effect (see Figure 3.3). Simple observation under microscopy of the sections with Masson's Trichrome allows for the appreciation of the increasing collagen deposition that occurs throughout spontaneous wound healing. In addition, it is clear that the overall structure and appearance of collagen within the granulation tissue changes with time, allowing for the recognition of older versus newer collagen as well as the transition of 'parallel-like' immature collagen to the 'basket-weave' pattern of collagen in normal skin[132]. The remodelling that is mediated by MMPs and TIMPs was not directly evaluated in the full-thickness wound model of this study. Expression of MMP-2 and MMP-3 was measured in the autografted and synthetically-grafted mouse models (see Chapters 4 and 5).

Collagen deposition follows the path of the fibroblasts, which attach to the cables of the provisional matrix[222] following their appearance from the wound edges[96]. A recent paper by Jalili *et. al.* determined that full-thickness wounds grafted with autologous split-thickness skin grafts in a porcine model healed from the bottom up[175]. The relative density of the blue-stained fibres, particularly at D5 and D8, is higher at the wound edges when observing sections under microscopy. Although Masson's Trichrome cannot readily distinguish between Col3 or Col1, it is able to identify freshly-deposited collagen and established collagen via darkness of the blue stain produced (i.e., freshly-deposited collagen is a lighter blue, 'older' and collagen is darker blue). As such, the darker blue is present at the edges in sections from D5-21 at the wound beds of sections from D14 and 21. In addition, granulation tissue stained a lighter blue was found closer to the epidermis. Therefore, in this mouse model, collagen is deposited not only from the wound edges, but also from the bottom of the wound bed upwards. In addition, image analysis suggests that collagen deposition is significantly increased between inflammation and proliferation/early remodelling (see Figure 3.3b).

6.1.3. The selection of inflammatory, proliferation and remodelling endpoints to examine wound engraftment as guided by the results of the SKH-1 full-thickness wound mouse model

In order to guide the endpoints in experiments using the final two animal models of our study, data was collated as above and a decision was made to use the D1 (inflammation),

D5 (proliferation) and D21 (remodelling). This novel SKH-1 model demonstrated through the RNA data that the fold expression changes of various targets were not significantly different between D1 and D2. Further, the earlier peaks of the targets seemed to fall on the D5 endpoint, which indicated that this would be an appropriate endpoint to observe the behaviour of many target cytokines/growth factors that were likely to be present. It also underscored the transitional state of the wound bed as seen histologically, changing from a wound bed infiltrated with inflammatory cells to one that was seeking repair through granulation tissue synthesis.

Given the multiple cellular interactions during wound repair, it is difficult to state which cells are directly responsible for the secretion and/or synthesis of the various inflammatory cytokines; rather, it is likely that the complexity of wound repair in humans is also reflected in the SKH-1 mouse model. Further studies to characterise the nature of the inflammatory cells and dermal cells (by way of flow cytometry or immunohistochemistry) may give us further insight into the wound repair behaviour in this model. Notwithstanding this however, the characterisation of spontaneous wound repair in an SKH-1 mouse model is invaluable in providing comparative insight into wound repair via grafts. In addition to this and even with the small sample size for each experiment (*n* = 2-4 for Masson's Trichrome analysis, *n* = 3 for RT-PCR data, *n* = 3 for IL-6 ELISA), it is clear that this mouse model is an appropriate animal model in which to investigate wound repair.

6.2. Wound repair in the novel SKH-1 full-thickness wound by grafting

6.2.1. Skin grafts inhibit the wound contraction of an autografted full-thickness wound in the SKH-1 mouse model

The application of a full-thickness skin graft to cover a wound is regularly employed in Plastic and Reconstructive Surgery.

The behaviour of the murine full-thickness skin grafts under examination during the regular dressing changes were surprisingly similar to the behaviour of FTSGs in humans; in that, macroscopically, the graft may look hyperaemic around the graft edges with pronounced pallor centrally at approximately 5-10 days post-operation. Regular dressing changes are necessary to ensure the graft, in humans, is kept moist and to ensure graft take/healing.

It is not uncommon that FTSGs in humans within this initial 5-10 period require minor debridement to eliminate graft eschar that may form on top of the graft itself. With the autologous full-thickness skin graft mouse model, the lifting of the native epidermis (i.e. the original epidermis that accompanied the FTSG as grafted onto the mice) was initially thought to be graft rejection. It was evident by the D15 dressing change, however, that the graft was forming new epidermis underneath the peeling epidermis. This was confirmed through both Haematoxylin and Eosin staining (see Figure 4.2d) and Masson's Trichrome staining (see Figure 5.4c). The murine wounds grafted with BTM also behaved in a similar fashion to that of humans, in that by D21, the synthetic graft had integrated with the dermis of native skin without *de* novo epidermis (see Figure 5.3c and 5.5c).

Grafted wounds inhibited the contraction seen in wounds left to repair spontaneously. Analysis demonstrated that the ungrafted wounds in the FTSG group, significant at the D15 dressing change and the D21 endpoint, were smaller than the grafted wounds (see Figure 4.1f). Within the BTM group, the ungrafted wounds were again smaller than those grafted. This difference was again significant at the D21 endpoint. Porcine wounds grafted with dermal matrix or epidermal autograft has also previously demonstrated the inhibition of wound contraction in a full-thickness wound model[226]. A study with rats demonstrated that an autologous FTSG also prevented wound contraction, however the degree of prevention had a relationship with the size of the initial FTSG[227]. Notably, in our study, wounds grafted with FTSG experienced less contraction than those grafted with BTM (compare Figure 4.1f with Figure 5.1f, and see Figure 5.2), which remains in line with the current clinical acceptance that the ability of a skin graft to inhibit wound contraction is directly proportional to the amount of collagen intact within the dermis[228]. Walden *et. al.* compared various grafts in a porcine model, concluding that a wound will experience the least amount of contraction if a dermis covers the wound, as well as an immediate epithelial coverage[226]. The culmination of skin bioengineering lies within this realm of a "one-step" graft, and understanding how an autologous FTSG and a synthetic graft may allow us to take a step towards this.

6.2.2. An autologous full-thickness skin grafts alters the wound repair trajectory of a full-thickness wound

A full-thickness wound bed in the SKH-1 model grafted with an autologous FTSG is different to a wound without a graft. The density of inflammatory cells (which are uncharacterised in this study, see Section 6.2.1) is less in grafted wounds than ungrafted wounds. Quantification of inflammatory cells can be by the marking of specimens with an inflammation grade by a blinded pathologist[226] or through immunohistochemical labelling.

As fibrin was not histologically evaluated at any part of the study, the presence or absence of fibrin that is part of the elastin-fibrin bond postulated by Burleson[8] as a crucial first step to the adherence and plasmatic imbibition phase of graft take was not evaluated. Specific anti-fibrin antibodies for immunostaining would be necessary to qualify and analyse the presence of fibrin in tissues to confirm in future. The acellular wound fluid that is stained pink in the haematoxylin and eosin sections in the full-thickness wound model (see Figure 3.2a, D1-D5 boxes) may well be fibrin, as it stains as pink and acellular in both rodents[229] and humans [230]. However, this needs to be confirmed.

Comparing FTSG with ungrafted wounds indicated a clear difference in the behaviour of key biomolecules at an RNA level in the wound bed. This will be discussed in further detail subsequently.

The effect of autografting on inflammation compared to an ungrafted full-thickness wound

At an RNA level, the expression fold change of IL-6 in grafted wounds was less than that in ungrafted wounds (see Figure 4.3a) at the inflammatory and proliferative timepoints of D1 and D5, although not statistically significant (D1: $p = 0.07$, D5: $p = 0.17$). RNA levels of IL-6 at the D21 wound bed did not differ between the grafted and ungrafted wounds. As with IL-6 mRNA, levels of the IL-8 (functional) homologues KC and LIX were higher at the ungrafted wound beds compared to the grafted wound beds at D1 and D5. At D21, KC/CXCL-1 was higher in the grafted wound bed than in the ungrafted bed, but this result was not significant ($p = 0.37$). At D21, levels of LIX/CXCL-5/6 were similar.

Together, this would suggest that the FTSG dampens the actions of key pro-inflammatory mediators, at least at an RNA level, compared to full-thickness wounds allowed to heal spontaneously. This would support our primary hypothesis that skin grafting modulates the

inflammatory response on its path to facilitate wound repair. How this is facilitated requires further investigation, with consideration that a FTSG carries with it its native fibroblasts, endothelial cells, keratinocytes and epidermal stem cell niches that are likely to facilitate the dampening of inflammation. By D21, both wound beds are densely populated with cells of the dermis and are epithelialized, hence the lack of difference between the grafted and ungrafted wound bed conditions for the inflammatory targets of interest.

It has previously been suggested that skin grafting via a dermal template by itself or dermal template with epidermal graft decreases the quantity of inflammatory cells present at the wound bed up to 14 days post-wounding in a porcine full-thickness wound model[226]. This would thus encourage the notion that the lack of inflammatory cells (such as neutrophils) at the wound bed leads to less need for their recruitment of macrophages and other mediators.

In contrast, one may speculate the presence of keratinocytes and fibroblasts in an FTSG may lead to higher levels of KC and LIX, as other inflammatory mediators (not studied in the skin graft models) such as IL-1β are able to stimulate keratinocytes and fibroblasts to secrete IL-8. However, it is likely that wound keratinocytes actively participating in wound repair (such as those involves in epithelial-mesenchymal transition[94]) would behave differently to pre-existing keratinocytes that may be undergoing terminal differentiation[22] and with different growth factor/cytokine secretion profile influencing other cells' behaviours and interactions differently.

Interestingly, protein evaluation of IL-6 did not demonstrate any difference at D5 between the grafted and ungrafted wound beds. The translational delay that occurs between mRNA presence and protein expression is not able to explain this, as there was a difference in the mRNA levels of IL-6 between the two wounds at D1.

Post-translational modification from mRNA to protein is possible, as although a promising candidate for observing wound repair, the genetic background of the hairless SKH-1 strain of mouse is relatively uncharacterised[191]. Another possibility to account for this conspicuous difference is that the protein may have degraded between absolute quantification and protein array experiments, despite appropriate aliquoting of samples to reduce multiple freeze/thaw cycles, and adding protease inhibitors to the final RIPA lysis buffer.

Issues with total protein yield (see Section 3.1.6) of lysates also influenced the amount of protein used for the protein array membranes. A previous study from the Skin Bioengineering Laboratory utilised a similar protein array membrane[231], however lysates were used at a 100µg quantity. Correspondence with the manufacturing company (AbCam) was sought prior to completing the experiments, which ensured that 50µg of protein was an acceptable quantity for the membrane experiments. Nevertheless, there are no published studies in the literature that utilise the Neuro Antibody Protein Array Membranes used in this current study with protein lysates isolated from skin and cutaneous wound beds, and as such, 50µg of protein may have been insufficient to yield a true result. In conjunction with this, the SKH-1 mouse wound bed may also contain proteases that degrade the protein, thus leaving wound bed samples with poor protein content. Furthermore, to the best of our knowledge, skin grafts have not been investigated in this train of mice, thus limiting the comparative ability of any result. Inflammation may be in grafted epidermis and not in the wound bed. No other study has dissected out the molecular changes in the wound bed from a grafted epidermis.

In addition to the wound bed itself, size and location of the wounds could have been major factors in the behaviour of target proteins investigated. Despite increasing the wound bed size to almost double halfway through the full-thickness wound model arm, the wound size still could have been too small to allow for any discernible difference between IL-6 in ungrafted or grafted wounds. Even with the increased wound size, two equally sized full-thickness wounds in this strain (with mice weighing greater than 21g) only equated to less than 5% of the total body surface area of the mouse according to the Meeh-Rubner formula[202, 203].

The two wounds given to the mice on the day of surgery were applied on the dorsum of the mice, approximately halfway down its body (See Section 2.1.3). To avoid excess mobilisation of the mouse whilst it was under anaesthesia, the wounds were made to be accessible by the operating researcher. Thus, the two wounds may have been too close in proximity to each other; and accounting for wound contraction, may have almost been abutting each other by the D21 endpoint. This may have affected the behaviour of growth factors and cytokines within the wounds, as the systemic action of the growth factors and cytokines of interest in this strain cannot be eliminated.

Interestingly, wound measurements at D0 were approximately 150mm^2 when calculated through real-time measurements. A 15mm diameter wound would, through basic mathematics, yield a SA of approximately 180mm^2. It is evident that, even with gentle manipulation of the mouse's skin intraoperatively, it is possible that the wound size alters through suturing and application of the silicon ring.

Finally, a simple explanation to account for the results seen in Figures 4.3 and 4.4 could be that the sample size for the experiments are too small for any difference to be detected, given the variability between each mouse. Power studies from previous work from the Skin Bioengineering Laboratory[183] determined that a minimum of 10 mice per endpoint in each of the graft groups would be required to detect 30% differences between the two groups; however, these numbers were not feasible given the pandemic-related constraints of the year.

The effect of autografting on proliferation/remodelling compared to an ungrafted full-thickness wound

The expression fold changes of VEGF-A, TGF-β1, Col3 and Col1 all increased between D1 and D5 (see Figure 4.3 d-g). Levels of all four proliferation markers were all significantly less in the grafted wound than in the ungrafted wound at D5. Notably, with the exception of VEGF-A, the expression of these markers remains relatively unchanged through D1, D5 and D21, which may indicate that an FTSG also alters the remodelling phase of wound healing, as a secondary effect of its modulation of inflammation.

VEGF-A levels between an ungrafted wound and a grafted wound at D1 were not significantly different, though levels of it are slightly higher in the ungrafted wounds at this point. Angiogenesis in both spontaneous wound repair and grafted wound repair is induced through hypoxia[232], and both wounds are considered to be relatively hypoxic at D1[54]. With grafts, the low levels of oxygen triggers an increase in hypoxia inducible factor (HIF)-1 transcription factor to induce upregulation of pro angiogenic growth factors such as VEGF[162, 233, 234]. The pro-angiogenic growth factors promote the formation of spherical capillary sprouts from the endothelial cells of the graft bed at 24 to 48 hours [235, 236]. The subsequent decrease at D5 might indicate that other pro-angiogenic factors (such as bFGF) are now governing vascularisation of the graft; it might also indicate that the remodelling phase is altered as a direct result of the modulation of inflammation. Macrophages are one of the main producers

of VEGF, with TGF-β1 also producing it via is actions on the fibroblasts and myofibroblasts[54] (which are not needed to the same magnitude that they are needed in wounds left to spontaneously repair).

As expected, levels of Col3 increasingly rises from D1 to D21 in an ungrafted bed, but remains low in a grafted bed (see Figure 4.3 f). Col1 levels are also low in a grafted wound bed (see Figure 4.3 g). The FTSG already expresses the proteins at these timepoints through the graft dermis, thus the wound is unlikely to require much more collagen.

It is curious that Col1 declines sharply at the unwounded bed between D5 and D21 in the grafted model; whereas, in the full-thickness wound model, expression fold change of Col1 was slightly higher at D21 compared to D5 (though not significant). Whether or not this is a reflection that grafts may also have effects on nearby wound beds, or the variability in murine subjects, requires further investigation.

MMP-2 is synthesised during proliferation where inflammation Is prominent[237], and both MMP-2 and MMP-3 have been identified as important in collagen degradation; MMP-3 also contributes to keratinocyte migration during epithalialisation[238]. At a protein level, there were no significant differences between levels of MMP-2 at the ungrafted and grafted wound bed. This was also seen with MMP-3. As the levels of Col1 declines between D5 and D21, this would imply that some sort of remodelling change was occurring in order to change the levels of the collagen. By D21, equal amounts of granulation tissue remodelling may be occurring at both wound beds according to the levels of MMP-2 and MMP-3. The reasons why we are not seeing any differences in the protein data are likely multifactorial, as previously stated.

6.2.3. A synthetic dermal graft alters the wound repair trajectory of a full-thickness wound

Similar to the wound bed grafted with an autologous FTSG, the wounds grafted with BTM had less inflammatory cells present compared to those without grafts at D1 (see Figure 5.1a). In fact, any type of cell was relatively sparse at the D1 wounds grafted with BTM. The grafted wound bed suddenly saw an increase of cells and collagen deposition at the graft bed by D5.

Although all mice allocated to the BTM group that were taken through to D21 survived to the endpoint, there was some mild concern regarding a white wound exudate that was present

at the grafted wound beds during dressing changes (images not shown). Mice in this group also received extra care and increased husbandry as a result of weight loss, which was not seen in the mice grafted with FTSG. Haematoxylin and eosin staining was not able to identify the presence of bacteria or other pathogen that may be responsible for this difference at D5 (see Figure 5.3).

The effect of a synthetic dermal graft compared to an ungrafted full-thickness wound

IL-6 was significantly different between the synthetically grafted and the ungrafted wound beds at an RNA level at the inflammatory and proliferative timepoints of D1 and D5 (Figure 5.7 a). Unlike the autografted group, there were significant differences the expression of some proteins between the grafted and ungrafted wound beds at both D5 and D21 timepoints. The RNA data is confirmed with protein data, as at D5, protein expression of IL-6 was significantly higher at the ungrafted wound bed compared to the grafted wound (Figure 5.9 b). IL-6 is also higher at an RNA level in an ungrafted wound at D1 post-op, where the dominating stage of wound repair is inflammation; however, there is currently no protein data to support this finding.

In addition, MIP-1α (macrophage inflammatory protein-1α) was higher in the grafted wound (Figure 5.8 a). MIP-1α is produced by macrophages and monocytes after they are stimulated by bacterial endotoxin[239] or if stimulated by pro-inflammatory mediators such as IL-1β, which itself can be produced at the wound bed in the setting of bacterial infections.

We were not able to identify any bacteria at the grafted wound bed on D5 to account for the endotoxins that may explain why MIP-1α expression significantly differs between the two (see Figure 5.3b). Further, IL-1β expression was similar between the two wound beds at D5 (Figure 5.9 c). Despite this, a mild infection may have in fact occurred at the wound beds grafted with BTM, accounting for the white wound exudate, weight loss, and elevated levels of MIP-1α not seen in the mice grafted with FTSG at the equivocal timepoint.

The protein expression of IL-6 was higher at the ungrafted wound at D5, but similar to the expression of IL-6 in the grafted wound on D21. Again, this is reflected in the quantitative RT-PCR data. Protein expression of KC was higher in the ungrafted wounds at D5, although not significantly. At D21, however, expression of KC was significantly higher at the autografted wound (Figure 5.8 b). Interestingly, this was not confirmed by the RNA data, as at D21, levels

of KC/CXCL-1 were similar between the ungrafted and the synthetically grafted wound bed (Figure 5.7 b).

At an RNA level, both Col3 and Col1 were higher in the ungrafted wound bed than that grafted with BTM at D5, however, only Col3 yielded a significant difference. The general trend of both targets is nevertheless similar, with an increase of the collagen between D1 and D5, followed by a decrease, regardless of the wound bed condition. This differs from the FTSG group, where the trend of Col3 was an incremental increase of Col3 at the ungrafted wound until it reached a nadir at D21 (Figure 4.3 f).

RNA levels of collagen, in general, were higher at the BTM grafted wound beds compared to the wound beds grafted with a FTSG (compare Figure 5.7 f with 4.3 f). It is possible that, as an acellular dermal template, cells are required to infiltrate into the wound bed, bringing with it a whole host of activity revolving around the recruitment of cells. As previously stated, a FTSG already carries with it many of the required cells and player in wound healing, and thus, may not require much more of an increase of the necessary proteins and their mRNA.

6.2.4. The stages of wound repair are altered at a biomolecular level between autografted and synthetically-grafted full-thickness wound beds

It is evident from the findings in this study that a skin graft does alter the wound repair environment in a murine full-thickness wound. Observation of the wound beds at the inflammatory, proliferation and remodelling timepoints suggest that the cellular infiltrates within the wound changes in a grafted wound bed; in that, cells of a likely inflammatory nature are less present in a grafted wound. Again, identification of what these cells are would be important in characterising the inflammatory process during this period, as well as allowing for the identification of possible origins of various cytokines and growth factors. Knowledge of the cellular components would likely be the next step in completing the overall picture required to understand the molecular mechanisms that allow for grafts to take.

Collagen deposition is also heavily altered between the graft types. Wounds with FTSGs consistently demonstrated higher amounts of collagen at D1, D5 and D21 timepoints compared to wounds grafted with BTM. Interestingly, the amount of collagen deposited increased between D1 and D5, and subsequently declining to at or below the D1 levels of collagen for both the FTSG and BTM groups at a protein level.

BTM is an acellular dermal template, and as such, essentially requires the synthesis of granulation tissue, but in a more organised fashion (hence the general term for dermal templates of 'dermal matrices' or 'scaffolds'). FTSGs innately carry with them from the day of the operation the fibroblasts and keratinocytes that are readily synthesised over a period of days during spontaneous wound healing. Thus, the increased amounts of collagen at all timepoints in the wounds grafted with FTSGs is justifiable. This 54% decrease in the amount of collagen at the wound bed between D5 and D21 for wounds with a FTSG was significant, whereas the 58% decrease in collagen seen in the wounds grafted with BTM between D5 and D21 was not significant. It is possible that the remodelling occurring at the wound beds grafted with an FTSG is more advanced compared to that occurring in BTM-grafted beds, and further work regarding the examination of levels of Collagen and MMPs at wound beds grafted with BTM is planned.

That notwithstanding, protein evaluation of the grafts at D5 and D21 using protein array membranes was performed. Results from the grafted wound were compared to their ungrafted counterpart on the same mouse, as well as between the types of grafts. When comparison was made between grafts, the differences are noteworthy and certainly points to the differential behaviour of the two types of grafts (see Figures 5.8 and 5.9).

These include a lower protein expression of IL-6 on D5 with wounds grafted with BTM compared to FTSG. Whereas, the expression of IL-6 was higher at the BTM-grafted wounds on D21 compared to FTSG-grafted wounds. Although neither of these were significant, there was significantly higher expression of IL-6 between D5 and D21 for wounds grafted with BTM (likely related to the increasing cellular production and activity of the fibroblasts and keratinocytes responsible for IL-6). There were also various significant differences between grafts with the IL-8 homologues, KC and LIX. Again, these pro-inflammatory cytokines demonstrated lower levels in BTM-grafted wounds at D5 but higher levels at D21 compared to FTSG-grafted wounds. The trend was the same for IL-1β.

These pro-inflammatory cytokines, particularly IL-1β, KC and LIX, help lead with the hypothesis that during the early stages of wound repair, the biomolecular mediators of inflammation are less present in wounds grafted with a synthetic, acellular dermal graft. The subsequent rise in these pro-inflammatory cytokines between D5 and D21 may indicate that inflammation persists along a much longer timeframe in synthetic dermal grafts. Given that

BTM does not have an epidermis, this is also feasible. The idea behind dermal matrices was that in large surface area cutaneous injuries of differing depths such as burns, the period in which the matrix would integrate into the native skin would allow for the repair of other, more superficial wounds so as to not overwhelm the systemic response to injury. As such, an inflammation period that is slightly longer than in wounds with a full-thickness skin graft may even be of benefit once the wound is sealed with an epidermis, as the granulation tissue still has all of the mediators of wound healing present at the wound bed, leaving the wound bed in a somewhat 'primed' manner.

Common markers investigated during proliferation and remodelling were also examined in our study. In general, levels of TGF-β1 and VEGF were less in wounds grafted with BTM at both D5 and D21; though these differences were not significant (see Figure 5.10a and c). Perhaps an increase in the mouse sample size may reveal a significant difference between the two. Interestingly, one would have thought that an acellular dermal template such as BTM would influence the wound bed in a manner that captured a significant difference between the two types of grafts. It is possible though that, at the end of the day, for these wounds to heal, both need to be vascularised. Furthermore, VEGF-A is not the only pro-angiogenic factor that could be investigated; perhaps investigation of another may lead to a discernible difference between the two graft groups.

However, the lack of difference between various key inflammatory and proliferative/remodelling targets, when using these membranes and when comparing grafted and ungrafted wounds, is somewhat complicated to explain. Again, various explanations for this are present and have previously been discussed. In future, it is possible to avoid the proximity of the two wounds conditions (grafted and ungrafted) by increasing the number of mice used in the study. This would thus lead to having a group of mice acting solely as the full-thickness wound controls, another group to receive solely FTSG, and a final group to receive solely BTM. This could also eliminate the need to create two smaller wounds, and instead create a larger wound that might exhibit the changes in inflammatory/growth factors of interest we are seeking.

6.3. Conclusions and Future Directions

The threefold aims of our study were fulfilled, to a degree. The final aim of identifying biomolecules related to successful graft take requires rigorous ongoing work, and likely requires other animal models such as impaired wound healing model in order to contrast the difference between unsuccessful and successful wound repair via grafts.

Nevertheless, establishing a novel mouse model with which to continue this work is integral. As far as we are aware, this is the first time the temporal profile of various target pro- and anti-inflammatory, as well as proliferation and remodelling markers has been investigated in this strain. In addition, skin grafts are widely used in surgery to accelerate wound repair in humans; but how they do so and how this differs from spontaneous wound repair was yet to be observed. To our understanding, this is the first body of work that attempts to do so.

We conclude that the novel SKH-1 mouse model of full-thickness wound repair is an effective animal model to use as a vehicle to investigate wound repair by epithelialisation. In characterising the wound repair trajectory of this model, it behaves in a similar fashion along as similar time-course to epithelialisation to wound repair in humans.

Further, we conclude that skin grafting with an autologous full-thickness skin graft can alter the wound micro-environment of spontaneous wound repair as seen at RNA level. Unfortunately, we were unable to confirm the same for the synthetic graft, BTM, due to time and pandemic-related constraints. In addition to this, it is also evident that an autologous full-thickness skin graft and a full-synthetic dermal graft behave differently at a biomolecular level.

Future directions could include the characterisation of the cells that populate a grafted wound bed, which would ultimately complete the picture by outlining which cells are responsible for activities that occur at the wound bed. Characterisation of fibroblasts may also be of use, as this may aid in the understanding of recapitulating the dermal adnexae that currently eludes cultured skin substitutes. Identifying the activity of cells in the DEJ and the likely communication between the epidermal and dermal layers to assist in graft heal may also be of interest, and may certainly aid in the understanding of what allows a graft to heal at a cellular level and how this is facilitated between cells. The investigation of terminal

differentiation in wounds left to repair spontaneously versus wounds that are grafted could also be a useful tool to highlight whether a particular stage of repair or healing is altered.

This study provides the first steps with which skin bioengineering can take in order to identify various key factors in successful wound repair by grafts. It is likely the beginning of a larger body of work. Knowledge of what constitutes a successful graft is imperative when it comes to devising more efficacious grafts or skin substitutes that are more likely to take, and to improve wound repair in a vulnerable population such as Burns patients.

References

1. Le Cocq H, Stanley PRW. Closing the gap: skin grafts and flaps. Surgery. 2011;29(10):502-6.

2. Ang GC. History of skin transplantation. Clinics in Dermatology. 2005;23(4):320-4.

3. Hauben DJ, Baruchin A, Mahler A. On the histroy of the free skin graft. Annals of plastic surgery. 1982;9(3):242-5.

4. Young F. Immediate Skin Grafting in the Treatment of Burns: A Preliminary Report. Annals of surgery. 1942;116(3):445-51.

5. Cope O, Langohr JL, Moore FD, Webster RC. Expeditious Care of Full-Thickness Burn Wounds by Surgical Excision and Grafting. Annals of surgery. 1947;125(1):1-22.

6. Lee KC, Joory K, Moiemen NS. History of burns: The past, present and the future. Burns Trauma. 2014;2(4):169-80.

7. Clemmesen T. Experimental studies on the healing of free skin autografts. Danish medical bulletin. 1967;14:Suppl 2:1-73.

8. Burleson R, Eiseman B. Nature of the bond between partial-thickness skin and wound granulations. Surgery. 1972;72(2):315-22.

9. Converse JM, Smahel J, Ballantyne DL, Jr., Harper AD. Inosculation of vessels of skin graft and host bed: a fortuitous encounter. British journal of plastic surgery. 1975;28(4):274-82.

10. Venus M, Waterman J, McNab I. Basic physiology of the skin. Surgery. 2011;29(10):471-4.

11. McLafferty E, Hendry C, Alistair F. The integumentary system: anatomy, physiology and function of skin. Nursing standard (Royal College of Nursing (Great Britain) : 1987). 2012;27(3):35-42.

12. Chu DH. Structure and Function of the Skin. In: Goldman LMD, Schafer AIMD, editors. Goldman-Cecil Medicine2016. p. 2632-7.e2.

13. Anderson BEMD. Anatomy, Physiology, and Embryology. In: Anderson BEMD, editor. Netter Collection of Medical Illustrations: Integumentary System, The2012. p. 1-11.

14. Rippa AL, Kalabusheva EP, Vorotelyak EA. Regeneration of Dermis: Scarring and Cells Involved. Cells. 2019;8(6).

15. Yousef H, Sharma S. Anatomy, Skin (Integument), Epidermis. StatPearls. Treasure Island (FL): StatPearls Publishing

StatPearls Publishing LLC.; 2019.

16. Smoller BR, Hiatt KM. Normal Cutaneous Histology. Dermatopathology: The Basics. Boston, MA: Springer US; 2009. p. 1-35.

17. Arda OP, Göksügür NMD, Tüzün YMD. Basic histological structure and functions of facial skin. Clinics in Dermatology. 2014;32(1):3-13.

18. Eckhart L, Lippens S, Tschachler E, Declercq W. Cell death by cornification. Biochimica et biophysica acta. 2013;1833(12):3471-80.

19. Potten CS, Saffhill R, Maibach HI. Measurement of the transit time for cells through the epidermis and stratum corneum of the mouse and guinea-pig. Cell and tissue kinetics. 1987;20(5):461-72.

20. Marques-Pereira JP, Leblond CP. MITOSIS AND DIFFERENTIATION IN THE STRATIFIED SQUAMOUS EPITHELIUM OF THE RAT ESOPHAGUS. The American journal of anatomy. 1965;117:73-87.

21. Clayton E, Doupe DP, Klein AM, Winton DJ, Simons BD, Jones PH. A single type of progenitor cell maintains normal epidermis. Nature. 2007;446(7132):185-9.

22. Potten CS. Cell replacement in epidermis (keratopoiesis) via discrete units of proliferation. International review of cytology. 1981;69:271-318.

23. Watt FM. Epidermal stem cells: markers, patterning and the control of stem cell fate. Philosophical transactions of the Royal Society of London Series B, Biological sciences. 1998;353(1370):831-7.

24. Mascre G, Dekoninck S, Drogat B, Youssef KK, Brohee S, Sotiropoulou PA, et al. Distinct contribution of stem and progenitor cells to epidermal maintenance. Nature. 2012;489(7415):257-62.

25. Watt FM. Involucrin and other markers of keratinocyte terminal differentiation. The Journal of investigative dermatology. 1983;81(1 Suppl):100s-3s.

26. Lai-Cheong JE, McGrath JA. Structure and function of skin, hair and nails. Medicine. 2009;37(5):223-6.

27. Burgeson RE, Christiano AM. The dermal-epidermal junction. Current opinion in cell biology. 1997;9(5):651-8.

28. Goletz S, Zillikens D, Schmidt E. Structural proteins of the dermal-epidermal junction targeted by autoantibodies in pemphigoid diseases. Experimental dermatology. 2017;26(12):1154-62.

29. Briggaman RA, Wheeler CE, Jr. The epidermal-dermal junction. The Journal of investigative dermatology. 1975;65(1):71-84.

30. Fine J-D, Eady RAJ, Bauer EA, Bauer JW, Bruckner-Tuderman L, Heagerty A, et al. The classification of inherited epidermolysis bullosa (EB): Report of the Third International Consensus Meeting on Diagnosis and Classification of EB. Journal of the American Academy of Dermatology. 2008;58(6):931-50.

31. Woodley DTMD. Distinct Fibroblasts in the Papillary and Reticular Dermis. Dermatologic clinics. 2017;35(1):95-100.

32. Thangapazham RL, Darling TN, Meyerle J. Alteration of Skin Properties with Autologous Dermal Fibroblasts. International Journal of Molecular Sciences. 2014;15(5):8407-27.

33. Sorrell JM, Caplan AI. Fibroblasts-a diverse population at the center of it all. International review of cell and molecular biology. 2009;276:161-214.

34. Driskell RR, Lichtenberger BM, Hoste E, Kretzschmar K, Simons BD, Charalambous M, et al. Distinct fibroblast lineages determine dermal architecture in skin development and repair. Nature. 2013;504(7479):277-81.

35. Philippeos C, Telerman SB, Oulès B, Pisco AO, Shaw TJ, Elgueta R, et al. Spatial and Single-Cell Transcriptional Profiling Identifies Functionally Distinct Human Dermal Fibroblast Subpopulations. Journal of Investigative Dermatology. 2018;138(4):811-25.

36. Korosec A, Frech S, Gesslbauer B, Vierhapper M, Radtke C, Petzelbauer P, et al. Lineage Identity and Location within the Dermis Determine the Function of Papillary and Reticular Fibroblasts in Human Skin. Journal of Investigative Dermatology. 2019;139(2):342-51.

37. Tabib T, Morse C, Wang T, Chen W, Lafyatis R. SFRP2/DPP4 and FMO1/LSP1 Define Major Fibroblast Populations in Human Skin. Journal of Investigative Dermatology. 2018;138(4):802-10.

38. Fuchs E, Tumbar T, Guasch G. Socializing with the Neighbors: Stem Cells and Their Niche. Cell. 2004;116(6):769-78.

39. Driskell RR, Clavel C, Rendl M, Watt FM. Hair follicle dermal papilla cells at a glance. J Cell Sci. 2011;124(Pt 8):1179-82.

40. Ansell DM, Kloepper JE, Thomason HA, Paus R, Hardman MJ. Exploring the "hair growth-wound healing connection": anagen phase promotes wound re-epithelialization. The Journal of investigative dermatology. 2011;131(2):518-28.

41. Oh JW, Kloepper J, Langan EA, Kim Y, Yeo J, Kim MJ, et al. A Guide to Studying Human Hair Follicle Cycling In Vivo. Journal of Investigative Dermatology. 2016;136(1):34-44.

42. Morasso MI, Tomic-Canic M. Epidermal stem cells: the cradle of epidermal determination, differentiation and wound healing. Biol Cell. 2005;97(3):173-83.

43. Nowak JA, Polak L, Pasolli HA, Fuchs E. Hair follicle stem cells are specified and function in early skin morphogenesis. Cell stem cell. 2008;3(1):33-43.

44. Ito M, Liu Y, Yang Z, Nguyen J, Liang F, Morris RJ, et al. Stem cells in the hair follicle bulge contribute to wound repair but not to homeostasis of the epidermis. Nature medicine. 2005;11(12):1351-4.

45. Hoogduijn MJ, Gorjup E, Genever PG. Comparative characterization of hair follicle dermal stem cells and bone marrow mesenchymal stem cells. Stem cells and development. 2006;15(1):49-60.

46. Meleshina AV, Rogovaya OS, Dudenkova VV, Sirotkina MA, Lukina MM, Bystrova AS, et al. Multimodal label-free imaging of living dermal equivalents including dermal papilla cells. Stem Cell Res Ther. 2018;9(1):84-.

47. Higgins CA, Roger MF, Hill RP, Ali-Khan AS, Garlick JA, Christiano AM, et al. Multifaceted role of hair follicle dermal cells in bioengineered skins. Br J Dermatol. 2017;176(5):1259-69.

48. Fuchs E, Nowak JA. Building epithelial tissues from skin stem cells. Cold Spring Harb Symp Quant Biol. 2008;73:333-50.

49. Hutley LJ, Newell FS, Kim Y-H, Luo X, Widberg CH, Shurety W, et al. A putative role for endogenous FGF-2 in FGF-1 mediated differentiation of human preadipocytes. Molecular and Cellular Endocrinology. 2011;339(1):165-71.

50. Rosen ED, Spiegelman BM. Adipocytes as regulators of energy balance and glucose homeostasis. Nature. 2006;444(7121):847-53.

51. Wang HJ, Pieper J, Schotel R, van Blitterswijk CA, Lamme EN. Stimulation of skin repair is dependent on fibroblast source and presence of extracellular matrix. Tissue engineering. 2004;10(7-8):1054-64.

52. Sultan SM, Barr JS, Butala P, Davidson EH, Weinstein AL, Knobel D, et al. Fat grafting accelerates revascularisation and decreases fibrosis following thermal injury. Journal of Plastic, Reconstructive & Aesthetic Surgery. 2012;65(2):219-27.

53. Schmidt BA, Horsley V. Intradermal adipocytes mediate fibroblast recruitment during skin wound healing. Development (Cambridge, England). 2013;140(7):1517-27.

54. Broughton G, 2nd, Janis JE, Attinger CE. The basic science of wound healing. Plast Reconstr Surg. 2006;117(7 Suppl):12s-34s.

55. Gurtner GC, Werner S, Barrandon Y, Longaker MT. Wound repair and regeneration. Nature. 2008;453:314.

56. Enoch S, Leaper DJ. Basic science of wound healing. Surgery (Oxford). 2008;26(2):31-7.

57. Reinke JM, Sorg H. Wound repair and regeneration. European surgical research Europaische chirurgische Forschung Recherches chirurgicales europeennes. 2012;49(1):35-43.

58. Singer AJ, Clark RAF. Cutaneous Wound Healing. New England Journal of Medicine. 1999;341(10):738-46.

59. WERNER S, GROSE R. Regulation of Wound Healing by Growth Factors and Cytokines. Physiological Reviews. 2003;83(3):835-70.

60. Kumar VMMDF, Abbas AKM, Aster JCMDP. Inflammation and Repair. In: Kumar VMMDF, Abbas AKM, Aster JCMDP, editors. Robbins and Cotran Pathologic Basis of Disease2015. p. 69-111.

61. Turner MD, Nedjai B, Hurst T, Pennington DJ. Cytokines and chemokines: At the crossroads of cell signalling and inflammatory disease. Biochimica et Biophysica Acta (BBA) - Molecular Cell Research. 2014;1843(11):2563-82.

62. Sehgal PB. Interleukin-6: Molecular Pathophysiology. Journal of Investigative Dermatology. 1990;94(6, Supplement):s2-s6.

63. Paquet P, Piérard GE. lnterleukin-6 and the Skin. International Archives of Allergy and Immunology. 1996;109(4):308-17.

64. Grossman RM, Krueger J, Yourish D, Granelli-Piperno A, Murphy DP, May LT, et al. Interleukin 6 is expressed in high levels in psoriatic skin and stimulates proliferation of cultured human keratinocytes. Proc Natl Acad Sci U S A. 1989;86(16):6367-71.

65. Sawamura D, Meng X, Ina S, Sato M, Tamai K, Hanada K, et al. Induction of keratinocyte proliferation and lymphocytic infiltration by in vivo introduction of the IL-6 gene into keratinocytes and possibility of keratinocyte gene therapy for inflammatory skin diseases using IL-6 mutant genes. Journal of immunology (Baltimore, Md : 1950). 1998;161(10):5633-9.

66. Turksen K, Kupper T, Degenstein L, Williams I, Fuchs E. Interleukin 6: insights to its function in skin by overexpression in transgenic mice. Proc Natl Acad Sci U S A. 1992;89(11):5068-72.

67. Nguon N, Clery-Barraud C, Vallet V, Elbakdouri N, Wartelle J, Mouret S, et al. Time course of lewisite-induced skin lesions and inflammatory response in the SKH-1 hairless mouse model. Wound repair and regeneration : official publication of the Wound Healing Society [and] the European Tissue Repair Society. 2014;22(2):272-80.

68. Ricketts KM, Santai CT, France JA, Graziosi AM, Doyel TD, Gazaway MY, et al. Inflammatory cytokine response in sulfur mustard-exposed mouse skin. Journal of applied toxicology : JAT. 2000;20 Suppl 1:S73-6.

69. Bryan D, Walker KB, Ferguson M, Thorpe R. Cytokine gene expression in a murine wound healing model. Cytokine. 2005;31(6):429-38.

70. Gallucci RM, Simeonova PP, Matheson JM, Kommineni C, Guriel JL, Sugawara T, et al. Impaired cutaneous wound healing in interleukin-6–deficient and immunosuppressed mice. The FASEB Journal. 2000;14(15):2525-31.

71. Gallucci RM, Sloan DK, Heck JM, Murray AR, O'Dell SJ. Interleukin 6 Indirectly Induces Keratinocyte Migration. Journal of Investigative Dermatology. 2004;122(3):764-72.

72. Gallucci RM, Sugawara T, Yucesoy B, Berryann K, Simeonova PP, Matheson JM, et al. Interleukin-6 Treatment Augments Cutaneous Wound Healing in Immunosuppressed Mice. Journal of Interferon & Cytokine Research. 2001;21(8):603-9.

73. Gallucci RM, Lee EG, Tomasek JJ. IL-6 Modulates Alpha-Smooth Muscle Actin Expression in Dermal Fibroblasts from IL-6-Deficient Mice. Journal of Investigative Dermatology. 2006;126(3):561-8.

74. Dinarello CA. Immunological and Inflammatory Functions of the Interleukin-1 Family. Annual Review of Immunology. 2009;27(1):519-50.

75. Smola H, Thiekotter G, Fusenig NE. Mutual induction of growth factor gene expression by epidermal-dermal cell interaction. J Cell Biol. 1993;122(2):417-29.

76. Werner S, Smola H. Paracrine regulation of keratinocyte proliferation and differentiation. Trends in Cell Biology. 2001;11(4):143-6.

77. Jimenez PA, Rampy MA. Keratinocyte Growth Factor-2 Accelerates Wound Healing in Incisional Wounds. Journal of Surgical Research. 1999;81(2):238-42.

78. Hu YP, Liang DP, Li XMD, Liu H-HMDP, Zhang XP, Zheng MP, et al. The Role of Interleukin-1 in Wound Biology. Part I: Murine In Silico and In Vitro Experimental Analysis. Anesthesia & Analgesia. 2010;111(6):1525-33.

79. Lateef Z, Stuart G, Jones N, Mercer A, Fleming S, Wise L. The Cutaneous Inflammatory Response to Thermal Burn Injury in a Murine Model. Int J Mol Sci. 2019;20(3).

80. Trengove NJ, Stacey MC, MacAuley S, Bennett N, Gibson J, Burslem F, et al. Analysis of the acute and chronic wound environments: the role of proteases and their inhibitors. Wound repair and regeneration : official publication of the Wound Healing Society [and] the European Tissue Repair Society. 1999;7(6):442-52.

81. Mirza RE, Fang MM, Ennis WJ, Koh TJ. Blocking interleukin-1β induces a healing-associated wound macrophage phenotype and improves healing in type 2 diabetes. Diabetes. 2013;62(7):2579-87.

82. Mirza RE, Fang MM, Novak ML, Urao N, Sui A, Ennis WJ, et al. Macrophage PPARγ and impaired wound healing in type 2 diabetes. The Journal of pathology. 2015;236(4):433-44.

83. Barrow RE, Dasu MRK. Oxidative and Heat Stress Gene Changes in Hypertrophic Scar Fibroblasts Stimulated with Interleukin-1β1. Journal of Surgical Research. 2005;126(1):59-65.

84. Sommer K, Sander AL, Albig M, Weber R, Henrich D, Frank J, et al. Delayed wound repair in sepsis is associated with reduced local pro-inflammatory cytokine expression. PloS one. 2013;8(9):e73992-e.

85. Saxne T, Palladino MA, Jr., Heinegard D, Talal N, Wollheim FA. Detection of tumor necrosis factor alpha but not tumor necrosis factor beta in rheumatoid arthritis synovial fluid and serum. Arthritis and rheumatism. 1988;31(8):1041-5.

86. Yimin, Kohanawa M. A Regulatory Effect of the Balance between TNF-α and IL-6 in the Granulomatous and Inflammatory Response to Rhodococcus aurantiacus Infection in Mice. The Journal of Immunology. 2006;177(1):642-50.

87. Valvis SM, Waithman J, Wood FM, Fear MW, Fear VS. The Immune Response to Skin Trauma Is Dependent on the Etiology of Injury in a Mouse Model of Burn and Excision. Journal of Investigative Dermatology. 2015;135(8):2119-28.

88. Schröder JM. The neutrophil-activating peptide 1/interleukin 8, a novel neutrophil chemotactic cytokine. Archivum immunologiae et therapiae experimentalis. 1992;40(1):23-31.

89. Hammond ME, Lapointe GR, Feucht PH, Hilt S, Gallegos CA, Gordon CA, et al. IL-8 induces neutrophil chemotaxis predominantly via type I IL-8 receptors. Journal of immunology (Baltimore, Md : 1950). 1995;155(3):1428-33.

90. Harada A, Sekido N, Akahoshi T, Wada T, Mukaida N, Matsushima K. Essential involvement of interleukin-8 (IL-8) in acute inflammation. J Leukoc Biol. 1994;56(5):559-64.

91. Koch AE, Polverini PJ, Kunkel SL, Harlow LA, DiPietro LA, Elner VM, et al. Interleukin-8 as a macrophage-derived mediator of angiogenesis. Science (New York, NY). 1992;258(5089):1798.

92. Fousek K, Horn LA, Palena C. Interleukin-8: A chemokine at the intersection of cancer plasticity, angiogenesis, and immune suppression. Pharmacology & therapeutics. 2020:107692.

93. Li A, Dubey S, Varney ML, Dave BJ, Singh RK. IL-8 Directly Enhanced Endothelial Cell Survival, Proliferation, and Matrix Metalloproteinases Production and Regulated Angiogenesis. The Journal of Immunology. 2003;170(6):3369.

94. Yang J, Weinberg RA. Epithelial-mesenchymal transition: at the crossroads of development and tumor metastasis. Developmental cell. 2008;14(6):818-29.

95. Young A, McNaught C-E. The physiology of wound healing. Surgery. 2011;29(10):475-9.

96. Opalenik SR, Davidson JM. Fibroblast differentiation of bone marrow-derived cells during wound repair. FASEB journal : official publication of the Federation of American Societies for Experimental Biology. 2005;19(11):1561-3.

97. Sporn MB. TGF-β: 20 years and counting. Microbes and Infection. 1999;1(15):1251-3.

98. Vander Ark A, Cao J, Li X. TGF-β receptors: In and beyond TGF-β signaling. Cellular Signalling. 2018;52:112-20.

99. Barrientos S, Stojadinovic O, Golinko MS, Brem H, Tomic-Canic M. Growth factors and cytokines in wound healing. Wound repair and regeneration : official publication of the Wound Healing Society [and] the European Tissue Repair Society. 2008;16(5):585-601.

100. Denton CP, Khan K, Hoyles RK, Shiwen X, Leoni P, Chen Y, et al. Inducible lineage-specific deletion of TbetaRII in fibroblasts defines a pivotal regulatory role during adult skin wound healing. The Journal of investigative dermatology. 2009;129(1):194-204.

101. Li Y, Fan J, Chen M, Li W, Woodley DT. Transforming growth factor-alpha: a major human serum factor that promotes human keratinocyte migration. The Journal of investigative dermatology. 2006;126(9):2096-105.

102. Decline F, Okamoto O, Mallein-Gerin F, Helbert B, Bernaud J, Rigal D, et al. Keratinocyte motility induced by TGF-beta1 is accompanied by dramatic changes in cellular interactions with laminin 5. Cell motility and the cytoskeleton. 2003;54(1):64-80.

103. Zhang J, Tian XJ, Zhang H, Teng Y, Li R, Bai F, et al. TGF-beta-induced epithelial-to-mesenchymal transition proceeds through stepwise activation of multiple feedback loops. Science signaling. 2014;7(345):ra91.

104. Sellheyer K, Bickenbach JR, Rothnagel JA, Bundman D, Longley MA, Krieg T, et al. Inhibition of skin development by overexpression of transforming growth factor beta 1 in the epidermis of transgenic mice. Proc Natl Acad Sci U S A. 1993;90(11):5237-41.

105. Kulkarni AB, Huh CG, Becker D, Geiser A, Lyght M, Flanders KC, et al. Transforming growth factor beta 1 null mutation in mice causes excessive inflammatory response and early death. Proc Natl Acad Sci U S A. 1993;90(2):770-4.

106. Brown RL, Ormsby I, Doetschman TC, Greenhalgh DG. Wound healing in the transforming growth factor-β1—deficient mouse. Wound Repair and Regeneration. 1995;3(1):25-36.

107. Koch RM, Roche NS, Parks WT, Ashcroft GS, Letterio JJ, Roberts AB. Incisional wound healing in transforming growth factor-beta1 null mice. Wound repair and regeneration : official publication of the Wound Healing Society [and] the European Tissue Repair Society. 2000;8(3):179-91.

108. Roberts AB, Sporn MB, Assoian RK, Smith JM, Roche NS, Wakefield LM, et al. Transforming growth factor type beta: rapid induction of fibrosis and angiogenesis in vivo and stimulation of collagen formation in vitro. Proceedings of the National Academy of Sciences. 1986;83(12):4167-71.

109. White LA, Mitchell TI, Brinckerhoff CE. Transforming growth factor beta inhibitory element in the rabbit matrix metalloproteinase-1 (collagenase-1) gene functions as a repressor of constitutive transcription. Biochimica et biophysica acta. 2000;1490(3):259-68.

110. Lee TY, Chin GS, Kim WJ, Chau D, Gittes GK, Longaker MT. Expression of transforming growth factor beta 1, 2, and 3 proteins in keloids. Annals of plastic surgery. 1999;43(2):179-84.

111. Tredget EB, Demare J, Chandran G, Tredget EE, Yang L, Ghahary A. Transforming growth factor-beta and its effect on reepithelialization of partial-thickness ear wounds in transgenic mice. Wound repair and regeneration : official publication of the Wound Healing Society [and] the European Tissue Repair Society. 2005;13(1):61-7.

112. Wang X-J, Han G, Owens P, Siddiqui Y, Li AG. Role of TGFβ-Mediated Inflammation in Cutaneous Wound Healing. Journal of Investigative Dermatology Symposium Proceedings. 2006;11(1):112-7.

113. Kaltalioglu K, Coskun-Cevher S. A bioactive molecule in a complex wound healing process: platelet-derived growth factor. International Journal of Dermatology. 2015;54(8):972-7.

114. Li W, Fan J, Chen M, Guan S, Sawcer D, Bokoch GM, et al. Mechanism of Human Dermal Fibroblast Migration Driven by Type I Collagen and Platelet-derived Growth Factor-BB. Molecular Biology of the Cell. 2004;15(1):294-309.

115. Brown DM, Chung SH, Pasia EN, Khouri RK. Treatment of avascular ulcers with cytokine-induced tissue generation and skin grafting. American journal of surgery. 1996;171(2):247-50.

116. Pharmaceuticals O. Food and Drug Administration: Regranex [Product Information Label]. 2007 [updated May 2008.

117. Cohen MA, Eaglstein WH. Recombinant human platelet-derived growth factor gel speeds healing of acute full-thickness punch biopsy wounds. Journal of the American Academy of Dermatology. 2001;45(6):857-62.

118. Gale NW, Yancopoulos GD. Growth factors acting via endothelial cell-specific receptor tyrosine kinases: VEGFs, angiopoietins, and ephrins in vascular development. Genes & development. 1999;13(9):1055-66.

119. Nissen NN, Polverini PJ, Koch AE, Volin MV, Gamelli RL, DiPietro LA. Vascular endothelial growth factor mediates angiogenic activity during the proliferative phase of wound healing. The American journal of pathology. 1998;152(6):1445-52.

120. Brown LF, Yeo KT, Berse B, Yeo TK, Senger DR, Dvorak HF, et al. Expression of vascular permeability factor (vascular endothelial growth factor) by epidermal keratinocytes during wound healing. The Journal of experimental medicine. 1992;176(5):1375-9.

121. Peng C, He Q, Luo C. Lack of Keratinocyte Growth Factor Retards Angiogenesis in Cutaneous Wounds. Journal of International Medical Research. 2011;39(2):416-23.

122. Greaves NS, Ashcroft KJ, Baguneid M, Bayat A. Current understanding of molecular and cellular mechanisms in fibroplasia and angiogenesis during acute wound healing. Journal of Dermatological Science. 2013;72(3):206-17.

123. Fiorentino DF, Zlotnik A, Vieira P, Mosmann TR, Howard M, Moore KW, et al. IL-10 acts on the antigen-presenting cell to inhibit cytokine production by Th1 cells. Journal of immunology (Baltimore, Md : 1950). 1991;146(10):3444-51.

124. Sato Y, Ohshima T, Kondo T. Regulatory Role of Endogenous Interleukin-10 in Cutaneous Inflammatory Response of Murine Wound Healing. Biochemical and Biophysical Research Communications. 1999;265(1):194-9.

125. Kubo H, Hayashi T, Ago K, Ago M, Kanekura T, Ogata M. Temporal expression of wound healing-related genes in skin burn injury. Legal Medicine. 2014;16(1):8-13.

126. Walmsley GG, Maan ZN, Wong VW, Duscher D, Hu MS, Zielins ER, et al. Scarless wound healing: chasing the holy grail. Plast Reconstr Surg. 2015;135(3):907-17.

127. Desmoulière A, Chaponnier C, Gabbiani G. Perspective Article: Tissue repair, contraction, and the myofibroblast. Wound Repair and Regeneration. 2005;13(1):7-12.

128. Ehrlich HP, Krummel TM. Regulation of wound healing from a connective tissue perspective. Wound Repair and Regeneration. 1996;4(2):203-10.

129. Bella J, Hulmes DJS. Fibrillar Collagens. In: Parry DAD, Squire JM, editors. Fibrous Proteins: Structures and Mechanisms. Cham: Springer International Publishing; 2017. p. 457-90.

130. Maione AG, Smith A, Kashpur O, Yanez V, Knight E, Mooney DJ, et al. Altered ECM deposition by diabetic foot ulcer-derived fibroblasts implicates fibronectin in chronic wound repair. Wound Repair and Regeneration. 2016;24(4):630-43.

131. Ulrich MM, Verkerk M, Reijnen L, Vlig M, van den Bogaerdt AJ, Middelkoop E. Expression profile of proteins involved in scar formation in the healing process of full-thickness excisional wounds in the porcine model. Wound repair and regeneration : official publication of the Wound Healing Society [and] the European Tissue Repair Society. 2007;15(4):482-90.

132. Rawlins JM, Lam WL, Karoo RO, Naylor IL, Sharpe DT. Quantifying Collagen Type in Mature Burn Scars: A Novel Approach Using Histology and Digital Image Analysis. Journal of Burn Care & Research. 2006;27(1):60-5.

133. Gao Y, Sun Y, Yang H, Qiu P, Cong Z, Zou Y, et al. A Low Molecular Weight Hyaluronic Acid Derivative Accelerates Excisional Wound Healing by Modulating Pro-Inflammation, Promoting Epithelialization and Neovascularization, and Remodeling Collagen. International Journal of Molecular Sciences. 2019;20(15):3722.

134. Kato T, Kure T, Chang JH, Gabison EE, Itoh T, Itohara S, et al. Diminished corneal angiogenesis in gelatinase A-deficient mice. FEBS letters. 2001;508(2):187-90.

135. Galis ZS, Johnson C, Godin D, Magid R, Shipley JM, Senior RM, et al. Targeted Disruption of the Matrix Metalloproteinase-9 Gene Impairs Smooth Muscle Cell Migration and Geometrical Arterial Remodeling. Circulation Research. 2002;91(9):852-9.

136. Vu TH, Shipley JM, Bergers G, Berger JE, Helms JA, Hanahan D, et al. MMP-9/gelatinase B is a key regulator of growth plate angiogenesis and apoptosis of hypertrophic chondrocytes. Cell. 1998;93(3):411-22.

137. Kyriakides TR, Wulsin D, Skokos EA, Fleckman P, Pirrone A, Shipley JM, et al. Mice that lack matrix metalloproteinase-9 display delayed wound healing associated with delayed reepithelization and disordered collagen fibrillogenesis. Matrix biology : journal of the International Society for Matrix Biology. 2009;28(2):65-73.

138. Hastbacka J, Freden F, Hult M, Bergquist M, Wilkman E, Vuola J, et al. Matrix metalloproteinases -8 and -9 and tissue inhibitor of metalloproteinase-1 in burn patients. A prospective observational study. PloS one. 2015;10(5):e0125918.

139. Langton AK, Halai P, Griffiths CEM, Sherratt MJ, Watson REB. The impact of intrinsic ageing on the protein composition of the dermal-epidermal junction. Mechanisms of Ageing and Development. 2016;156:14-6.

140. Moulin V, Auger FA, Garrel D, Germain L. Role of wound healing myofibroblasts on re-epithelialization of human skin. Burns : journal of the International Society for Burn Injuries. 2000;26(1):3-12.

141. Rognoni E, Pisco AO, Hiratsuka T, Sipila KH, Belmonte JM, Mobasseri SA, et al. Fibroblast state switching orchestrates dermal maturation and wound healing. Molecular systems biology. 2018;14(8):e8174.

142. Medina AMDF, Scott PGP, Ghahary AP, Tredget EEMDMF. Pathophysiology of Chronic Nonhealing Wounds. Journal of Burn Care & Rehabilitation July/August. 2005;26(4):306-19.

143. Qian L-W, Fourcaudot AB, Yamane K, You T, Chan RK, Leung KP. Exacerbated and prolonged inflammation impairs wound healing and increases scarring. Wound Repair and Regeneration. 2016;24(1):26-34.

144. Loots MAM, Lamme EN, Zeegelaar J, Mekkes JR, Bos JD, Middelkoop E. Differences in Cellular Infiltrate and Extracellular Matrix of Chronic Diabetic and Venous Ulcers Versus Acute Wounds. Journal of Investigative Dermatology. 1998;111(5):850-7.

145. Stephens P, Cook H, Hilton J, Jones CJ, Haughton MF, Wyllie FS, et al. An analysis of replicative senescence in dermal fibroblasts derived from chronic leg wounds predicts that telomerase therapy would fail to reverse their disease-specific cellular and proteolytic phenotype. Exp Cell Res. 2003;283(1):22-35.

146. Yager DR, Chen SM, Ward SI, Olutoye OO, Diegelmann RF, Kelman Cohen I. Ability of chronic wound fluids to degrade peptide growth factors is associated with increased levels of elastase activity and diminished levels of proteinase inhibitors. Wound repair and regeneration : official publication of the Wound Healing Society [and] the European Tissue Repair Society. 1997;5(1):23-32.

147. Rohani MG, Parks WC. Matrix remodeling by MMPs during wound repair. Matrix Biology. 2015;44-46:113-21.

148. Jeschke MG, Chinkes DL, Finnerty CC, Kulp G, Suman OE, Norbury WB, et al. Pathophysiologic response to severe burn injury. Annals of surgery. 2008;248(3):387-401.

149. Sheridan RL. A great constitutional disturbance. The New England journal of medicine. 2001;345(17):1271-2.

150. Ong YS, Samuel M, Song C. Meta-analysis of early excision of burns. Burns : journal of the International Society for Burn Injuries. 2006;32(2):145-50.

151. Herndon DN, Barrow RE, Rutan RL, Rutan TC, Desai MH, Abston S. A comparison of conservative versus early excision. Therapies in severely burned patients. Annals of surgery. 1989;209(5):547-52; discussion 52-3.

152. Puri V, Khare NA, Chandramouli MV, Shende N, Bharadwaj S. Comparative Analysis of Early Excision and Grafting vs Delayed Grafting in Burn Patients in a Developing Country. Journal of burn care & research : official publication of the American Burn Association. 2016;37(5):278-82.

153. Enoch S, Roshan A, Shah M. Emergency and early management of burns and scalds. BMJ. 2009;338:b1037.

154. Johnson RM, Richard R. Partial-thickness burns: identification and management. Advances in skin & wound care. 2003;16(4):178-87; quiz 88-9.

155. Greenhalgh DGMDF. Models of Wound Healing. Journal of Burn Care & Rehabilitation July/August. 2005;26(4):293-305.

156. Kim HS, Kim J-H, Yim H, Kim D. Changes in the levels of interleukins 6, 8, and 10, tumor necrosis factor alpha, and granulocyte-colony stimulating factor in Korean burn patients: relation to burn size and postburn time. Ann Lab Med. 2012;32(5):339-44.

157. Jeschke MG, Gauglitz GG, Finnerty CC, Kraft R, Mlcak RP, Herndon DN. Survivors versus nonsurvivors postburn: differences in inflammatory and hypermetabolic trajectories. Annals of surgery. 2014;259(4):814-23.

158. Finnerty CC, Jeschke MG, Herndon DN, Gamelli R, Gibran N, Klein M, et al. Temporal cytokine profiles in severely burned patients: a comparison of adults and children. Mol Med. 2008;14(9-10):553-60.

159. Hur J, Yang HT, Chun W, Kim J-H, Shin S-H, Kang HJ, et al. Inflammatory cytokines and their prognostic ability in cases of major burn injury. Ann Lab Med. 2015;35(1):105-10.

160. Afifi GY, Akelman E, Argenta LC, Arnaud E, Ashmead D, Aston SJ, et al. Contributors. In: Weinzweig J, editor. Plastic Surgery Secrets Plus (Second Edition). Philadelphia: Mosby; 2010. p. xiii-xxiv.

161. Pepper FJ. Studies on the viability of mammalian skin autografts after storage at different temperatures. British journal of plastic surgery. 1954;6(4):250-6.

162. Vural E, Berbee M, Acott A, Blagg R, Fan CY, Hauer-Jensen M. Skin graft take rates, granulation, and epithelialization: dependence on myeloid cell hypoxia-inducible factor 1alpha. Archives of otolaryngology--head & neck surgery. 2010;136(7):720-3.

163. Chiu TW. Stone's Plastic Surgery Facts and Figures. 3 ed. Cambridge: Cambridge University Press; 2011.

164. Kim EK, Hong JP. Efficacy of negative pressure therapy to enhance take of 1-stage allodermis and a split-thickness graft. Annals of plastic surgery. 2007;58(5):536-40.

165. Wang X, Zhang Y, Han C. Topical negative pressure improves autograft take by altering nutrient diffusion: A hypothesis. Medical science monitor : international medical journal of experimental and clinical research. 2014;20:61-3.

166. Landau AG, Hudson DA, Adams K, Geldenhuys S, Pienaar C. Full-thickness skin grafts: maximizing graft take using negative pressure dressings to prepare the graft bed. Annals of plastic surgery. 2008;60(6):661-6.

167. Schneider LA, Korber A, Grabbe S, Dissemond J. Influence of pH on wound-healing: a new perspective for wound-therapy? Archives of dermatological research. 2007;298(9):413-20.

168. Lang E, Schaefer BM, Eickhoff U, Hohl HP, Kramer MD, Maier-Reif K. Rapid normalization of epidermal integrin expression after allografting of human keratinocytes. The Journal of investigative dermatology. 1996;107(3):423-7.

169. Compton CC, Hickerson W, Nadire K, Press W. Acceleration of skin regeneration from cultured epithelial autografts by transplantation to homograft dermis. The Journal of burn care & rehabilitation. 1993;14(6):653-62.

170. Rudolph R. Inhibition of myofibroblasts by skin grafts. Plast Reconstr Surg. 1979;63(4):473-80.

171. Desmouliere A, Redard M, Darby I, Gabbiani G. Apoptosis mediates the decrease in cellularity during the transition between granulation tissue and scar. The American journal of pathology. 1995;146(1):56-66.

172. Garbin S, Pittet B, Montandon D, Gabbiani G, Desmoulière A. Covering by a flap induces apoptosis of granulation tissue myofibroblasts and vascular cells. Wound Repair and Regeneration. 1996;4(2):244-51.

173. Knapik A, Hegland N, Calcagni M, Althaus M, Vollmar B, Giovanoli P, et al. Metalloproteinases facilitate connection of wound bed vessels to pre-existing skin graft vasculature. Microvascular research. 2012;84(1):16-23.

174. Capla JM, Ceradini DJ, Tepper OM, Callaghan MJ, Bhatt KA, Galiano RD, et al. Skin graft vascularization involves precisely regulated regression and replacement of endothelial cells through both angiogenesis and vasculogenesis. Plast Reconstr Surg. 2006;117(3):836-44.

175. Jalili RB, Pourghadiri A, Li Y, Cleversey C, Kilani RT, Ghahary A. Split Thickness Grafts Grow From Bottom Up in Large Skin Injuries. Journal of burn care & research : official publication of the American Burn Association. 2019;40(6):727-33.

176. Rose LF, Wu JC, Carlsson AH, Tucker DI, Leung KP, Chan RK. Recipient wound bed characteristics affect scarring and skin graft contraction. Wound repair and regeneration : official publication of the Wound Healing Society [and] the European Tissue Repair Society. 2015;23(2):287-96.

177. Shahrokhi S, Arno A, Jeschke MG. The use of dermal substitutes in burn surgery: acute phase. Wound repair and regeneration : official publication of the Wound Healing Society [and] the European Tissue Repair Society. 2014;22(1):14-22.

178. Lee KH. Tissue-engineered human living skin substitutes: development and clinical application. Yonsei medical journal. 2000;41(6):774-9.

179. Pham C, Greenwood J, Cleland H, Woodruff P, Maddern G. Bioengineered skin substitutes for the management of burns: a systematic review. Burns : journal of the International Society for Burn Injuries. 2007;33(8):946-57.

180. Hodgkinson T, Bayat A. Dermal substitute-assisted healing: enhancing stem cell therapy with novel biomaterial design. Archives of dermatological research. 2011;303(5):301-15.

181. Casadiegos S, Bustos RH, Fontanilla MR. Comparative evaluation of healing biomarkers in skin wound exudates using a nanobiosensor and histological analysis of full-thickness skin wounds grafted with multidirectional or unidirectional artificial dermis. Journal of tissue engineering and regenerative medicine. 2018;12(12):2299-308.

182. Greenwood J, Amjadi M, Dearman B, Mackie I. Real-time demonstration of split skin graft inosculation and integra dermal matrix neovascularization using confocal laser scanning microscopy. Eplasty. 2009;9:e33.

183. Cheshire PA, Herson MR, Cleland H, Akbarzadeh S. Artificial dermal templates: A comparative study of NovoSorb Biodegradable Temporising Matrix (BTM) and Integra((R)) Dermal Regeneration Template (DRT). Burns : journal of the International Society for Burn Injuries. 2016;42(5):1088-96.

184. Fang RC, Mustoe TA. Animal models of wound healing: utility in transgenic mice. Journal of biomaterials science Polymer edition. 2008;19(8):989-1005.

185. Boyko TV, Longaker MT, Yang GP. Laboratory Models for the Study of Normal and Pathologic Wound Healing. Plast Reconstr Surg. 2017;139(3):654-62.

186. Wilhelm K-P, Wilhelm D, Bielfeldt S. Models of wound healing: an emphasis on clinical studies. Skin Research and Technology. 2017;23(1):3-12.

187. Zomer HD, Trentin AG. Skin wound healing in humans and mice: Challenges in translational research. Journal of Dermatological Science. 2018;90(1):3-12.

188. Abdullahi A, Amini-Nik S, Jeschke MG. Animal models in burn research. Cellular and molecular life sciences : CMLS. 2014;71(17):3241-55.

189. Galiano RD, Michaels V, Joseph, Dobryansky M, Levine JP, Gurtner GC. Quantitative and reproducible murine model of excisional wound healing. Wound Repair and Regeneration. 2004;12(4):485-92.

190. Dunn L, Prosser HC, Tan JT, Vanags LZ, Ng MK, Bursill CA. Murine model of wound healing. Journal of visualized experiments : JoVE. 2013(75):e50265.

191. Benavides F, Oberyszyn TM, VanBuskirk AM, Reeve VE, Kusewitt DF. The hairless mouse in skin research. J Dermatol Sci. 2009;53(1):10-8.

192. Wang L-L, Zhao R, Liu C-S, Liu M, Li S-S, Li J-Y, et al. A fundamental study on the dynamics of multiple biomarkers in mouse excisional wounds for wound age estimation. Journal of Forensic and Legal Medicine. 2016;39:138-46.

193. Wise LM, Stuart GS, Real NC, Fleming SB, Mercer AA. VEGF Receptor-2 Activation Mediated by VEGF-E Limits Scar Tissue Formation Following Cutaneous Injury. Advances in wound care. 2018;7(8):283-97.

194. Yee CS, Yao Y, Xu Q, McCarthy B, Sun-Lin D, Tone M, et al. Enhanced production of IL-10 by dendritic cells deficient in CIITA. Journal of immunology (Baltimore, Md : 1950). 2005;174(3):1222-9.

195. Jentho E, Bodden M, Schulz C, Jung AL, Seidel K, Schmeck B, et al. microRNA-125a-3p is regulated by MyD88 in Legionella pneumophila infection and targets NTAN1. PloS one. 2017;12(4):e0176204.

196. Chalmers JA, Martino TA, Tata N, Ralph MR, Sole MJ, Belsham DD. Vascular circadian rhythms in a mouse vascular smooth muscle cell line (Movas-1). American journal of physiology Regulatory, integrative and comparative physiology. 2008;295(5):R1529-38.

197. Marek I, Canu M, Cordasic N, Rauh M, Volkert G, Fahlbusch FB, et al. Sex differences in the development of vascular and renal lesions in mice with a simultaneous deficiency of Apoe and the integrin chain Itga8. Biology of sex differences. 2017;8:19.

198. Prokopec SD, Buchner NB, Fox NS, Chong LC, Mak DY, Watson JD, et al. Validating reference genes within a mouse model system of 2,3,7,8-tetrachlorodibenzo-p-dioxin (TCDD) toxicity. Chemico-biological interactions. 2013;205(1):63-71.

199. Brattelid T, Winer LH, Levy FO, Liestøl K, Sejersted OM, Andersson KB. Reference gene alternatives to Gapdh in rodent and human heart failure gene expression studies. BMC molecular biology. 2010;11:22.

200. Sánchez-Alvarez R, Gayen S, Vadigepalli R, Anni H. Ethanol diverts early neuronal differentiation trajectory of embryonic stem cells by disrupting the balance of lineage specifiers. PloS one. 2013;8(5):e63794.

201. Schmittgen TD, Livak KJ. Analyzing real-time PCR data by the comparative CT method. Nature Protocols. 2008;3(6):1101-8.

202. Gouma E, Simos Y, Verginadis I, Lykoudis E, Evangelou A, Karkabounas S. A simple procedure for estimation of total body surface area and determination of a new value of Meeh's constant in rats. Laboratory animals. 2012;46(1):40-5.

203. Cheung MC, Spalding PB, Gutierrez JC, Balkan W, Namias N, Koniaris LG, et al. Body Surface Area Prediction in Normal, Hypermuscular, and Obese Mice. Journal of Surgical Research. 2009;153(2):326-31.

204. Chen JS, Longaker MT, Gurtner GC. Murine models of human wound healing. Methods Mol Biol. 2013;1037:265-74.

205. Jimi S, De Francesco F, Ferraro GA, Riccio M, Hara S. A Novel Skin Splint for Accurately Mapping Dermal Remodeling and Epithelialization During Wound Healing. J Cell Physiol. 2017;232(6):1225-32.

206. Sun Y, Song L, Zhang Y, Wang H, Dong X. Adipose stem cells from type 2 diabetic mice exhibit therapeutic potential in wound healing. Stem Cell Res Ther. 2020;11(1):298.

207. Kopec AM, Rivera PD, Lacagnina MJ, Hanamsagar R, Bilbo SD. Optimized solubilization of TRIzol-precipitated protein permits Western blotting analysis to maximize data available from brain tissue. Journal of neuroscience methods. 2017;280:64-76.

208. Simoes AE, Pereira DM, Amaral JD, Nunes AF, Gomes SE, Rodrigues PM, et al. Efficient recovery of proteins from multiple source samples after TRIzol((R)) or TRIzol((R))LS RNA extraction and long-term storage. BMC genomics. 2013;14:181.

209. Vagenende V, Yap MG, Trout BL. Mechanisms of protein stabilization and prevention of protein aggregation by glycerol. Biochemistry. 2009;48(46):11084-96.

210. Rastgar Jazii F, Karkhane AA, Yakhchali B, Fatemi SS, Deezagi A. A simplified purification procedure for recombinant human granulocyte macrophage-colony stimulating factor from periplasmic space of Escherichia coli. Journal of chromatography B, Analytical technologies in the biomedical and life sciences. 2007;856(1-2):214-21.

211. Tsumoto K, Ejima D, Senczuk AM, Kita Y, Arakawa T. Effects of salts on protein-surface interactions: applications for column chromatography. Journal of pharmaceutical sciences. 2007;96(7):1677-90.

212. Support TT. Interpretation of Nucleic Acid 260/280 Ratios: Thermofisher Scientific; 2012 [Available from: http://tools.thermofisher.com/content/sfs/brochures/T123-NanoDrop-Lite-Interpretation-of-Nucleic-Acid-260-280-Ratios.pdf.

213. Qiagen. Quick-Start Protocol - QIAzol(R) Lysis Reagent 2011 [Available from: https://www.qiagen.com/au/resources/resourcedetail?id=6c452080-142a-44a7-a902-9177dea57d7c&lang=en.

214. Krebs S, Fischaleck M, Blum H. A simple and loss-free method to remove TRIzol contaminations from minute RNA samples. Analytical biochemistry. 2009;387(1):136-8.

215. Lee JTY, Cheung KMC, Leung VYL. Correction for concentration overestimation of nucleic acids with phenol. Analytical biochemistry. 2014;465:179-86.

216. Blatter A. Choosing the Right Method for Nucleic Acid Quantitation 2018 [Available from: https://www.promega.com.au/resources/pubhub/choosing-the-right-method-for-nucleic-acid-quantitation/#references-c9a7b496-4311-4517-8968-f79b4eb55b34.

217. Hurst SD, Muchamuel T, Gorman DM, Gilbert JM, Clifford T, Kwan S, et al. New IL-17 family members promote Th1 or Th2 responses in the lung: in vivo function of the novel cytokine IL-25. Journal of immunology (Baltimore, Md : 1950). 2002;169(1):443-53.

218. Rumalla VK, Borah GL. Cytokines, growth factors, and plastic surgery. Plast Reconstr Surg. 2001;108(3):719-33.

219. Engelhardt E, Toksoy A, Goebeler M, Debus S, Bröcker EB, Gillitzer R. Chemokines IL-8, GROalpha, MCP-1, IP-10, and Mig are sequentially and differentially expressed during phase-specific infiltration of leukocyte subsets in human wound healing. The American journal of pathology. 1998;153(6):1849-60.

220. Zlotnik A, Yoshie O. Chemokines: a new classification system and their role in immunity. Immunity. 2000;12(2):121-7.

221. Rennekampff HO, Hansbrough JF, Kiessig V, Doré C, Sticherling M, Schröder JM. Bioactive interleukin-8 is expressed in wounds and enhances wound healing. The Journal of surgical research. 2000;93(1):41-54.

222. Bradbury A. Principles of Wound Healing. In: Fitridge R, Thompson M, editors. Mechanisms of Vascular Disease: A Reference Book for Vascular Specialists. Adelaide (AU): University of Adelaide Press, © The Contributors 2011.; 2011.

223. Kumar VMMDF, Abbas AKM, Aster JCMDP. Inflammation and Repair. In: Kumar VMMDF, Abbas AKM, Aster JCMDP, editors. Robbins and Cotran Pathologic Basis of Disease2015. p. 104-5.

224. Wise LM, Stuart GS, Real NC, Fleming SB, Mercer AA. Orf virus IL-10 accelerates wound healing while limiting inflammation and scarring. Wound Repair and Regeneration. 2014;22(3):356-67.

225. Kondo T, Ishida Y. Molecular pathology of wound healing. Forensic science international. 2010;203(1):93-8.

226. Walden JL, Garcia H, Hawkins H, Crouchet JR, Traber L, Gore DC. Both dermal matrix and epidermis contribute to an inhibition of wound contraction. Annals of plastic surgery. 2000;45(2):162-6.

227. Tuncali D, Yavuz N, Cigsar B, Gokrem S, Aslan G. Effect of full-thickness skin graft initial dimension on secondary wound contraction: experimental study in rats. Dermatologic surgery : official publication for American Society for Dermatologic Surgery [et al]. 2005;31(5):542-5.

228. Brown D, Garner W, Young VL. Skin grafting: dermal components in inhibition of wound contraction. Southern medical journal. 1990;83(7):789-95.

229. Taranov OS, Yakubitskiy SN, Nepomnyashchikh TS, Nesterov AE, Shchelkunov SN. Adjuvant-Induced Arthritis in Guinea Pigs. Acta naturae. 2016;8(4):110-7.

230. Boeckh-Behrens T, Schubert M, Förschler A, Prothmann S, Kreiser K, Zimmer C, et al. The Impact of Histological Clot Composition in Embolic Stroke. Clinical neuroradiology. 2016;26(2):189-97.

231. Banakh I, Cheshire P, Rahman M, Carmichael I, Jagadeesan P, Cameron NR, et al. A Comparative Study of Engineered Dermal Templates for Skin Wound Repair in a Mouse Model. Int J Mol Sci. 2020;21(12).

232. Frueh FS, Sanchez-Macedo N, Calcagni M, Giovanoli P, Lindenblatt N. The Crucial Role of Vascularization and Lymphangiogenesis in Skin Reconstruction. Eur Surg Res. 2018;59(3-4):242-54.

233. Gruss CJ, Satyamoorthy K, Berking C, Lininger J, Nesbit M, Schaider H, et al. Stroma formation and angiogenesis by overexpression of growth factors, cytokines, and proteolytic enzymes in human skin grafted to SCID mice. J Invest Dermatol. 2003;120(4):683-92.

234. Krock BL, Skuli N, Simon MC. Hypoxia-induced angiogenesis: good and evil. Genes Cancer. 2011;2(12):1117-33.

235. O'Ceallaigh S, Herrick SE, Bennett WR, Bluff JE, Ferguson MW, McGrouther DA. Perivascular cells in a skin graft are rapidly repopulated by host cells. J Plast Reconstr Aesthet Surg. 2007;60(8):864-75.

236. Lindenblatt N, Platz U, Althaus M, Hegland N, Schmidt CA, Contaldo C, et al. Temporary angiogenic transformation of the skin graft vasculature after reperfusion. Plast Reconstr Surg. 2010;126(1):61-70.

237. Lazaro JL, Izzo V, Meaume S, Davies AH, Lobmann R, Uccioli L. Elevated levels of matrix metalloproteinases and chronic wound healing: an updated review of clinical evidence. Journal of wound care. 2016;25(5):277-87.

238. Ravanti L, Kähäri VM. Matrix metalloproteinases in wound repair (review). International journal of molecular medicine. 2000;6(4):391-407.

239. Sherry B, Tekamp-Olson P, Gallegos C, Bauer D, Davatelis G, Wolpe SD, et al. Resolution of the two components of macrophage inflammatory protein 1, and cloning and characterization of one of those components, macrophage inflammatory protein 1 beta. The Journal of experimental medicine. 1988;168(6):2251-9.

Appendices

Animal Monitoring Sheets

TheAlfred

Skin Culture Lab
Victorian Adult Burns Service

INTRA-OPERATIVE ANIMAL MONITORING SHEET

Project Details: Wound treatment: Establishing novel mouse models and studying alternative interventions

Emergency Contacts: 1. Shiva Akbarzadeh (0449 798 966, 03 9903 0284) 2. Nikki Garcia (0432295886) 3. Mostafiz Rahman (0410 638 903, 03 9903 0616)

Mouse ID *Strain: SKH-1 Hairless Mice*
Lab ID: PAC ID:
Sex: Cage Mate:

Experimental Procedures
Date of Surgery:
Weight prior to surgery/g: Estimated DOB:

PRE-OPERATIVE CHECKLIST:

Anaesthetic machine checked:	YES / NO	
Scavenger cannister has been weighed:	YES / NO	Weight: _____
Recovery area is prepared:	YES / NO	
Mouse ID verified:	YES / NO	
Mouse was individually housed:	YES / NO	
Mouse consumed paracetamol jelly:	YES / NO	**OR**
Pre-operative SC/IP injections prepared:	YES / NO	
Mouse has been weighed pre-op:	YES / NO	
Final health check has been performed:	YES / NO	

SURGERY RECORD:
(Record the times)

Mouse placed in induction chamber:
Mouse placed on anaesthetic nose cone:
First incision:
Bandaged and removed from nose cone:
Placed in recovery cage:
Moved to recovery home cage:
Weight after surgery (g)- with bandage:

DO NOT PROCEED WITH SURGERY IF PRE-OPERATIVE CONDITIONS HAVE NOT BEEN MET

Observation		Time 1:	Time 2:	Time 3:	Time 4:	Time 5:	Time 6:
Isoflurane level							
Reflex (pedal and/or tail)	1. *No response* 2. *Withdrawal* 3. *Withdrawal/change in respiration*						
Respiration	1. *Slow* 2. *Rhythmic and stable* 3. *Fast*						
Skin colour	1. *Pink* 2. *Pale* 3. *Blue*						

CONTINUE WITH POST-SURGERY MONITORING SHEET AND EXPERIMENTAL ANIMAL LOG

TheAlfred

Skin Culture Lab
Victorian Adult Burns Service

POST-SURGERY ANIMAL MONITORING SHEET

Project Details: Wound treatment: Establishing novel mouse models and studying alternative interventions **AEC Number:** E/1920/2019/A
Emergency Contacts: 1. Shiva Akbarzadeh (0449 798966, 03 9903 0616) 2. Nicole Garcia (0432 295 886) 3. Mostafiz Rahman (0410638903)

Mouse ID *Strain: SKH-1 hairless mouse*		**Experimental Procedures**	
Lab ID:	PAC ID:	Date of Surgery:	
Sex:	Cage Mate:	Weight prior to surgery/g:	Estimated DOB:

ANIMALS TO BE MONITORED THREE TIMES IN THE FIRST 24 HOURS POST-SURGERY, THEN 2 TIMES DAILY FROM 24 TO 72 HOURS, THEN ONCE DAILY THEREAFTER. RECORD WEIGHT TWICE WEEKLY (*For weight loss: Administer standard supportive care, place on care form and increase frequency of weighing to once a day, if weight loss is 20% or more of their pre-surgery weight should be euthanized. Note: a 1-2g daily fluctuation in weight is normal).
Record score 0-3. RECORD ANY ACTION TAKEN IN COMMENTS.

Clinical Examination	**Date AND time AND initial**						
	FIRST 24 HOURS POST-SURGERY			**DAY 2 POST-SURGERY**		**DAY 3 POST-SURGERY**	
	TIME POINT 1	**TIME POINT 2**	**TIME POINT 3**	**TIME POINT 1**	**TIME POINT 2**	**TIME POINT 1**	**TIME POINT 2**
Abnormal respiration							
Hypothermia							
Sunken appearance/dull eyes							
Reduced appetite							
Lack of nesting							
Unusually docile or aggressive							
Inactive							
Increased muscle tone/ hunched appearance							
Orbital tightening							
Ear position							
Wound infection							
Bandaging							
*Weight (twice weekly)							
Other abnormal signs							
Comments (record weight loss, bandage treatment and bandage removal here if applicable)							

Lab ID:	Date AND time AND initial						
Clinical Examination	DAY 4	DAY 5	DAY 6	DAY 7	DAY 8	DAY 9	DAY 10
Abnormal respiration							
Hypothermia							
Sunken appearance/dull eyes							
Reduced appetite							
Lack of nesting							
Unusually docile or aggressive							
Inactive							
Increased muscle tone/ hunched appearance							
Orbital tightening							
Ear position							
Wound infection							
Bandaging							
* Weight (twice weekly)							
Other abnormal signs							
Comments (record weight loss, bandage treatment and bandage removal here if applicable)							

*For weight loss: Administer standard supportive care, place on care form and increase frequency of weighing to once a day, if weight loss is 20% or more of their pre-surgery weight should be euthanized. Note: a 1-2g daily fluctuation in weight is normal.

Lab ID:	**Date AND time AND initial**						
Clinical Examination	**DAY**	**DAY**	**DAY**	**DAY**	**DAY**	**DAY**	**DAY**
Abnormal respiration							
Hypothermia							
Sunken appearance/dull eyes							
Reduced appetite							
Lack of nesting							
Unusually docile or aggressive							
Inactive							
Increased muscle tone/ hunched appearance							
Orbital tightening							
Ear position							
Wound infection							
Bandaging							
*Weight (twice weekly)							
Other abnormal signs							
Comments (record weight loss, bandage treatment and bandage removal here if applicable)							

*For weight loss: Administer standard supportive care, place on care form and increase frequency of weighing to once a day, if weight loss is 20% or more of their pre-surgery weight should be euthanized. Note: a 1-2g daily fluctuation in weight is normal.